Dissertation zur Erlangung des Doktorgrades an der Fakultät
für Mathematik, Informatik und Naturwissenschaften
Fachbereich Geowissenschaften
Universität Hamburg

Natural variability of turbulence and stratification in a tidal shelf sea and the possible impact of offshore wind farms

vorgelegt von Larissa Kerstin Paul Schultze

Hamburg, 2018

– Korrigierte Fassung –
Tag der Disputation: 29.06.2018
Folgende Gutachter empfehlen die Annahme der Dissertation:
Dr. Jeffrey R. Carpenter
Prof. Dr. Carsten Eden

Versicherung an Eides statt

Hiermit versichere ich an Eides statt, dass ich die vorliegende Dissertation mit dem Titel: „Natural variability of turbulence and stratification in a tidal shelf sea and the possible impact of offshore wind farms“ selbstständig verfasst und keine anderen als die angegebenen Hilfsmittel – insbesondere keine im Quellenverzeichnis nicht benannten Internet-Quellen – benutzt habe. Alle Stellen, die wörtlich oder sinngemäß aus Veröffentlichungen entnommen wurden, sind als solche kenntlich gemacht. Ich versichere weiterhin, dass ich die Dissertation oder Teile davon vorher weder im In- noch im Ausland in einem anderen Prüfungsverfahren eingereicht habe und die eingereichte schriftliche Fassung der auf dem elektronischen Speichermedium entspricht.

Hamburg, den 15. Oktober 2018,

Zusammenfassung

Die Schelfmeere sind energiereiche Gebiete, die stark von den Gezeiten beeinflusst werden und erhöhte biologische Aktivität aufweisen. Wichtige Turbulenzquellen in den Schelfmeeren treten in fluiddynamischen Grenzschichten auf, beispielsweise durch Windspannung oder Wellenbrechung an der Wasseroberfläche, oder durch die Gezeitenbewegung am Meeresboden. Wenn sich eine Dichteschichtung in der Wassersäule bildet, tritt oft eine Thermokline auf, welche beide genannten Grenzregionen voneinander trennt und den vertikalen Transport von Wärme und anderen skalaren Größen kontrolliert. Während diapyknische Vermischungsprozesse weitreichende Auswirkungen auf das Meeresökosystem haben, bleibt die Untersuchung der Schlüsselprozesse, die die Dissipation turbulenter kinetischer Energie auslösen, ein aktives Forschungsgebiet.

Die Durchführung von Turbulenzmessungen auf See ist eine anspruchsvolle Aufgabe, die bis vor kurzer Zeit auf Kurzzeitmessungen in besonders turbulenten Gebieten beschränkt wurde. Der Mangel an Langzeitexperimenten könnte dabei das aktuelle Verständnis der Stärke turbulenzgetriebenen vertikalen Transports beeinflusst haben. Aufgrund der großräumigen Auswirkungen kleinskaliger Turbulenz muss diese in globalen Ozeanmodellen parametrisiert werden. Dies unterstreicht den Bedarf für ein umfangreicheres Bild der natürlichen Variabilität von Turbulenz, dessen Repräsentation in großskaligen Modellen optimiert werden muss.

Eines der Ziele der vorliegenden Arbeit ist es, Turbulenz in einem energetischen Gezeitenschelfmeer unter verschiedenen Wasserschichtungs- und Wetterbedingungen zu untersuchen, um einen Einblick in die lokale natürliche Variabilität zu erhalten. Dieses Ziel wird durch den Einsatz von autonomen Unterwassergleitern erreicht, welche in der Lage sind, Messungen ununterbrochen über mehrere Wochen zu sammeln, und Daten bei widrigen Wetterverhältnissen aufzuzeichnen. Die vertikale Struktur der Wassersäule während der Sommermonate im Untersuchungsgebiet ist variabel, und kann von einem durchgemischten Regime bis zu einer stabil geschichteten Thermokline reichen. Während die vertikale Struktur der Dissipationsrate in gut gemischten Regimen nahezu homogen ist, sorgt die Thermokline für eine fast laminare Wasserschicht, in der aktive Turbulenz nur sporadisch stattfindet. Obwohl die Thermokline aktive Turbulenz unterbricht, spielen solche turbulenten Ereignisse eine wichtige Rolle beim vertikalen Wärmetransport. Im Rahmen dieses Projekts wurden außerdem Turbulenz-Messungen während eines Sturmereignisses durchgeführt, aus denen die Dissipationsrate turbulenter kinetischer Energie errechnet wurde. Der Sturm bestand aus 2 großen Windstößen (Beaufort 6), die eine starke Scherung in der Thermokline verursachten. Die Dissipationsrate wurde dadurch um fast eine Größenordnung erhöht, und die Dichteschichtung wurde rasch umgekippt. Grobe Schätzungen legen nahe, dass solche seltenen Ereignisse erhöhter Turbulenzintensität eine wichtige Rolle bei den durchschnittlichen saisonalen vertikalen Energieflüssen spielen könnten.

Zusätzlich zu den natürlich vorkommenden Durchmischungsmechanismen stellen küstennahe Windturbinenfundamente eine Turbulenzquelle dar. Fortschritte in der Offshore-Windpark-Technologie haben den Aufbau von Windturbinenfundamenten in tieferen Meeresbereichen ermöglicht, in denen sich oftmals eine Dichteschichtung bildet. Daher ist das abschließende Ziel dieser Arbeit, die Rolle einzelner Fundamentstrukturen bei der Durchmischung lokaler Temperaturgradienten mit Hilfe von Feldbeobachtungen und Large Eddy-Simulations zu untersuchen. Der Nachlauf einzelner Monopiles weist eine starke Turbulenz auf, die auf einen engen Bereich von 50 – 100 m Breite bis zu

200 – 300 m stromabwärts begrenzt ist. Die durch einen Monopile erzeugten Temperaturanomalien und die Anomalien anderer skalarer Größen können bis zum Ende der Domäne beobachtet werden (ca. 600 m stromabwärts des Hindernisses). Obwohl der Einfluss einer einzigen Struktur auf die Durchmischung der Wassersäule gering ist, könnte das Zusammenspiel der Nachläufe mehrerer Strukturen bei schwacher Schichtung wichtig sein. Die Schelfmeere sind letztendlich dynamische Gebiete. Es ist daher von großer Relevanz, das Verständnis über deren natürliche Variabilität zu verbessern, um die Berechenbarkeit von Ereignissen starker Durchmischung sowie Veränderungen in diesen gesellschaftlich bedeutsamen Regionen zu erhöhen.

Abstract

Tidal shelf seas are energetic areas of intense biological activity and turbulent motion. This turbulence is largely generated at the water surface from wind stress and wave breaking and in the bottom boundary layer through friction generated by tidal motion. When stratification is formed, a thermocline often emerges and separates both boundary regions, controlling the vertical transport of heat and other scalars. Whilst diapycnal mixing has broad implications on the marine ecosystem functioning, unraveling the key processes triggering this mixing remains an active area of research.

Conducting turbulence measurements in the field is a challenging task, which until recently was constrained by short term measurements collected in areas of increased mixing, potentially introducing a bias in the current notion of vertical transport. Moreover, because of the large-scale impact of small-scale turbulent mixing, the latter has to be inevitably parameterized in ocean models. It is therefore essential to improve understanding of the natural variability of turbulent motion to improve its representation in large-scale models.

The present work aims to assess turbulence levels in an energetic tidal shelf sea under different stratification and weather conditions in order to gain an insight of the local natural variability of mixing. This aim was enabled through the use of autonomous underwater gliders, which are able to collect measurements uninterrupted for several weeks and to record data during adverse meteorological events. The vertical structure of the water column during the summer months in the study area, the German Bight of the North Sea, is variable and may range from a fully mixed regime to a stably stratified thermocline. Whilst the vertical structure of turbulence dissipation in well-mixed regimes is found to be close to homogeneous, the presence of a thermocline generates a low turbulence layer where active turbulent mixing takes place only sporadically. Despite their intermittency, such mixing events are shown to play an important role in heat transport. Within the framework of this study, turbulence measurements during a storm event were collected, from which the rate of dissipation of turbulent kinetic energy was obtained. The storm consisted of 2 major pulses of elevated wind speeds ($>$ Beaufort 6), which generated strong shear across the sharp thermocline and increased dissipation levels by nearly an order of magnitude, rapidly overturning the water column. Rough estimates suggest that such events of strong mixing could play an important role on the average seasonal fluxes.

In addition to naturally occurring mixing mechanisms, advances in offshore wind farm technology have enabled their construction and operation in deeper areas of shelf seas, in which stratification forms. Wind turbine foundations extract power from strong tidal currents and generate turbulence additional to background levels. Field measurements and large-eddy simulations were used to assess the role of single foundation structures in mixing local temperature gradients. The wake of single turbine foundations is characterized by strong turbulence localized within a narrow region of 50 – 100 m up to 200 – 300 m downstream, after which turbulence levels off towards background levels. The signature of temperature anomalies and that of other scalars due to the pylon reaches farther out and is observed until the end of the domain at 600 m downstream the obstacle. The additional mixing generated by a single foundation at current pylon spacings is low, however simplified estimates suggest that the effect of multiple structures on local stratification could be important. Lastly, shelf seas are dynamic regions and it is essential to advance understanding of their natural state and variability to improve the predictability of

mixing events, as well as changes that may affect these areas of great societal relevance.

Contents

1 Introduction

1.1 Stratification and turbulence in shelf seas

The shelf seas lie in the continental shelf, a submerged region between the shore and the shelf break, which is typically found at a depth of around 200 m. In these regions, the turbulence generated by frictional stresses from tidal and wind forcing together with buoyancy effects are commonly among the most relevant elements of the kinetic energy budget (*Simpson and Sharples*, 2012). These components compete to shape the vertical structure of the water column, and the balance between buoyancy and the mechanical inputs in shallow regions determine whether the water column will remain thoroughly mixed, or stratification will form (*Thorpe*, 2007; *van Leeuwen et al.*, 2015). Vertical stratification is generated when buoyancy effects acting to stabilize the water column are able to overcome mixing inputs to form density gradients, which in turn control vertical turbulent fluxes. In shelf seas situated in temperate regions of the globe, seasonal stratification often develops during the summer months, forming a pycnocline that separates the well-mixed surface and bottom layers (*van Leeuwen et al.*, 2015). The pycnocline can be depicted as a transition layer that separates the light and oxygenated surface mixed layer from the nutrient rich bottom. In this layer, gradients that control primary productivity coincide, and favor the build up of a biologically rich environment (*Ross and Sharples*, 2007). The formation of such a mid-water biological hot spot is thought to be a significant source of new production in the water column, similar in importance to the primary production generated in surface algal blooms (*Sharples et al.*, 2001). Moreover, although shelf seas account for only 7% of the total area of the ocean, they host 90% of the fishing activities, and are a source of up to 15% of the marine primary production worldwide (*Muller-Karger et al.*, 2005; *Simpson and Sharples*, 2012).

Shelf seas are known to be energetic maritime regions that contribute to the dissipation of a significant fraction of the total energy delivered to the ocean (*Palmer et al.*, 2008; *Simpson and Sharples*, 2012). Since 1950, a number of horizontal and vertical profiling instruments have been developed to study turbulence in the ocean and advance the understanding of mixing and fluid motion through turbulent friction (*Lueck et al.*, 2002; *Palmer et al.*, 2015). Among them, turbulence measurements by shear microstructure probes mounted in free-falling profilers loosely tethered to a research vessel have led to significant advancements in the field. Recent studies have brought attention to the fact that boundary layer turbulence is not sufficient to explain the mixing rates found in stratified shelf seas and have suggested that lower energy mechanisms, such as internal wave breaking and near-inertial current shear, might provide the power needed for diapycnal mixing through shear instabilities (e.g. *Simpson et al.*, 1996; *Rippeth et al.*, 2005; *Palmer et al.*, 2008; *Burchard and Rippeth*, 2009).

While it is crucial to improve understanding of other possible sources of turbulent dissipation, and therefore their representation in numerical models, sea-going research requires significant financial investments and labor force, which places a challenge of conducting experiments of longer duration. Furthermore, the generality of turbulence measurements has been until recently constrained by a majority of experiments with limited sampling duration (a few tidal cycles), selected areas with elevated mixing, and taken under fair weather conditions for safety reasons (*Simpson et al.*, 1996; *Palmer et al.*, 2008; *Rumyantseva et al.*, 2015; *Rovelli et al.*, 2016). Considering that mixing events are sporadic, there is a need to explore turbulence levels through long-term experiments, different stratification regimes and under extreme weather conditions to adequately understand the natural variability of mixing in shelf seas. To approach this challenge, autonomous vehicles for microstructure measurements have been continuously developed starting from the 1990s, which provide a cost-effective and reliable means of studying turbulence in the field (*Lueck et al.*, 2002; *Palmer et al.*, 2015; *Rudnick*, 2016). To improve the understanding of the natural variability of turbulence and mixing in the North Sea, we focus on data collected by underwater gliders, an example of an autonomous vehicle that has been recently used in the field during physical and biogeochemical experiments (*Peterson and Fer*, 2014; *Fer et al.*, 2014; *Palmer et al.*, 2015).

1.2 Anthropogenic activities in tidal shelf seas

In addition to natural mechanisms responsible for turbulence, mixing and biological productivity, anthropogenic activities in shelf seas might potentially induce a significant shift in the ecosystem balance. Approximately 40% of the global population inhabits areas within 100 km from the coast and shelf seas have been commonly exploited for their hydrocarbon rich sediments and biologically active environment. Like most shelf seas, the North Sea is an area of great social and economic relevance. Bordered by more than five European countries, the North Sea is one of the marine ecosystems with the highest human impact in the world, with some of its common uses being shipping, sediment extraction, natural gas and hydrocarbon transport through pipelines (*Halpern et al.*, 2008; *BSH*, 2016). Further, with the development of the offshore wind farm (OWF) technology in the past years, the North Sea has become increasingly utilized for the renewable energy sector (*Wind Europe et al.*, 2018).

Given the necessity to switch from non-renewable energy resources, such as fossil fuels, to more sustainable technologies, several countries have created legal frameworks and incentives for the exploitation of renewable energy sources. In Europe, the Renewable Energy Directive 2009/28/EC framework has been issued by the European Union (EU) in 2009 establishing binding goals for the increase in share of renewables for each of the member countries until 2020 (*European Parliament and the Council of the European Union*, 2009). The directive has determined that until 2020 at least 20% of the total energy consumption within the EU should consist of renewable energy sources (*European Parliament and the Council of the European Union*, 2009). Until the end of 2017, over 15 GW of offshore wind capacity had been installed and connected to the grid. If ongoing projects that are only partially grid connected are taken into consideration, this corresponds to a total of 92 OWFs spread through European maritime territory, equivalent to over 4,500 turbine foundations (*Wind Europe et al.*, 2018). The most relevant sea basins for offshore wind farming within the European Union (EU) to date are the Baltic Sea, the Atlantic Ocean, the Irish Sea and the North Sea, the latter supporting 71% of all offshore wind capacity in the region (*Wind Europe et al.*, 2018).

Germany is one of the most important investors in the construction and operation of OWFs within the EU, with a share of 34%. This corresponds to over 5 GW of installed capacity, and 23 OWFs connected to the grid (*Wind Europe et al.*, 2018), most of which is situated within the German Bight of the North Sea. As the number of OWFs is growing, their size, distance from shore, and average depths is increasing as well. In 2017 (2011), the average size of an OWF was 493 MW (200 MW) with a distance from the coast of 41 km (23 km) and an average water depth of 28 m (23 m) (cf. *Wind Europe et al.*, 2018; *Wilkes et al.*, 2012). Moreover, the construction and operation of OWFs has reached areas subjected to seasonal stratification, with a possibly significant increase in naturally occurring turbulent mixing locally (*Carpenter et al.*, 2016). In addition to studying naturally occurring turbulence and mixing, OWF induced mixing and scalar transport is addressed in this thesis through the use of observational and numerical methods to focus on the mixing by monopiles, the most used foundation structure in European territory (*Wind Europe et al.*, 2018).

1.3 Thesis overview

The present work aims at studying turbulence and mixing rates in the North Sea under different conditions of stratification (well-mixed to strongly stratified), natural forcing (low and high wind speeds), and anthropogenic forcing (operation of offshore wind farms). For this purpose, datasets collected in three different campaigns conducted between 2014 and 2017 are analyzed in Chapters 3–5.

The next chapter (Chapter 2) gives an overview of the scientific methods and strategy used. It is intended to serve as a broad overview of the approaches that are amply described in the cumulative part of this thesis. Moreover, in the first two publication manuscripts connected to this thesis, two extensive datasets collected by autonomous underwater gliders over dozens of tidal cycles in the German Bight of the North Sea are used to advance the understanding of the variability of turbulence and mixing under different stratification regimes, ranging from a well-mixed regime to a strongly stratified thermocline (Chapter 3). The extent to which background turbulence levels and mixing rates are altered by extreme events such as storms is presented in Chapter 4. In Chapter 4, a dataset of microstructure turbulence recorded by an autonomous underwater glider is combined with evidence of storm-induced marginal stability, in which the complete overturn of the thermally stratified thermocline has been tracked throughout the complete life-cycle of the storm. Chapter 5 presents a publication manuscript in preparation, in which turbulence and mixing generated by offshore wind farms, additional sources of power removal from the flow, is investigated and compared to natural background levels. Chapter 6 summarizes the scientific findings presented throughout this thesis, and provides an outlook for future work.

The scientific findings presented in this thesis have been either published or are being prepared for publication, and are listed below:

1. Schultze, L. K., Merckelbach, L. M., & Carpenter, J. R. (2017). Turbulence and mixing in a shallow shelf sea from underwater gliders. *Journal of Geophysical Research: Oceans*, 122(11), 9092–9109. DOI: 10.1002/2017JC012872.
2. Schultze, L. K., Merckelbach, L. M., & Carpenter, J. R. (2018). Storm-induced turbulence alters shelf sea vertical fluxes. *Submitted for publication.*
3. Schultze, L. K., Merckelbach, L. M., Raasch, S., & Carpenter, J. R. (2018). Increased mixing and turbulence in the wake of offshore wind farm foundations. *In preparation for submission.*

2 Theoretical and Technical Background

The materials and methods used in this PhD project have been extensively described in the scientific publications in chapters 3, 4 and 5, and in their respective supplemental materials. Aiming at avoiding doubling of descriptions, this chapter provides a general background of the equipment and methods applied.

2.1 Turbulence and mixing

Turbulence is a state of the flow that enables rapid heat, momentum and scalar transfer compared to purely molecular diffusion rates due to its irregular, energetic, and rotational nature. The mixing of fluid properties is enhanced through turbulence by two different mechanisms: stirring and diffusion. Through stirring, the boundary area between two fluid volumes is stretched such that the gradients across the fluid volumes is sharpened and the area itself is increased, which in turn leads to increased molecular diffusion. Molecular diffusion works towards the homogenization of the existing gradients and causes mixing, which is irreversible (*Thorpe*, 2007). While turbulence varies among a wide range of time (seconds to years) and spatial scales (millimeters to kilometers), the strong gradients created by stirring occur at very small scales on the order of millimeters, where the kinetic energy of the flow is transformed into heat by viscous dissipation (ε). Although the heat transfer through ε is largely negligible, the energy budget of the ocean is significantly affected by the energy loss caused by turbulence (*Richardson*, 1920; *Thorpe*, 2007).

The vast range of scales found in geophysical turbulent flows and thus the difficulty of resolving these scales with sensors or numerical models has always challenged scientists focused on understanding the role of turbulence and mixing in the energy budget. One common approach to deal with this challenge is to use the Reynolds decomposition (e.g. $\Psi = \langle\Psi\rangle + \Psi'$), a technique in which the expected value of a fluid property $\langle\Psi\rangle$ is separated from its turbulent fluctuations Ψ', thus enabling the study of the overall evolution of a quantity in time (*Reynolds*, 1895). Further, by decomposing the Navier-Stokes equations into a mean and a fluctuating part, the equation for the mean flow becomes:

$$\frac{\partial\langle u_i\rangle}{\partial t} + \langle u_j\rangle\frac{\partial\langle u_i\rangle}{\partial x_j} = -\frac{1}{\rho_o}\frac{\partial\langle p\rangle}{\partial x_i} - g\langle\rho\rangle\delta_{13} + \frac{\partial}{\partial x_j}\left(\frac{\nu\partial\langle u_i\rangle}{\partial x_j} - \langle u_i'u_j'\rangle\right) \tag{1}$$

In Equation 1, u_i stands for a component of the velocity, t is time, x_i the spatial coordinate, p the pressure, ν the kinematic viscosity of seawater, ρ the density, ρ_o a reference density, and g the gravity acceleration. The terms on the left hand side correspond to the inertial forces, and those on the right hand side represent the pressure gradient, buoyancy and viscous forces. The viscous term contains a second order tensor, also known as the Reynolds stress tensor $\rho_o\langle u_i'u_j'\rangle$, which has the role of transferring momentum between the mean flow and turbulence. Moreover, it becomes clear that non-linear turbulent flux terms are present in the mean flow equations, thus introducing the closure problem of turbulence, where the number of unknowns now exceeds the number of equations available to solve them.

Halving the trace of the Reynolds stress tensor gives the turbulent kinetic energy per unit mass $e = 0.5\langle u_i'u_i'\rangle$. Assuming steady state, and that the turbulent kinetic energy of the flow is created and dissipated at the same place (i.e. that it is not advected), we now can write:

$$\frac{De}{Dt} = \mathcal{P} + \mathcal{B} - \varepsilon = 0, \tag{2}$$

where $\mathcal{P} = -\langle u_i' u_j' \rangle \partial \langle u_i \rangle / \partial x_j$ and $\mathcal{B} = -(g/\rho_o)\langle w' p' \rangle$ are the shear production and buoyancy flux terms of e, respectively. The last term, $\varepsilon = 2\nu \langle s_{ij}' s_{ij}' \rangle$ represents the sink, or dissipation, of turbulent kinetic energy, in which $s_{ij}' = 0.5(\partial u_i'/\partial x_j + \partial u_j'/\partial x_i)$ stands for the strain rate tensor of the fluctuating velocities.

The buoyancy term can be a sink (stable stratification) or a source (unstable stratification) of e. If the turbulent kinetic energy e is in steady-state in a stably stratified environment, the ratio of the buoyancy term to the production term gives the flux Richardson number $R_f = -\mathcal{B}/\mathcal{P} = -\mathcal{B}/(-\mathcal{B} + \varepsilon)$. Moreover, *Osborn* (1980) derived the relationship to quantify the maximum turbulent diffusivity in the stably stratified turbulence:

$$K_\rho = \frac{R_f}{1 - R_f} \frac{\varepsilon}{N^2} \sim \gamma \frac{\varepsilon}{N^2}, \tag{3}$$

with the buoyancy frequency squared $N^2 = (g/\rho_o) d\rho/dz$. The mixing efficiency $\gamma = R_f/(1 - R_f)$ is frequently set to 0.2 (*Thorpe*, 2007; *Gregg et al.*, 2012; *Cyr et al.*, 2015), although there is evidence that γ depends on the turbulent state of the flow (*Shih et al.*, 2005; *Bouffard and Boegman*, 2013).

2.2 Turbulence measurements by shear microstructure sensors

In the field, except for Particle Image Velocimetry methods where more components of the shear tensor can be solved for (*Lueck et al.*, 2002; *Thorpe*, 2007; *Burchard et al.*, 2008), turbulence measurements are taken based on the assumption of isotropy. The concept of isotropic turbulence refers to the idea of the energy cascade, in which energy is transferred from the large anisotropic scales towards the small scales where it is dissipated into heat. Larger eddies break up into ever smaller eddies until they become statistically isotropic and therefore do not vary with direction (*Kolmogorov*, 1941). Moreover, in isotropic turbulence, ε reduces to:

$$\varepsilon = \frac{15}{2} \nu \left\langle \left(\frac{\partial u'}{\partial z} \right)^2 \right\rangle = \frac{15}{2} \nu \int_0^\infty \Phi(k) dk, \tag{4}$$

where only one component of the shear is needed to obtain the rate of dissipation of turbulent kinetic energy. Further, in $\langle (\partial u'/\partial z)^2 \rangle$, any component of shear, i.e. any spatial derivative in a direction normal to its own can be used (*Thorpe*, 2007; *Lueck*, 2013). The dissipation ε can be then obtained by integrating the power spectrum of shear, where $\Phi(k)$ in Equation 4 represents the power spectrum in wavenumber space k.

Shear microstructure measurements are commonly performed by either hot-film anemometers or by air-foil shear probes, the latter being the most used for capturing the small-scale velocity fluctuations in the flow (*Lueck et al.*, 2002). In the following, focus is given to the air-foil shear probes, which are used throughout the experiments reported in this thesis. The shear probes carry a piezo-ceramic beam protected by a silicone tip and can be mounted on a free-falling microstructure profiler, or on a microstructure package that is attached to autonomous underwater gliders (Figure 2.1, Chapter 2.2.1). In short, as the instrument travels through water at a given velocity, the cross-stream fluctuations in the flow will hit the air-foil shear probes creating a force on the piezo-ceramic beam. The tilt of the beam creates a pressure difference between the side where the sensor is

Figure 2.1: Autonomous underwater glider with a microstructure package mounted on its top. Two microstructure shear sensors (white tips) and two microstructure temperature sensors (black tips) are fixed in the front. A transparent plastic cap is protecting the sensors prior to deployment. Picture by Thomas Wasilewski (2016).

being hit and the other side, the net force of which is detected from the production of an electric charge. The cross-stream fluctuation can be then calculated by dividing the electric charge by the velocity of the instrument along the axis. The data set collected is therefore in the time domain, and has to be converted to wavenumber space (Equation 4). This is done assuming Taylor's hypothesis of frozen turbulence, which implies that the temporal rate of change of the quantity of interest is significantly smaller than the change measured due to spatial gradients. Specific details on the calculation of ε from our microstructure data sets are given in Chapter 3.

2.2.1 Autonomous underwater gliders

The gliders used in this work are Teledyne Webb Research Slocum Electric ocean gliders. Ocean gliders are autonomous vehicles that move in a sawtooth-like pattern by adjusting their buoyancy and use their wings, hull, and tail fin to provide the lift required to move horizontally (*Merckelbach et al.*, 2010) (Figure 2.1).

The gliders were equipped with conductivity, depth and temperature sensors (Seabird, SBE41 CTD) measuring at 0.5 Hz. All gliders also carried an altimeter (AIRMAR Technology), a navigation pressure sensor (Micron Instruments, MP50-2000), and an attitude sensor (TCM3) that measured pitch and roll. Communication was ensured by an Iridium antenna and a global positioning system (GPS).

Each of the gliders had a neutrally buoyant microstructure instrument package MicroRider-1000LP (MR, manufactured by Rockland Scientific International) mounted on its top that is manufactured to carry orthogonally positioned air-foil shear probes (e.g. SPM-38), fast response thermistors (e.g. FP07), a pressure transducer, a vibration sensor and an inclinometer.

2.3 Numerical simulations of turbulent flows

The extent to which field measurements can be used to analyze a specific phenomenon is constrained by their ability to discern this phenomenon from natural variability. As for the third goal proposed in this thesis, field measurements in the wake of offshore wind farm structures are challenging to interpret (*Floeter et al.*, 2017), thus the use of a turbulence model to investigate the contribution of single OWF structures to turbulence and mixing is desirable.

The lack of a general analytical solution to the Navier-Stokes equations (cf. Section 2.1) has led to the development of models that solve the equations of motion numerically based on predefined initial and boundary conditions (*Pope*, 2000). There are three basic branches of models widely used in computational fluid dynamics, namely the Direct Numerical Simulations (DNS), Large-Eddy Simulations (LES) and models based on the Reynolds Averaged Navier-Stokes equations (RANS). These models differ from one another with respect to the level they are able to describe the flow and thus accuracy, the computational cost, and therefore the range of applicability. On the one side, RANS models are computationally inexpensive and applicable for a large range of Reynolds numbers suitable for engineering and oceanographic applications, while DNS simulations are costly and focus on small domains and Reynolds numbers due to computational limitations that persist to date (*Pope*, 2000). On the other side, whilst DNS simulations are able to fully resolve the equations of motion in time and space numerically, RANS models rely on parameterization schemes of which output is by definition time averaged and do not provide any explicit information on the turbulent field (*Pope*, 2000). Moreover, the parameterization of turbulent motion in RANS models is sensitive to the structure of the water column, e.g. stratification, which presents a drawback when conducting mixing studies.

The idea of LES goes back to *Smagorinsky* (1963) and is based on the Kolmogorov theory (*Kolmogorov*, 1941) that assumes that the production of energy and its dissipation occur at different spatial scales. Large-eddy simulations provide a compromise between DNS and RANS, in which the large energy-containing eddies are explicitly resolved and the impact of the small scales is parameterized with a statistical subgrid-scale model (*Maronga et al.*, 2015). The scale separation in LES is done by defining a cut-off length, which is often set to the grid spacing to save computational resources. The cut-off length separates a quantity $\psi(x,t)$ into a three-dimensional resolved-scale component $\bar{\psi}(x,t)$, and a subgrid-scale term $\psi''(x,t)$, and thus $\psi''(x,t) = \psi(x,t) - \bar{\psi}(x,t)$. The computational cost of LES is still high compared to RANS models, however computer clusters are able to support LES simulations at realistic Reynolds numbers, which generally have higher accuracy and provide information on the turbulent eddies.

The study of the impact of OWF monopiles on turbulence and mixing in a neutrally stratified flow is essentially the study of the flow past a circular cylinder, a classical problem in fluid dynamics that has been analyzed both experimentally (*ESDU*, 1985; *Schlichting and Gersten*, 2000; *Eça et al.*, 2014) and numerically with RANS, DNS and LES (*Eça et al.*, 2014). The addition of different strengths of stratification to the problem has been much less studied (*Rennau et al.*, 2012), but it is nevertheless essential for the parameterization of OWFs in larger-scale models. Given the unfeasibility of conducting DNS for large Reynolds numbers with obstacles (*Rosetti et al.*, 2012), and the difficulties of RANS models in dealing with stratification and the flow around structures, LES simulations are used to tackle this research question.

2.4 Parallelized Large-Eddy Simulation Model (PALM)

This section provides a summary of the most relevant characteristics of the LES model applied, the Parallelized Large-Eddy Simulation Model (PALM) for atmospheric and oceanic flows, without aiming for completeness. A detailed description of PALM can be found in *Maronga et al.* (2015) and references therein. The PALM edition used to perform the simulations presented in this thesis is version 4.0, revision 2504M.

The PALM code is written in Fortran and is based on the non-paralellized LES scripts developed at the Leibniz Universität Hannover to study atmospheric turbulence. The first version of PALM has been documented in 1991 (*Raasch and Etling*, 1991) and became parallelized through the use of a message passing interface in 2001 (*Raasch and Schröter*, 2001). PALM has been in continuous development and includes the possibility of performing high resolution oceanic simulations that may include topography, vertical stratification, and a passive scalar, among others (*Maronga et al.*, 2015).

2.4.1 Governing equations

In the ocean mode, the default version of PALM solves the prognostic equations for the velocity components u_i, potential temperature θ, salinity s, the subgrid-scale turbulent kinetic energy e_{SGS} and a passive scalar c. The Navier-Stokes equations of conservation of momentum, mass, potential temperature, salinity and other scalars in a viscous fluid are used in Boussinesq-approximated form and subsequently filtered over a grid volume, an approach through which the discretization works as a Reynolds operator, separating the mean $\overline{\psi}$ of the grid volume from the non-resolved local spatial fluctuation ψ'' (*Schumann*, 1973; *Froehlich*, 2006). After the Boussinesq approximation and the filtration, the non-hydrostatic Navier-Stokes equations read as (*Maronga et al.*, 2015):

$$\begin{aligned}\frac{\partial u_i}{\partial t} = -\frac{\partial u_i u_j}{\partial x_j} - \epsilon_{ijk} f_j u_k + \epsilon_{i3j} f_3 u_{g,j} - \frac{1}{\rho_0}\frac{\partial (p^* + 2\rho_0 e_{\mathrm{SGS}}/3)}{\partial x_i} \\ -g\frac{\rho - \langle\rho\rangle}{\langle\rho\rangle}\delta_{i3} - \frac{\partial}{\partial x_j}\left(\overline{u_i'' u_j''} - \frac{2}{3} e_{\mathrm{SGS}}\delta_{ij}\right)\end{aligned} \tag{5}$$

$$\frac{\partial u_j}{\partial x_j} = 0 \tag{6}$$

$$\frac{\partial \theta}{\partial t} = -\frac{\partial u_j \theta}{\partial x_j} - \frac{\partial \overline{u_j'' \theta''}}{\partial x_j} \tag{7}$$

$$\frac{\partial s}{\partial t} = -\frac{\partial u_j s}{\partial x_j} - \frac{\partial \overline{u_j'' s''}}{\partial x_j} \tag{8}$$

$$\frac{\partial c}{\partial t} = -\frac{\partial u_j c}{\partial x_j} - \frac{\partial \overline{u_j'' c''}}{\partial x_j} \tag{9}$$

In the equations above, time is given by t, the indices are $i, j, k \in [1, 2, 3]$, the direction in space is indicated by x_i, ρ is the density of sea water, and p^* is the perturbation pressure. Note that, except for the subgrid-scale flux quantities, the overbars have been omitted for better readability. The subscript 0 stands for the sea surface value and the angle brackets stand for a horizontal average of the domain. The gravitational acceleration is given by g, and the Coriolis force is $f_i = (0; 2\Omega\cos\varphi; 2\Omega\sin\varphi)$, with the latitude φ

and the angular velocity of the planet Ω. The density of seawater is calculated based on the method by *Jackett et al.* (2006) and depends on θ, s, and the pressure p.

Equations 5 – 9 show that the filtering step yields second-order moments, e.g. $\tau_{ij} = \overline{u_i'' u_j''}$, with subgrid-scale quantities that have to be parameterized. This is done using the closure proposed by *Deardorff* (1980) and modified by *Moeng and Wyngaard* (1988); *Saiki et al.* (2000), which assumes that the energy transport by the unresolved small-scale turbulent eddies is proportional to the local gradients of the averaged variables (*Maronga et al.*, 2015):

$$\overline{u_i'' u_j''} - \frac{2}{3} e_{\mathrm{SGS}} \delta_{ij} = -K_{\mathrm{m}} \left(\frac{\partial u_i}{\partial x_j} + \frac{\partial u_j}{\partial x_i} \right) \tag{10}$$

$$\overline{u_i'' \theta''} = -K_{\mathrm{h}} \frac{\partial \theta}{\partial x_i} \tag{11}$$

$$\overline{u_i'' s''} = -K_{\mathrm{h}} \frac{\partial s}{\partial x_i} \tag{12}$$

$$\overline{u_i'' c''} = -K_{\mathrm{h}} \frac{\partial c}{\partial x_i} \tag{13}$$

with $K_{\mathrm{m}} = 0.1 l (e_{\mathrm{SGS}})^{1/2}$ and $K_{\mathrm{h}} = (1 + 2l/\Delta) K_{\mathrm{m}}$ being the turbulent diffusivity of momentum and heat, respectively, and the grid size $\Delta = (\Delta x \Delta y \Delta z)^{1/3}$. The mixing length l, the subgrid-scale turbulent kinetic energy, e_{SGS}, and the subgrid-scale dissipation of turbulent kinetic energy, ϵ, are calculated as:

$$l = \begin{cases} \min\left(\Delta, 1.8z, 0.76 e_{\mathrm{SGS}}^{1/2} \left(\frac{g}{\rho_0} \frac{\partial \rho}{\partial z}\right)^{-1/2}\right), & \text{if stably stratified, else} \\ \min(\Delta, 1.8z) \end{cases} \tag{14}$$

$$\frac{\partial e_{\mathrm{SGS}}}{\partial t} = -u_j \frac{\partial e_{\mathrm{SGS}}}{\partial x_j} - \tau_{ij} \frac{\partial u_i}{\partial x_j} + \frac{g}{\rho_0} \overline{u_3'' \rho''} - \frac{\partial}{\partial x_j} \left\{ 2 K_m \frac{\partial e_{\mathrm{SGS}}}{\partial x_j} \right\} - \epsilon \tag{15}$$

$$\epsilon = \left(0.19 + 0.74 \frac{l}{\Delta}\right) \frac{e_{\mathrm{SGS}}^{3/2}}{l} \tag{16}$$

2.4.2 Numerical modeling

PALM uses a staggered Arakawa C-grid with equal horizontal grid spacings and makes use of the finite differences method to approximate the differential equations. Simulations with topography/obstacles may use the advection scheme defined by *Piacsek and Williams* (1970) or *Wicker and Skamarock* (2002) to discretize the advection of momentum and scalar quantities in the filtered Navier-Stokes equations (Equations 5 – 9). Because the numerical dissipation of the method described by *Piacsek and Williams* (1970) is considerably larger than in the *Wicker and Skamarock* (2002) scheme, the latter is used in this thesis in combination with the 3^{rd} order Runge-Kutta time integration scheme (*Maronga et al.*, 2015).

To comply with the incompressibility requirement of the Boussinesq equations (Equations 5 – 9), a method to predict and correct for the divergence generated in the flow field is needed as the time integration of Equation 5 doesn't consider the continuity equation. The Poisson equation and the "iterative multigrid scheme" are the methods implemented in PALM at the moment to correct for divergence, whereby the latter does not require periodic lateral boundaries (*Maronga et al.*, 2015) and is therefore used in this thesis as a result of the boundary conditions defined (cf. Boundary conditions, below).

2.4.3 Topography

PALM allows the addition of stationary topography or obstacles to the simulations that may be either in suspension ("tunnels") or completely bound to the bottom of the domain ("conventional buildings"). The requirement for the inclusion of obstacles is that their shape is adapted to fill single grid cells such that a grid volume is either replete by fluid or by obstacle (*Maronga et al.*, 2015). The realization of topography follows the method described in *Briscolini and Santangelo* (1989); *Maronga et al.* (2015) and the domain is subdivided into three groups or sub-domains: (1) grid volumes located in the free fluid, where the standard PALM scripts are executed to calculate the prognostic terms; (2) grid volumes next to the walls of the obstacle, in which a parameterization (e.g. wall functions) is used; and (3) grid volumes within the obstacles that use the standard PALM code but are subsequently annulled i.e. excluded from the calculations (*Maronga et al.*, 2015). In this study, the monopile is therefore approximated to a Cartesian grid such that it resembles a monopile (cf. Section 5).

2.4.4 Boundary conditions

The choice of the boundary conditions, as well as that of the initial conditions, depend on the research problem being studied. PALM enables the Dirichlet or Neumann boundary conditions for the velocity components at the top and bottom boundaries. Setting Dirichlet boundary conditions (no-slip) on the top and bottom of the domain would resemble a channel flow, whereas Neumann boundary conditions (free-slip) maintain a free stream at the boundaries (*Maronga et al.*, 2015). In this thesis, free-slip conditions are set at the sea surface. At the sea bed, the no-slip conditions are chosen to allow the assessment of bottom boundary layer turbulence in addition to the foundation effects. Further, no-slip conditions generate bottom boundary layer turbulence if perturbations are present, such as through velocity fluctuations from the monopile, or random noise added to the flow. To isolate turbulence and mixing generated by the monopile from those caused by friction at the sea bed, twin simulations with identical conditions but without topography are conducted, thus enabling the differentiation between both sources of turbulence (cf. Section 5). The boundary conditions for the subgrid-scale turbulent kinetic energy, potential temperature and salinity are defined as Neumann conditions at the top and bottom boundaries of the domain.

There are two possible settings for the lateral boundary conditions in PALM: (1) periodic in all horizontal directions or (2) non-periodic (Dirichlet/radiation), which can be set either on the left and right domain walls or on the front and back walls. The periodic boundary conditions yield an infinite domain that is laterally recycled. In turn, the non-periodic conditions are characterized by a laminar or turbulent inflow and an open outflow (*Maronga et al.*, 2015). To analyze the effect of a single monopile on turbulence and mixing, non-periodic boundary conditions are used in this thesis.

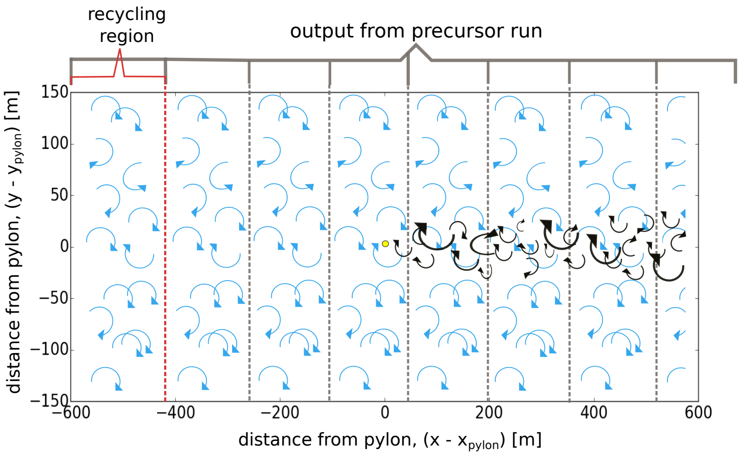

Figure 2.2: Sketch of the initialization of the main run using the output obtained in the precursor run. The domain of the precursor run is commonly smaller than that of the main run. In this case, the turbulence formed in the precursor run is cyclically pasted in the main run domain at the first time step. Turbulence is continuously recycled in the recycling region (red). The axis have been centered to the monopile position.

2.4.5 Precursor run and initial conditions

To enable the comparison between the simulations with and without the monopile, a turbulent inflow with bottom boundary layer turbulence is required when using non-periodic boundary conditions, otherwise a very long domain would be needed for turbulence to develop. A turbulent inflow is implemented in PALM through a two-step process based on the method described by *Lund et al.* (1998) and modified by *Kataoka and Mizuno* (2002). Prior to the main run, which is used for scientific analysis, a precursor run with periodic lateral boundary conditions has to be carried out. In the precursor run, a homogeneous current of 0.4 m/s is defined. Temperature stratification is horizontally homogeneous and decreases linearly with depth by 1.5 – 4.0°C between the sea surface and approximately 10 m.

Once the precursor run has become quasi-stationary and turbulence is fully developed, information on the velocity and other scalar quantities are saved and used in the main run. The model domain in the precursor run can be significantly smaller than in the main run. In this case, the 3D data recorded is repeatedly mapped in the main run until its domain is filled (Figure 2.2). At the beginning of the main run, the turbulence formed in the precursor run is recycled at a given distance from the inflow (Figure 2.2). Salinity is kept homogeneous in all simulations.

3 Turbulence and mixing in a shallow shelf sea from underwater gliders

This chapter is a reprint of the manuscript "Turbulence and mixing in a shallow shelf sea from underwater gliders" that has been published in the Journal of Geophysical Research.

Citation: Schultze, L. K. P., Merckelbach, L. M., & Carpenter, J. R. (2017). Turbulence and mixing in a shallow shelf sea from underwater gliders. Journal of Geophysical Research: Oceans, 122, 9092–9109. https://doi.org/10.1002/2017JC012872.[1]

Keypoints

- Two extensive continuous datasets spanning 29 days use gliders to quantify turbulence in a shallow (40 m) energetic shelf sea.
- Turbulent fluxes within stratification are sensitive to the thermocline definition, mixing efficiency and intermittent turbulent events.
- A tendency for low bulk Richardson numbers to exhibit higher turbulence levels was observed, however no clear relation could be drawn.

3.1 Abstract

The seasonal thermocline in shallow shelf seas acts as a natural barrier for boundary-generated turbulence, damping scalar transport to the upper regions of the water column, and controlling primary production to a certain extent. To better understand turbulence and mixing conditions within the thermocline, two unique 12- and 17-day datasets with continuous measurements of the dissipation rate of turbulent kinetic energy (ε) collected by autonomous underwater gliders under stratified to well-mixed conditions are presented. A highly intermittent ε signal was observed in the stratified thermocline region, which was mainly characterized by quiescent flow (turbulent activity index below 7). The rate of diapycnal mixing remained relatively constant for the majority of the time with peaks of higher fluxes that were responsible for much of the increase in bottom mixed layer temperature. The water column stayed predominantly strongly stratified, with a bulk Richardson number across the thermocline well above 2. A positive relationship between the intensity of turbulence, shear and stratification was found. The trend between turbulence levels and the bulk Richardson number was relatively weak, but suggests that ε increases as the bulk Richardson number approaches 1. The results also highlight the interpretation difficulties in both quantifying turbulent thermocline fluxes, as well as the responsible mechanisms.

3.2 Introduction

Stratification in shelf seas occurs when wind stress and bottom friction do not compete sufficiently against solar heating at the ocean surface to mix the water column (*Pingree and Griffiths*, 1978; *Simpson et al.*, 1990). Except for blooms, enhanced phytoplankton growth in stratified continental shelf seas concentrates in the subsurface chlorophyll maximum (SCM), which is usually situated in the euphotic, temperature stratified region of the water column. In this region, the thermocline, conditions for phytoplankton growth are often favourable due to the existing vertical gradients of light intensity, nutrients, O_2 and CO_2 (*Ross and Sharples*, 2007; *Simpson and Sharples*, 2012). On a global scale, such rates of primary productivity in the SCM are thought to contribute significantly to both the fixation of carbon (*Holligan et al.*, 1984; *Richardson et al.*, 1998; *Ross and Sharples*, 2007), and biological production (*Muller-Karger et al.*, 2005; *Simpson and Sharples*, 2012). Understanding the mechanisms through which different scalars are transported to and across the stratified thermocline are therefore of major importance.

In several areas of the German Bight of the North Sea (Figure 3.1), the water column stratifies during the summer months and a thermocline separates the surface and bottom layers, which remain well-mixed to a large extent (*van Leeuwen et al.*, 2015). The upward nutrient and downward heat transport across the thermocline in shelf seas are thought to be dominated by low energy mechanisms other than directly by the highly energetic barotropic tide (*Palmer et al.*, 2008; *Rippeth*, 2005; *van Haren et al.*, 1999). *van Haren et al.* (1999) suggested that the dissipation of breaking internal waves in combination with near-inertial current shear is responsible for mixing and nutrient transport across the thermocline. *Rippeth* (2005) studied mixing in an area of relative smooth topography and identified the breaking of internal tides and near-inertial oscillations as key processes to understand mixing in the thermocline. *Palmer et al.* (2008) analysed a 50-hour dataset of microstructure shear measurements using a vertical free-falling profiler. They suggested that turbulence and mixing across the thermocline in the Celtic Sea are powered by internal waves and near-inertial waves. The most accepted idea on how the energy generated by possible mixing processes is delivered to the thermocline is the transition to turbulent flow through shear instability (*Palmer et al.*, 2008; *Rippeth*, 2005; *van Haren et al.*, 1999; *Burchard and Rippeth*, 2009).

Additional to the naturally occuring mixing processes, the increased interest in renewable energies and the development of the technology to build wind turbines offshore in greater water depths have led to the planning and construction of offshore wind farms (OWFs) at coastal regions (*Carpenter et al.*, 2016; *Ho et al.*, 2016). Turbine foundations generate additional turbulence in the water column that can contribute to mix a stratified regime. This additional mixing of the water column could alter nutrient levels and shift the competitive balance between phytoplankton species, altering phytoplankton growth and community composition, with possible implications for the marine food web and biogeochemical cycles (*Huisman et al.*, 2004; *Lauria et al.*, 1999; *Franks*, 2015; *Carpenter et al.*, 2016). Results from an idealized study by *Carpenter et al.* (2016) suggest that OWFs could significantly impact stratification in the North Sea, given they are built in extensive areas of the shelf. Until 2015, 11 GW of offshore capacity had been installed in Europe, 69% of which is situated in the North Sea (*Ho et al.*, 2016). Of the consented offshore wind farms, 78% of the total capacity is planned to be built in the North Sea, underlining the importance of this shelf sea for offshore development (*Ho et al.*, 2016). To better understand the thermocline fluxes in seasonally stratified shelf seas, which could be altered by OWFs in the near future, the present paper focusses on quantifying turbulence and mixing in the German Bight region of the North Sea, as well as understanding the mechanisms responsible.

Two datasets of microstructure turbulence measurements collected in July – August 2014 and May – June 2015 over 12 and 17 days, respectively, are presented. To our knowledge, this is so far the most extensive dataset of stratified turbulence in a shallow shelf sea. We analyze the dissipation of turbulent kinetic energy in the German Bight region of the North Sea under strongly stratified to well-mixed conditions. Measurements were obtained by autonomous underwater gliders equipped with turbulence microstructure shear sensors. Underwater gliders have been shown to be suitable instruments to study turbulence as they move independently from ships or propellers, reducing the vibration noise in the shear probe measurements (*Wolk and Lueck*, 2009), and are able to reliably measure through long periods of time, even when subjected to adverse weather conditions (*Fer et al.*, 2014; *Palmer et al.*, 2015).

The following section provides an overview of the field measurements, including instrument deployment and relevant instrument details. Data processing is discussed in section 3.4, in which a description of the quality control of glider and microstructure measurements is included. In sections 3.5 and 3.6, results are presented and discussed,

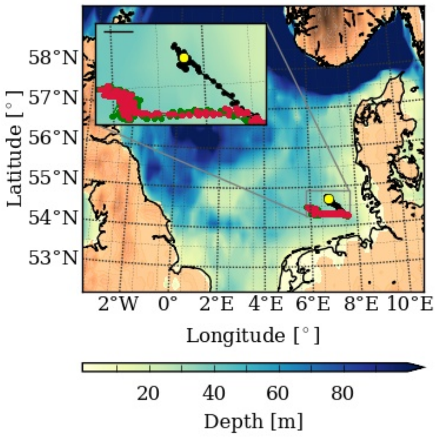

Figure 3.1: Research area of the campaigns in 2014 and 2015. Deployment location and flight paths of Amadeus (C14), Comet (C15) and Sebastian (C15) are shown in black, green and red, respectively. All paths are situated within the German Bight of the North Sea. The location of the ADCP is marked by a yellow dot. The colormap represents the water depth in meters, which has been created using data from the National Centers for Environmental Information (NOAA, http://maps.ngdc.noaa.gov/viewers/wcs-client/). Water depths above 100 m are well outside the study area and are therefore not resolved in this map. The black overbar in the zoomed area indicates a distance of 20 km.

and in section 3.7 the paper is concluded providing insights on the mixing processes in the study area.

3.3 Overview of field measurements

To study turbulence and mixing in shallow shelf seas, measurements from two field campaigns conducted in the German Bight of the North Sea are presented (Figure 3.1). The first field campaign (C14) took place between July 28 and August 18 in 2014. On August 9, the Storm Bertha reached the studied region and was able to mix the water column thoroughly, drastically affecting the mixing conditions in the area. To concentrate on the mechanisms responsible for mixing under representative conditions, only the data collected before the storm (12 days) is analysed. The sampling location was situated between 6.67°E, 54.26°N and 7.54°E, 54.76°N. Relevant instruments for this work are one Teledyne Webb Research Slocum Electric ocean glider (Amadeus) with a MicroRider-1000LP (MR, manufactured by Rockland Scientific International) mounted on its top, and one acoustic doppler current profiler (ADCP, RDI 600-kHz Workhorse Sentinel), which was mounted on the sea floor in 40 m water depth. The ADCP was positioned close to the buoy station Nordseeboje 3 (NSB3) at 54.68°N, 6.78°E and sampled horizontal velocities over nearly the whole water column range (5 to 38 m).

Further, within the studied period in 2014, we have conducted "spiral missions", the beginning of which is indicated in Figure 3.5 by a dashed line between August 4 – 5. During this period, the glider was configured with a tail rudder position fixed to starboard, causing it to profile up and down in spirals with a diameter of about 10 – 12 m. In this setup, the glider moves horizontally with the mean velocity of the water column, which renders the parameters measured by the glider observed in an approximately Lagrangian fashion.

The second campaign (C15) was conducted between May 21 and June 6 in 2015, in which two Teledyne Webb Research Slocum Electric ocean gliders (Comet and Sebastian) were deployed, each carrying a MR. The sampling area was located between 5.82°E, 54.24°N and 7.62°E, 54.52°N. The exact routes and instrument positions are shown in Figure 3.1.

All three gliders carried custom Sea-Bird Electronics conductivity, depth and temperature sensors (Seabird SBE41 CTD) that measure at a frequency of 0.5 Hz. The gliders are further equipped with an attitude sensor (TCM3), an altimeter (AIRMAR Technology), a navigation pressure sensor (Micron Instruments, MP50-2000), an Iridium modem and a global positioning system (GPS). On both campaigns, the gliders surfaced approximately every three hours at which point the glider position is acquired via GPS. To reduce glider vibrations that can contaminate the shear probe measurements, the battery position was fixed for all gliders during up- and downcasts.

The MR, a microstructure instrument package, carried two orthogonally positioned air-foil shear probes (SPM-38, 512 Hz), two thermistors in C14 (FP07, 512 Hz) and one thermistor in C15 (FP07, 512 Hz), a pressure transducer (64 Hz), a vibration sensor (64 Hz) and an inclinometer (64 Hz).

3.4 Data processing

3.4.1 Glider dynamics and CTD measurements

In contrast to vertical profilers, the glider moves through the water column in a sawtooth pattern. Hence, the speed along the microstructure sensors (U_{g}) cannot be obtained trough the rate of change of pressure, but it needs to be estimated accounting for the glide angle. It is necessary to estimate U_{g} to obtain the dissipation of turbulent kinetic energy (ε) from shear probe measurements. Glider measurements are obtained from up- and downcasts, and understanding the flight behavior during these different casts is an active area of research. Therefore, since the procedure to calculate ε from microstructure shear sensors mounted on gliders is novel, and the conventions to process this type of dataset are still under development, the present section describes the steps taken to obtain data for the scientific analysis.

Previous studies (e.g., *Fer et al.*, 2014; *Palmer et al.*, 2015) have used the hydrodynamic glider flight model of *Merckelbach et al.* (2010) to obtain U_{g}. The flight model assumes steady flight, that is, an equilibrium between buoyancy, drag and lift forces, and takes the observed in-situ density, measured pitch and buoyancy drive as input parameters. The model yields the glider speed along the glide path and accounts for the angle of attack, a small, but non-zero angle between the glide angle and the pitch angle. Especially in stratified regions, however, the assumption of steady flight is questionable, and the model results become less accurate. In order to retain the dynamic response of the glider due to sudden changes in forcing, for example when passing a pycnocline, U_{g} is calculated from the depth rate, computed from the measured pressure, and the glide angle. Herein, the glide angle is composed of the measured pitch angle and the angle of attack, with the latter being computed using the steady-state model. It is necessary to account for the effect of the angle of attack, as ignoring it could overestimate the glider speed through water by an amount of 2 – 4 cms^{-1} (*Merckelbach et al.*, 2010), or about

10% of the glider speed. Note that in this procedure it is tacitly assumed that the vertical water velocities are equal to zero.

Table 3.1: Average values and one standard deviation of flight parameters (glider's along path velocity (U_{g}), vertical glider velocity (w_g), angle of attack (α) and pitch angle (θ_{g})) for field campaigns C14 and C15

Campaign/ glider	Profile	U_{g} [ms^{-1}]	w_g [ms^{-1}]	α [°]	θ_{g} [°]
C14					
Amadeus	upcasts	0.36 (0.05)	-0.14 (0.05)	-3.46 (0.61)	-19.74 (3.81)
Amadeus	downcasts	0.21 (0.05)	0.08 (0.03)	3.33 (0.47)	21.00 (2.97)
C15					
Comet	upcasts	0.26 (0.04)	-0.11 (0.04)	-4.05 (0.50)	-21.70 (2.17)
Comet	downcasts	0.37 (0.04)	0.16 (0.05)	4.02 (0.45)	21.80 (1.96)
Sebastian	upcasts	0.29 (0.03)	-0.12 (0.04)	-2.88 (0.28)	-23.86 (2.62)
Sebastian	downcasts	0.39 (0.04)	0.18 (0.06)	2.69 (0.23)	25.72 (2.38)

Average values of pitch (θ_{g}), angle of attack (α), glider velocities (U_{g}) and vertical glider velocities (w_g) are shown in Table 3.1.

The conductivity signal measured by CTD sensors in the presence of sharp temperature gradients tends to be corrupted due to thermal lag effects in the conductivity cell (*Lueck and Picklo*, 1990). This in turn compromises the accuracy of salinity and therefore density estimates in thermoclines. General methods to correct for the thermal inertia have been proposed by e.g., *Lueck and Picklo* (1990) and *Morison et al.* (1994). Correction methods for glider CTDs and, in particular, unpumped CTDs have been proposed by *Garau et al.* (2011). Nevertheless, due to the low sample rate of 0.5 Hz, the correction of the thermal lag effects turned out to be problematic for the current dataset due to the sharp and strong thermocline present in C14. However, considering that the variance of the density profiles in the study area is dominated by temperature, we opted to apply a simplified technique for the calculation of density. Density is estimated as described in *Carpenter et al.* (2016), in which the accurate salinity estimates from the the top and bottom mixed layers are used to calculate the change in density across the water column. Density profiles are then generated by using top and bottom density incremented by a proportional density contribution, which preserves the vertical shape of the temperature profiles.

3.4.2 Calculating the dissipation of turbulent kinetic energy

Estimates of U_{g} are used in the calculation of shear microstructure from the air-foil shear probes, from which the dissipation rates of turbulent kinetic energy are obtained. An air-foil shear probe detects velocity fluctuations perpendicular to its pointing direction by means of a piezo-ceramic beam that is able to sense a net force exerted by the cross-stream flow, producing an electric charge. Shear measurements are obtained using the measured voltage, the sensitivity of the shear probes and the velocity of the glider (*Lueck et al.*, 2002).

Assuming isotropic turbulence, the dissipation of turbulent kinetic energy can be calculated from the time series of one component of the shear tensor after a spectral analysis (fast Fourier transform), in which the variance of the spectra is estimated through the use of the Parseval theorem (described mathematically below in Equation 17). For the spectral analysis, a sample length of 12 s was chosen, and a total of 5 half-overlapping segments of 4 s each generated 5 shear spectra, which were averaged together for the calculation of one ε estimate. Thus, one ε estimate was obtained every 2 – 4.5 m horizontally and 0.95 – 2.5 m vertically on average, depending on the glide angle and on the glider along path velocity. Using Taylor's frozen turbulence hypothesis, it is assumed that the temporal rate of change of the quantity of interest is significantly less than its change attributed to spatial gradients, which enables the conversion of shear spectra in the frequency domain, $\Phi(f)$, into a spatial, wavenumber domain, $\Phi(k)$. For one ε_j estimate, a shear spectrum is integrated over a determined wavenumber range $[k_{\mathrm{min_j}}, k_{\mathrm{max_j}}]$. The integrated values are multiplied by the kinematic viscosity of seawater ν, and a numerical scale factor to account for the assumption of isotropy (*Wolk et al.*, 2002; *Lueck et al.*, 2002):

$$\varepsilon_j = \frac{15}{2}\nu\overline{\left(\frac{\partial u_j}{\partial x}\right)^2} = \frac{15}{2}\nu\int_{k_{\mathrm{min_j}}}^{k_{\mathrm{max_j}}}\Phi_j(k)dk\,, \tag{17}$$

where the subscript j denotes the two different shear probes, and ε without subscript denotes the final dissipation estimates that are used in the scientific analysis.

The preliminary estimate of ε_j integrates the measured shear spectrum ($\Phi_j(k)$) from the lowest available wavenumber ($k_{\mathrm{min_j}}$) to a maximum wavenumber ($k_{\mathrm{max_j}}$), which is determined via an algorithm used to identify the spectral minimum through a polynomial fit (*Lueck*, 2013). This range of integration is chosen to eliminate contamination from instrumental noise at high frequencies. Based on this preliminary estimate, the integration range is iteratively adjusted by comparing the shear spectrum with the fitted form of the Nasmyth spectrum (*Wolk et al.*, 2002). The upper limit of integration, $k_{\mathrm{max_j}}$, is increased (decreased) if the shear spectrum is well above (below) the theoretical Nasmyth spectrum. In general, the higher (lower) the quality of the shear spectra obtained, the closer (farther apart) $k_{\mathrm{max_j}}$ is going to be to the wavenumber at which the spectrum ceases to roll-off and is dominated by instrumental noise (k_{noise}, Figure 3.2). The k_{noise} wavenumber has been observed to vary among different orders of magnitude of ε (*Nasmyth*, 1970; *Bluteau et al.*, 2016; *Fer et al.*, 2014) and was determined here by averaging the shear spectra over the complete dataset in bins of ε (for reference, see Figure 9 in *Fer et al.* (2014)).

Interferences in the shear signal may occur due to motions of the glider. To account for this, the algorithm suggested by *Goodman et al.* (2006) was used prior to the evaluation of the quality of the shear spectra and the estimation of dissipation. Differences in ε estimates obtained with and without the use of the Goodman algorithm were on average within a factor of 2 and are presented in section 3.4.4. Furthermore, to ensure that only high quality data would be included in the scientific analysis, several steps were taken to monitor the measurements, which are described in the following subsection.

3.4.3 Identification of reliable ε estimates and criteria for data selection

In the following we discuss the steps taken to control the quality of the acquired data, including a discussion on the glider velocities through water, vertical velocities and the quality of the measured shear spectra.

Due to the intermittency of turbulence and other sources of error, shear spectra are not expected to agree perfectly with the empirical Nasmyth spectra (*Fer et al.*, 2014). To distinguish dissipation estimates generated from shear spectra that considerably deviate from the empirical Nasmyth spectra from the estimates generated by well-fitting spectra in an automated manner, we propose the empirically defined index of spectral agreement:

$$I_{\mathrm{SA}} = \left[\frac{1}{n} \cdot \sum_{\mathrm{i=1}}^{\mathrm{n}} \log_{10}^{2}\left(\frac{\Phi_{\mathrm{SH_i}}}{\Phi_{\mathrm{N_i}}}\right)\right]^{1/2} \cdot \frac{k_{\mathrm{noise}}}{k_{\mathrm{max}}}\,, \tag{18}$$

where $\Phi_{\mathrm{SH_i}}$ and $\Phi_{\mathrm{N_i}}$ correspond to the shear spectrum and the corresponding value from the fitted Nasmyth spectrum, which are compared against each other from k_{min} ($i = 1$) until k_{noise} ($i = n$). In equation (18), subscripts j have been dropped for convenience. The factor with the square root in equation (18) corresponds to a normalized root mean squared error between the shear and Nasmyth spectra in logarithmic space, whereas the second factor assesses the bandwidth of the shear spectra by comparing k_{noise} to k_{max}. The lower the value of I_{SA}, the better the agreement with the Nasmyth spectrum is expected to be. By manually comparing the spectra with I_{SA}, a threshold $I_{\mathrm{SA}} < 1$ was found to effectively reject "low-quality" spectra (e.g. Figure 3.2).

From the previous subsection, we know that two independent values of ε are generated simultaneously as a result of the orthogonally positioned shear sensors. These two different ε_j estimates are averaged together if they agree up to a factor of four. Otherwise, the ε_j estimate whose shear spectrum is in closest agreement with its respective Nasmyth spectrum is chosen. If the shear spectra from both estimates are of bad quality, the estimate is annulled. Dissipation estimates above 10^{-5} Wkg^{-1} were mainly characterized by overly noisy spectra, whereas dissipation estimates below 10^{-11} Wkg^{-1} were related to spectra with extremely weak curvature, in which the transition from the inertial subrange to the dissipation range could be barely detected. Therefore, for $\varepsilon_j < 10^{-11}$ Wkg^{-1} and for $\varepsilon_j > 10^{-5}$ Wkg^{-1}, dissipation estimates were not considered in the scientific analysis. In total, the amount of rejected ε associated with unreliable shear spectra was 3.4% for Amadeus (C14), 1.5% for Comet (C15) and 1.3% for Sebastian (C15), which points to the high quality of the data collected by the gliders.

The validity of the assumption of Taylor's hypothesis of frozen turbulence in the calculation of ε and the implications of notably high or low vertical glider velocities have been amply discussed by *Fer et al.* (2014) and is briefly addressed in this subsection. When discussing glider velocities in the context of the estimates of dissipation of turbulent kinetic energy, U_{g} and the vertical glider velocity, w_g, have been averaged over the sample length used for producing an ε estimate.

To test the ε estimates against Taylor's hypothesis, a threshold value of $U_{\mathrm{g}} \geqslant 20u_t$ was chosen for up- and downcasts based on the same analysis performed by *Fer et al.* (2014), where u_t is defined as the turbulent velocity scale (cf. Appendix A). In our dataset, high values of the angle of attack did not seem to affect directly the dissipation rates. Therefore, we set a limit of $|\alpha| < 20°$, which is the standard value suggested by the manufacturers for the proper functioning of the air-foil shear probes (*Lueck*, 2013). As in *Fer et al.* (2014), the thresholds for vertical velocities were set to a minimum of 0.04 ms^{-1} and a maximum of 0.5 ms^{-1}. As an example, after data processing, Amadeus (C14) had 3.4% of its data points removed in the upcasts, 9.6% of which were rejected for failing Taylor's hypothesis. A total of 52528 data points collected during Amadeus' upcasts were left for scientific analysis. The percentages of the rejected data for all gliders are listed in Table 3.2.

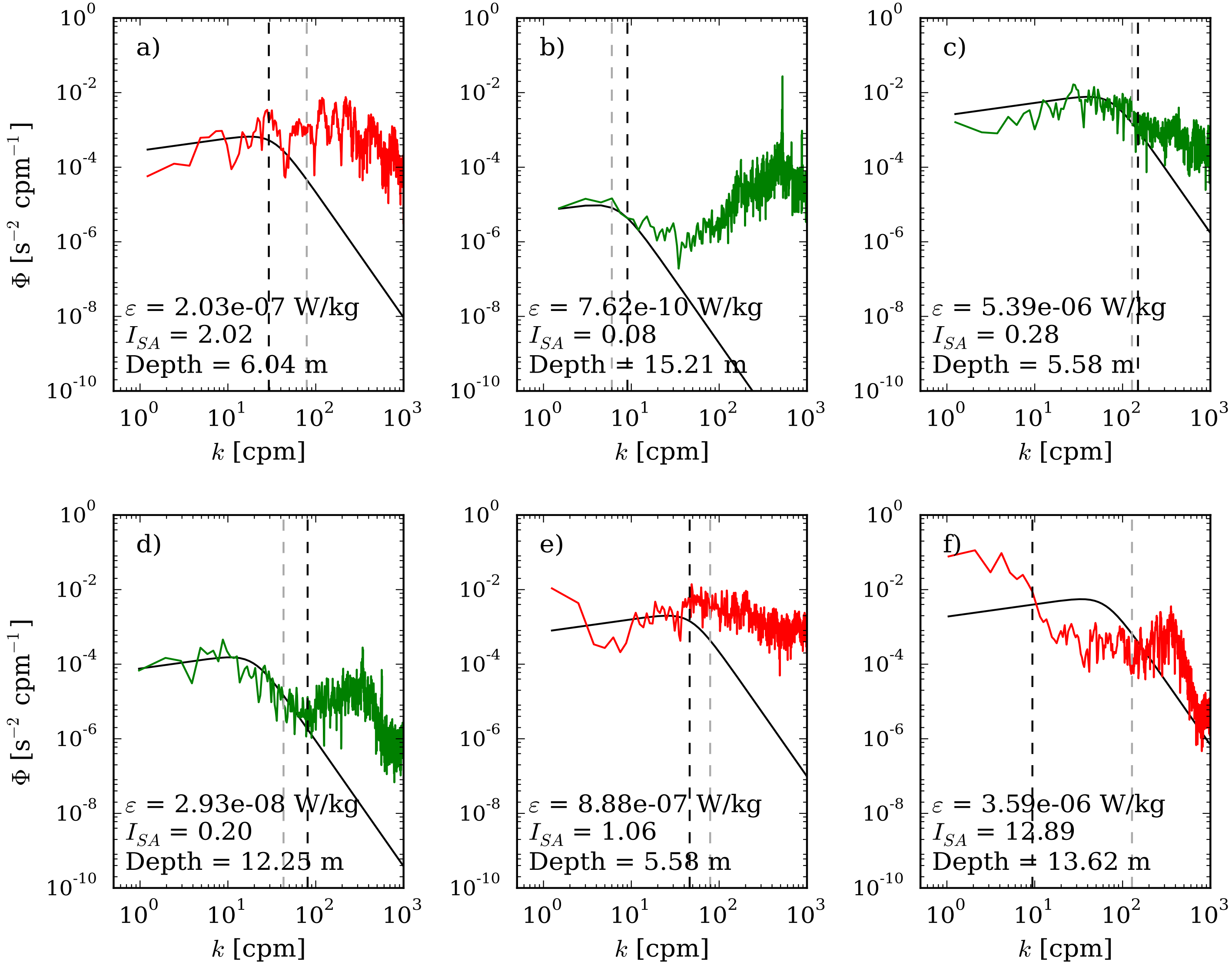

Figure 3.2: Shear spectra (red and green lines) and their corresponding empirical Nasmyth spectra (black line). The black and gray dashed lines correspond to k_{max} and k_{noise}, respectively. The yellow line shows the Kolmogorov scale. The color green stands for shear spectra that passed I_{SA}, whereas red indicates a bad agreement between the shear spectrum and the empirical spectrum identified by the index. The corresponding ε estimate, I_{SA} and depth are included in each plot.

Table 3.2: Total number of data points available for scientific analysis after data processing and percentage of rejected values (C14 and C15)

Campaign/ Glider	Profile	Total number of data points after processing	Total of data points rejected [%]	Percentage rejected due to $U_g \leqslant 20\, u_t$	Percentage rejected due to I_{SA}
C14					
Amadeus	upcasts	52,528	3.4	9.6	90.4
Amadeus	downcasts	83,520	6.3	52.3	46.0
C15					
Comet	upcasts	107,440	4.5	77.6	21.8
Comet	downcasts	76,339	1.4	50.1	45.9
Sebastian	upcasts	113,202	1.8	57.9	40.3
Sebastian	downcasts	77,018	0.9	39.7	54.4

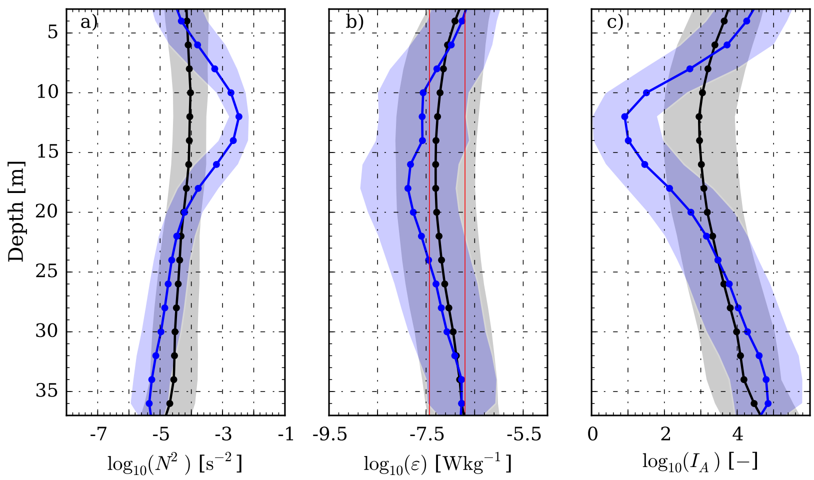

Figure 3.3: Vertical profiles of the decadic logarithm of the mean and one standard deviation of N^2 (a), ε (b) and I_A (c). The mean of the data at every two meters was determined for the complete stratified period of the campaign in 2014 (C14, blue data points) and during the complete research cruise in 2015 (C15, black data points). Shaded blue and black areas represent one standard deviation of the corresponding values during C14 and C15, respectively. In subplot (b), the red lines represent the lower and upper estimates of additional turbulence that could be supplied to the water column by the large-scale installation of offshore wind farm foundations in the North Sea.

3.4.4 Agreement between ε estimates from up- and downcasts and different gliders

The mean agreement between the estimates of ε obtained from up- and downcasts was a factor of 2.1 for Amadeus, 1.1 for Comet and 1.0 for Sebastian. In view of the good agreement between up- and downcast measurements from Amadeus during C14, these estimates were analyzed together in the generation of mean vertical profiles to enhance statistical significance (Figure 3.3). Differences in ε estimates observed between up- and

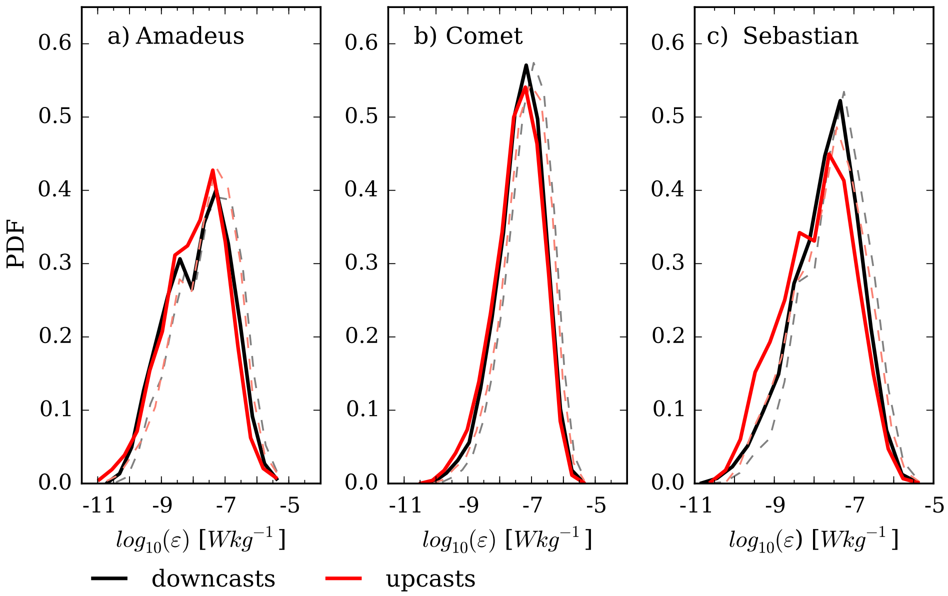

Figure 3.4: Probability density functions (PDFs) of the decadic logarithm of the dissipation of turbulent kinetic energy estimates from upcasts (red, solid lines) and downcasts (black, solid lines) after applying the Goodman algorithm (*Goodman et al.*, 2006). Red and black dashed lines correspond to the PDFs of the dissipation estimates without the use of the algorithm for up- and downcasts, respectively. (a) Amadeus; (b) Comet; (c) Sebastian.

downcasts of single gliders appear to be related to the flight behavior of the glider and the extent to which the method applied is able to describe it. For example, small errors in the measured pitch or in the angle of attack obtained by the hydrodynamic flight model could be responsible for the imperfect agreement between the casts.

During C15, inferences of dissipation of turbulent kinetic energy from Comet's and Sebastian's up- and downcasts agreed on average by a factor of 3.6 – 6.9. In C15, the datasets were collected in early spring by two different gliders that were approximately 15.4 (± 10) km apart, and consequently subjected to elevated spatial variability of turbulent events due to unsteady and patchy weak vertical stratification. Therefore, up- and downcast measurements from Comet and Sebastian are considered to be in very good agreement and were evaluated together when producing averaged profiles (Figure 3.3).

Figure 3.4 shows the probability distributions of ε inferred from shear measurements during up- and downcasts for all three gliders. Results are shown with and without the use of the Goodman algorithm (*Goodman et al.*, 2006), which is used to remove the influence of glider motions on the shear measurements. Estimates obtained after using the algorithm differed on average by a factor of 0.6 – 0.8 from the raw estimates. Even though there is a risk of underestimation of turbulence by the use of the Goodman algorithm (*Fer et al.*, 2014; *Palmer et al.*, 2015), a factor of two difference between the estimates is within the acceptable uncertainty range, as ε varies by many orders of magnitude.

In the following, the temporal and vertical variability of ε and related quantities are introduced and discussed. Descriptive statistics are used to present the data, whereby mean values of turbulent parameters (ε, K_ρ, I_A, N^2) were calculated after *Baker and Gibson* (1987) assuming a log-normal distribution. The interquartile range is defined as the range between the 25^{th} and the 75^{th} percentiles.

Table 3.3: Qualitative statistics of the ε estimates for the whole water column and the thermocline. Mean values have been calculated after *Baker and Gibson* (1987) assuming a log-normal distribution. The 25^{th} and the 75^{th} percentiles are given under 25th and 75th, respectively. All values are reported in $\mathrm{Wkg^{-1}}$.

	2014		2015
	Thermocline	Water column	Water column
minimum	2.7×10^{-11}	1.1×10^{-11}	1.5×10^{-11}
maximum	9.8×10^{-6}	9.9×10^{-6}	9.6×10^{-6}
mean	2.0×10^{-8}	6.3×10^{-8}	8.3×10^{-8}
median	5.5×10^{-9}	2.7×10^{-8}	4.7×10^{-8}
25th	1.7×10^{-9}	3.8×10^{-9}	1.1×10^{-8}
75th	3.0×10^{-8}	1.2×10^{-7}	1.5×10^{-7}

3.5 Results

3.5.1 Stratification and the dissipation of turbulent kinetic energy

In C14, the water column in the research area was strongly stratified, with a 5.0 ($\pm$ 2.2) m thick thermocline situated between 10.3 ($\pm$ 1.7) m and 15.2 ($\pm$ 1.5) m depth on average (plus or minus one standard deviation). The difference in temperature between surface and bottom mixed layers was approximately $\Delta T = 6$ °C, whereby the water temperature in these layers was around 20 – 21 °C and 14 – 15 °C, respectively, for all of the C14 data presented (Figure 3.5(a)). Here, the thermocline depth and thickness are calculated by first sorting each temperature profile to be monotonically decreasing with depth to circumvent temperature overturns. Subsequently, the temperature at the top and bottom of the main thermocline are defined as being $0.1\Delta T$ ($\sim$ 0.6 °C) warmer (bottom) or cooler (top) than mixed layer temperatures (Figure 3.5(a), thin black lines). Unless specified otherwise, we refer to this definition of the thermocline throughout the study. Note that, however, a second, much weaker, thermocline is observed with a temperature difference of $0.05\Delta T$ ($\sim$ 0.3 °C) between thermocline extremities and bottom mixed layers (Figure 3.5(a), red lines).

A tidal amplitude of approximately 0.4 $\mathrm{ms^{-1}}$ was recorded during C14. In the North Sea, semidiurnal tides are major contributors of variance in currents, which travel in a counterclockwise direction along the coasts and have the largest amplitudes along the eastern English and German coasts (*Huthnance*, 1991). The ε estimates reveal a clear tidal signal in the bottom mixed layer from tidally-driven bottom boundary layer turbulence (Figure 3.5(b)). The tidally-driven turbulence in the lower layer is damped by the stable stratification in the thermocline throughout the presented period, thus bottom boundary layer turbulence is not observed within the thermocline nor in the surface mixed layer. In the surface mixed layer, high values of ε are observed towards the water surface and are largely explained by wind forcing. Within the thermocline, turbulence is sporadic and ranges between 2.7×10^{-11} $\mathrm{Wkg^{-1}}$ and 9.8×10^{-6} $\mathrm{Wkg^{-1}}$, with a mean of 2.0×10^{-8} $\mathrm{Wkg^{-1}}$ (Figure 3.5(b), Table 4.1). Dissipation rates were the highest at the surface mixed layer and bottom boundary layer. The lowest dissipation levels occurred at the center of the thermocline and below it. Figure 3.6 depicts the vertical variability of the dissipation estimates and the squared buoyancy frequency with respect to the center

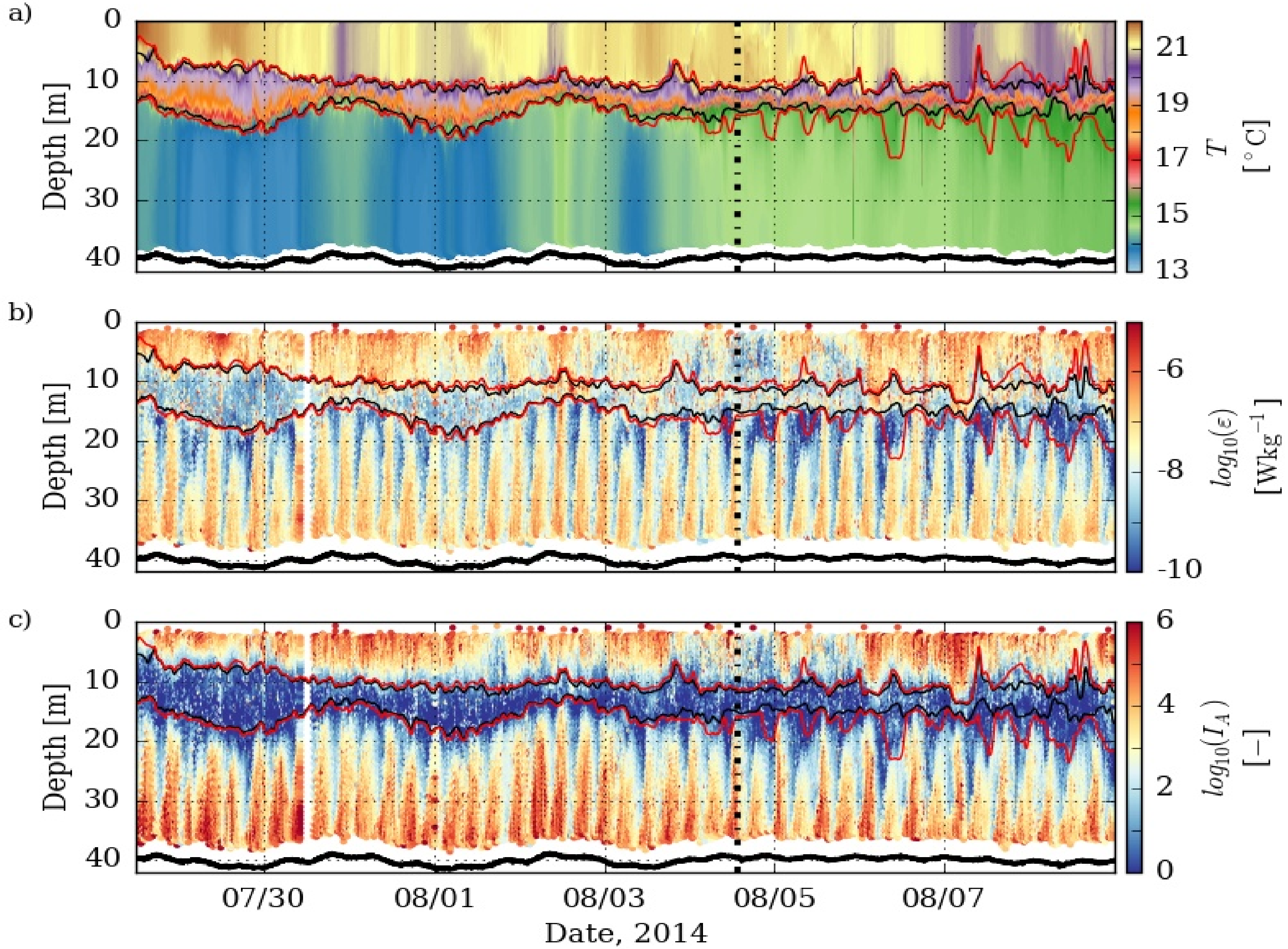

Figure 3.5: Time series of temperature (a), ε (b) and I_A (c) during C14. The main thermocline is shown in black together with a second, less sharp, thermocline (red line) for comparison. The thick black line in the bottom (around 40 m) delineates the seabed. The black dot-dashed lines show the start of the "spiral missions", in which the position of the tail rudder of the glider was fixed (more details in Sections 3.3 and 3.6.1). These scatter plots were produced using measurements and estimates derived from upcasts (Amadeus).

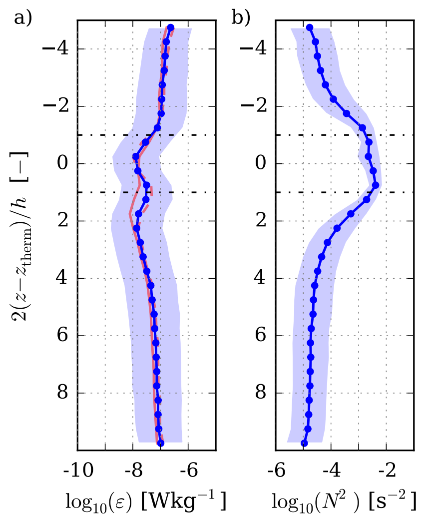

Figure 3.6: Vertical profiles of the decadic logarithm of the mean (blue) and one standard deviation (blue shade) of ε (a) and N^2 (b). The calculations refer to the complete stratified period of the campaign (C14), whereby the data was centred with respect to the non-dimensionalized main thermocline found between -1 and 1. In the y-axis, z_{therm} represents the center of the thermocline and h is the thermocline thickness. Time-averaged vertical profiles of up- and downcasts in C14 are depicted by the continuous and dashed red lines, respectively.

of the thermocline. Even though ε estimates were overall lower within the thermocline than in the mixed layers, they were relatively higher in the extremities of the thermocline than in its center (Figures 3.3 and 3.6).

In C15, the water column remained well-mixed for the majority of the time. The strong tidal signature can be clearly visualized in the dissipation estimates and, in the absence of significant vertical stratification, nearly reaches the top of the water column (Figure 3.7(b)). The highest ε values were observed near the sea surface and the seabed, whereas the lowest ε estimates were obtained during slack water periods at mid-water depths. Minimum and maximum ε were 1.5 x 10^{-11} and 9.6 x 10^{-6} Wkg^{-1}, and the mean was 8.3 x 10^{-8} Wkg^{-1} (Table 4.1). Both gliders captured the onset of stratification in the end phase of the campaign, approximately 3 days before the end of the research cruise. During these days, the temperature difference between surface and bottom mixed layers reached 1 °C. Moreover, in May 23 – 28, both gliders recorded data from an unsteady and weakly stratified area, in which the net temperature change between surface and bottom mixed layers was most often below 0.5 °C and occasionally as low as 0.2 °C. In this period, the weak stratification is observed to damp the tidally-driven bottom boundary layer turbulence, which is trapped below the temperature gradient (Figure 3.7(b)). Whilst the wind speed during this period remained below 10 ms^{-1}, on May 28, the wind speed reached 12.5 ms^{-1} and was able to effectively mix the weak stratification.

3.5.2 Turbulent activity index

The turbulent activity index, I_A, is used to quantify turbulent mixing under stratified conditions. The I_A can be obtained from the ratio of the Ozmidov scale (L_O) to the Kolmogorov scale $L_K = (\nu^3/\varepsilon)^{1/4}$, that is, the ratio of the largest possible turbulent

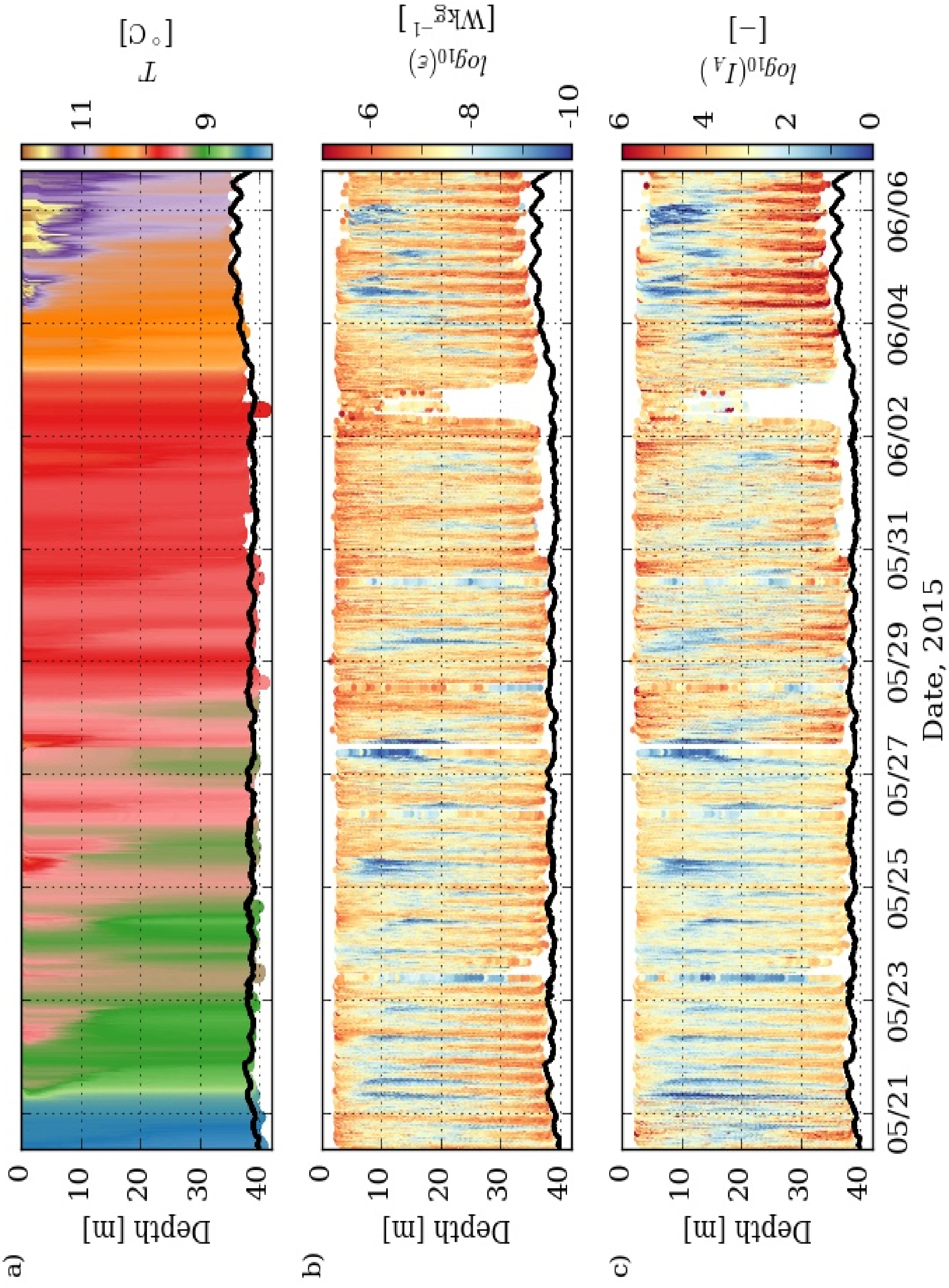

Figure 3.7: Time series of temperature (a), ε (b) and I_A (c) during C15. The thick black line in the bottom (around 40 m) delineates the seabed. These scatter plots were produced using measurements and estimates derived from upcasts (Comet).

eddies given the strength of the stratification ($N^2 = (g/\rho_o)d\rho/dz$, the buoyancy frequency squared) and the smallest viscous scales in turbulent flow, which depend only on ε and ν (*Hebert and de Bruyn Kops*, 2006),

$$I_A = \left(\frac{L_O}{L_K}\right)^{4/3} = \frac{\varepsilon}{\nu N^2}. \tag{19}$$

Figures 3.5(c) and 3.7 show the areas characterized by a high and low turbulent activity index. Experimental and numerical analysis suggest that fully turbulent isotropic mixing takes place when $I_A > O(10^2)$ (*Smyth and Moum*, 2000; *Shih et al.*, 2005). During C14 (C15), 69% (81%) of the I_A estimates were higher than the threshold value 100, indicating fully turbulent and isotropic mixing for the majority of the collected data points. However, within the thermocline the interquartile range of I_A was 0.6 – 7.2, and only 6% of the data points resulted in a I_A above 100, suggesting a regime shift within the thermocline. A total of 20% of the data points in the thermocline were found between $7 \leqslant I_A \leqslant 100$, the transitional regime, in which turbulence is able to actively mix stratification despite not being fully isotropic (*Stillinger et al.*, 1983; *Shih et al.*, 2005; *Bouffard and Boegman*, 2013).

A turbulent activity index lower than $7 - 20$ indicates quiescent flow, being therefore not sufficiently energetic to promote significant diapycnal mixing (*Stillinger et al.*, 1983; *Itsweire et al.*, 1986; *Ivey et al.*, 2008). Within the quiescent level, *Bouffard and Boegman* (2013) have suggested a differentiation between a molecular regime and a buoyancy-controlled regime by extending existing parameterizations based on a low Prandtl number Pr = 0.7 (*Shih et al.*, 2005) to higher Prandtl numbers up to 700. The Prandtl number denotes the ratio of momentum to the scalar diffusivities. By considering $0.7 \leqslant Pr \leqslant 700$, the corresponding value for the diffusion of heat in seawater $\mathrm{Pr}_{\mathrm{sw}} \approx 7$ (at 20 $^\circ C$) is included. In the molecular regime $I_A < 10^{2/3}Pr^{-1/2}$ ($I_A < 1.7$ at $\mathrm{Pr}_{\mathrm{sw}}$), turbulence is expected to be completely suppressed by stratification, resulting in laminar flow. In the buoyancy-controlled regime $10^{2/3}Pr^{-1/2} \leqslant I_A \leqslant (3\ln\sqrt{Pr})^2$ ($1.7 < I_A < 8.5$ at $\mathrm{Pr}_{\mathrm{sw}}$), turbulent mixing takes place, albeit at much lower rates than in the intermediate regime. Within the thermocline (C14), approximately 77% of the I_A estimates were below 8.5, of which 67% were lower than 1.7. Therefore, in contrast to the bottom and surface mixed layers, the thermocline is characterized by quiescent to transitional flow.

Figure 3.8 depicts three different levels of I_A in the thermocline, defined by *Shih et al.* (2005): (1) quiescent or laminar (blue dots, $I_A < 7$), (2) intermediate between quiescent and turbulent flow (yellow dots, $7 \leqslant I_A \leqslant 100$) and (3) fully turbulent flow (red dots, $I_A > 100$). The extremities of the thermocline are dominated by quiescent flow, which occasionally develops into turbulence.

3.5.3 Turbulent diffusivity in the thermocline

Within the thermocline, the intensity of diapycnal mixing generated by the observed values of dissipation of turbulent kinetic energy is estimated by using the Osborn relation for every ε estimate:

$$K_\rho = \Gamma\frac{\varepsilon}{N^2}, \tag{20}$$

where Γ is the so called "mixing efficiency". Γ has been frequently set to 0.2 for shear-generated mixing (*Thorpe*, 2007; *Osborn*, 1980), although more recent studies reporting

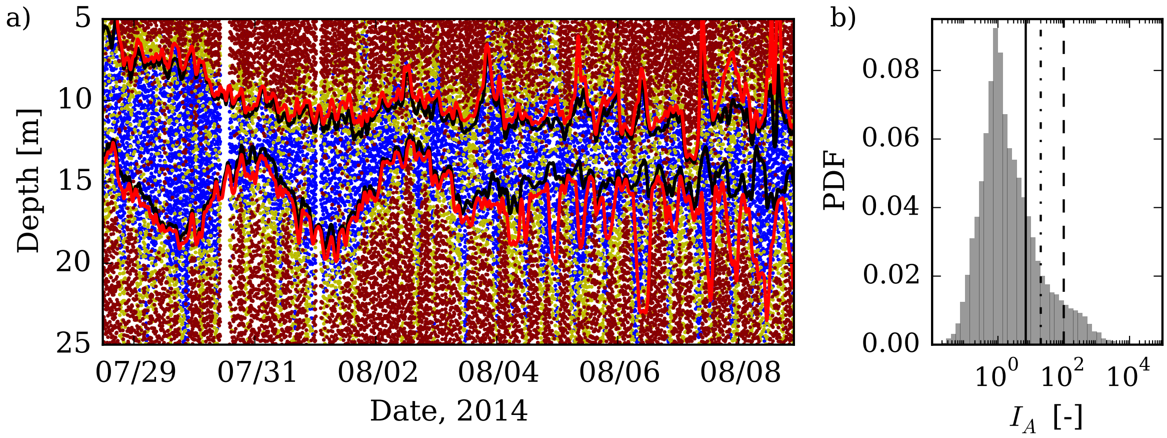

Figure 3.8: (a) Turbulent activity index at the thermocline (C14). Red dots represent $I_A > 100$, yellow dots stand for $7 \leqslant I_A \leqslant 100$ and blue dots symbolize $I_A < 7$. The black and red lines delineate the main and secondary thermoclines, respectively. (b) Histogram of I_A in the main thermocline. The solid line indicates $I_A = 7$, the dot-dashed line holds the $I_A = 20$ mark, and the dashed line shows $I_A = 100$.

on direct numerical simulations (*Shih et al.*, 2005) and oceanic field measurements (*Walter et al.*, 2014) define $\Gamma = f(I_A)$.

Parameterizations of variable mixing efficiency commonly set $\Gamma = 0.2$ for the intermediate regime defined in subsection 3.5.2, and $\Gamma = 2N(\nu/\varepsilon)^{1/2}$ for the fully turbulent regime, with the mixing efficiency approaching zero as I_A increases (*Shih et al.*, 2005; *Ivey et al.*, 2008; *Bouffard and Boegman*, 2013). For the buoyancy-controlled regime, the mixing efficiency is calculated as $\Gamma = 0.1\varepsilon^{1/2}/(Pr^{1/4}\nu^{1/2}N)$ and, in the molecular regime ($I_A < 1.7$), K_ρ is set to 1.4 x 10^{-7} m^{2}s^{-1} (*Bouffard and Boegman*, 2013), which corresponds to the molecular diffusion coefficient of heat in seawater (κ_T).

In the following we present results from both parameterizations, of which differences will be shown in subsection 3.6.1 to significantly affect the rate of vertical scalar flux, and therefore the heat budget. The estimated turbulent diffusivity levels spanned over several orders of magnitude within the thermocline, namely over 10^{-7} – 10^{-4} m^{2}s^{-1} for $\Gamma = f(I_A)$ and over 10^{-7} – 10^{-2} m^{2}s^{-1} for a constant mixing efficiency. Turbulent mixing was in general relatively low, with the interquartile range of the turbulent diffusion rate between 1.4 x 10^{-7} m^{2}s^{-1} and 2.0 x 10^{-6} m^{2}s^{-1} for both parameterizations. In this region of the water column, K_ρ was often close to the molecular diffusion coefficient of heat in seawater, which was expected as a considerable portion of the thermocline is dominated by the laminar regime (cf. subsection 3.5.2). Higher mixing rates on the order of $O(10^{-5})$ – $O(10^{-4})$ m^{2}s^{-1} were found in the upper half of the thermocline and, during ebb and flood periods, in the bottom of the thermocline where it encounters the bottom mixed layer. The turbulent mixing rates obtained in this study are in reasonable agreement with other studies (*Rippeth*, 2005; *Ledwell et al.*, 2004; *Palmer et al.*, 2015; *van Haren et al.*, 1999; *Burchard and Rippeth*, 2009) and are discussed in the following section by means of the calculation of the heat budget.

3.6 Discussion

On both campaigns, high dissipation levels were observed close to the water surface and near the seabed, which is explained by enhanced turbulence caused by wind and bottom friction of the tidal currents, respectively. Dissipation estimates obtained during slack water at midwater depths were about two orders of magnitude lower than during periods of tidal motion. The tidal signature in ε extended upwards until the thermocline in the stratified dataset (C14), and until a height of 25 − 30 m in the well-mixed areas in C15. These observations are in good agreement with *Simpson et al.* (1996), who conducted measurements in 1993 in the Irish Sea over a few tidal periods, and with *Palmer et al.* (2008), who reported on measurements taken in 2003 in the Celtic Sea. Within the thermocline, turbulence varied over several orders of magnitude, underlining the difficulty in estimating a mean value for the dissipation of turbulent kinetic energy.

Further, it was observed in C15 that a temperature difference of 0.2 °C is able to damp boundary-generated ε, decreasing the turbulent activity to transient and quiescent levels, and therefore supressing vertical fluxes for the given time period (Figure 3.7). Measurements obtained from both gliders during C15 revealed that in early spring, before a steady thermocline is established, turbulence and stratification properties in the studied region are highly variable.

3.6.1 Stratification and transport through the thermocline

To investigate the role of the thermocline in limiting transport between layers, we use glider measurements taken during the "spiral missions" introduced in section 3.3, in which the glider moves in an approximately Lagrangian fashion and is therefore expected to remain in the same body of water. The spiral missions were conducted close to the bottom-mounted ADCP and took place under light wind conditions, on average 5.2 (± 2.2) ms^{-1}. Therefore, given that the geographical variation of the glider during the spiral missions was low (8.3 km), horizontal advection of heat is expected to play a minor role and is neglected. Furthermore, the average temperature within the water column in this period was conserved at 17 (± 0.2) °C, which further suggests that solar heating and heat absorption through the seabed can be neglected, enabling the calculation of the heat budget.

Heat budget

The estimates of dissipation of turbulent kinetic energy obtained during the spiral missions are shown in Figure 3.9. The mean vertical heat flux $\langle Q_T \rangle$ (Wm^{-2}) is estimated for each profile using the heat capacity of sea water $c_p = 3993$ Jkg^{-1}K^{-1} at 20 °C, the mean of the depth derivative of temperature within the thermocline limits $\langle \partial T/\partial z \rangle$ and the depth averaged thermocline turbulent diffusivity K_{thm}:

$$\langle Q_T \rangle = \rho_0 c_p K_{\mathrm{thm}} \left\langle \frac{\partial T}{\partial z} \right\rangle, \tag{21}$$

where K_{thm} is calculated as

$$K_{thm} = \frac{1}{h} \int_{h_{\mathrm{top}}}^{h_{\mathrm{bot}}} K_\rho \, \mathrm{d}z, \tag{22}$$

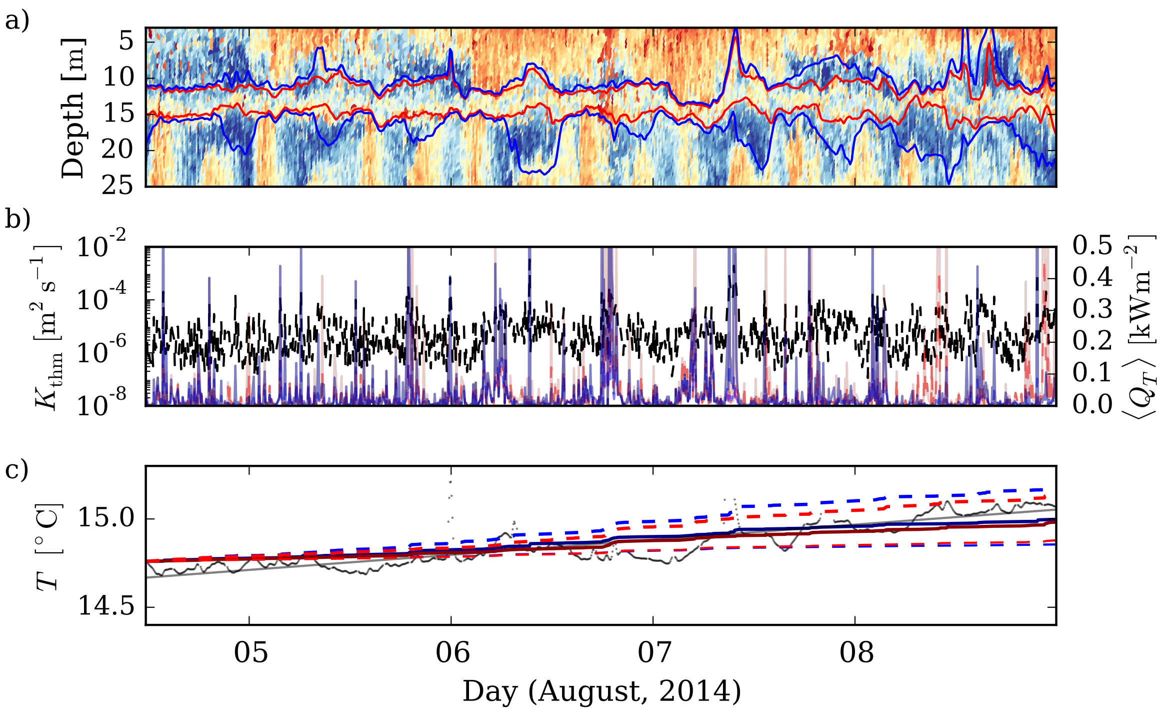

Figure 3.9: (a) ε estimates during the spiral missions conducted in the C14 campaign. The thin lines around 10 m and 15 m indicate the position of the thermocline, where blue and red lines stand for the thermocline definitions i) and ii), respectively. This scatter plot was produced using measurements from upcasts (Amadeus). (b) Average turbulent diffusivity ($\Gamma = 0.2$) within the main thermocline (black dashed line). The continuous lines show the vertical heat flux calculated with $\Gamma = 0.2$, whereby the blue line shows results for the thermocline definition i) and, conversely, the red line shows results from definition ii). (c) Measured evolution of bottom mixed layer temperature with time (black dots). The black line corresponds to a linear regression of the measured data points. The parameterized increase in bottom mixed layer temperature is depicted by continuous lines (constant Γ), thin dashed lines (variable Γ), and thick dashed lines (ε calculated without the Goodman algorithm, with constant Γ). The line colors have the same meaning as described in (a). This analysis was conducted using measurements taken during the spiral missions (August 4 – 9) in C14.

in which h_{top} and h_{bot} stand for the thermocline limits, and h is the thermocline thickness. In equation (21), it is observed that the K_{thm} factor largely determines the outcome of the heat flux as, in contrast to $\langle \partial T/\partial z \rangle$, it varies over several orders of magnitude.

There is no universal definition of the thermocline, which is a source of uncertainty when estimating the heat budget. To account for this uncertainty, we calculate the heat budget based on the two different definitions of the thermocline given in section 3.5. Moreover, the bottom and top of the thermocline are marked either by i) $0.1\Delta T$ °C, or ii) $0.05\Delta T$ °C lower (higher) temperatures than in the top (bottom) mixed layers. Depending on the definition of the thermocline and the Γ parameterization used, the average vertical heat flux driven by diapycnal turbulent diffusion between August 4 – 9 was 18.4 – 49.5 Wm^{-2} (Table 3.4). The depth averaged thermocline turbulent diffusivity K_{thm} and the vertical heat flux are depicted in Figure 3.9(b). During this period, the temperature in the bottom mixed layer increased by 0.4 °C, which corresponds to a

Table 3.4: Overview of the heat budget performed during the spiral missions in C14. The space and time averages of the heat flux $\langle Q_T \rangle$ across the thermocline and of the rate of change in bottom mixed layer temperature $\mathrm{d}T/\mathrm{d}t$ are listed for the studied cases. Similarly, the percentage of the heat budget that can be explained through the estimated thermocline turbulent diffusivity K_{thm} is reported. In the description of the cases, the letter "G" denotes the use of the Goodman algorithm in the calculation of the ε. The range shows the variation among different thermocline definitions.

Case	$\langle Q_T \rangle$ [$\mathrm{Wm^{-2}}$]	$\mathrm{d}T/\mathrm{d}t$ [$^\circ\mathrm{Cs^{-1}}$]	Percentage explained through K_{thm} [%]
ε, $\Gamma = 0.2$, G	44.8 – 49.5	6.1 – 6.8 x 10^{-7}	64.3 – 73.5
ε, $\Gamma = 0.2$	79.8 – 84.3	1.0 – 1.2 x 10^{-6}	111.1 – 126.7
ε, $\Gamma = f(I_A)$, G	18.4 – 25.7	2.8 – 3.2 x 10^{-7}	29.6 – 34.2
ε, $\Gamma = f(I_A)$	29.3 – 41.4	4.4 – 5.3 x 10^{-7}	47.0 – 55.6

warming rate of 1 x 10^{-6} $^\circ\mathrm{Cs^{-1}}$. The predicted effect of $\langle Q_T \rangle$ on the bottom mixed layer temperature was calculated as

$$\frac{\mathrm{d}T}{\mathrm{d}t} = \frac{\langle Q_T \rangle}{c_p \rho_o H_{\mathrm{BML}}}, \tag{23}$$

where $\mathrm{d}T/\mathrm{d}t$ is the rate of change of temperature [$^\circ\mathrm{Cs^{-1}}$], and H_{BML} [m] is the height of the bottom mixed layer (BML). The measured increase in BML temperature based on definition i) is depicted in Figure 3.9(c), alongside with the estimated change in BML temperature due to diapycnal diffusion (equation (21)). Depending on the two definitions of the thermocline described above, and on the definition of the mixing efficiency, the parameterized vertical heating rate was on average 2.8 x 10^{-7} – 6.8 x 10^{-7} $^\circ\mathrm{Cs^{-1}}$ (Table 3.4). Moreover, 30 – 74% of the observed increase in bottom mixed layer temperature could be traced back to diapycnal mixing generated from turbulence within the thermocline (Table 3.4). A steady-state heat budget estimate, in which K_{thm} and dT/dz were set constant from the average over the spiral missions, shows that 14 – 62% of the increase in bottom mixed layer temperature can be attributed to above average thermocline turbulent diffusivities. Approximately 26 – 69% of the parameterized increase in temperature can be traced back to high heat flux rates ($\langle Q_T \rangle \geqslant 80$ [$\mathrm{Wm^{-2}}$]), suggesting that much of the heating of the bottom mixed layer is triggered by sporadic events of high turbulent diffusivity (Figure 3.9). This also highlights the need for long uninterrupted time series to accurately capture turbulent fluxes.

Considerations

Possible errors in the calculation of ε, and therefore of K_{thm}, may explain the difference between measured and calculated flux rates (*Palmer et al.*, 2008; *Simpson et al.*, 1996) as ε estimates are uncertain within at least a factor of two. Estimates of the dissipation of turbulent kinetic energy from gliders have relied until recently on instrument velocities calculated either through the hydrodynamic flight model introduced in section 3.4, or through the vertical velocity, the pitch angle and the angle of attack. As shown in

Figure 3.6(a), the agreement between up- and downcasts in the time-averaged vertical profiles is largely within a factor of two, with the exception of the bottom of the thermocline. In the bottom of the thermocline, the time-averages of up- and downcasts agree by a factor of 2.6 – 4.4. Further research on the glider flight is needed to advance current understanding of its behavior when entering and leaving sharp thermoclines, and therefore reducing the uncertainties when calculating ε. The addition of recently developed velocitimeters for microstructure packages might help to improve current understanding of the glider flight. Another source of uncertainty is the use of the Goodman algorithm in the calculation of ε, which might not be appropriate when using gliders (*Fer et al.*, 2014; *Palmer et al.*, 2015). If K_ρ is estimated using ε without the Goodman algorithm, the increase in BML temperature can be traced back to vertical mixing is a factor of 0.5 – 1.3 of the measured temperature change (Table 3.4).

Further, the choice of applying a constant mixing efficiency $\Gamma = 0.2$ instead of $\Gamma = f(I_A)$ in the calculation of K_ρ has a significant effect in closing the heat budget. The parameterization based on a constant mixing efficiency significantly improves the recovery of the heat budget compared to a mixing efficiency that varies with the turbulence activity index (Figure 3.9(b)). These results suggest that the experimentally defined constant mixing efficiency might still be more accurate than the parameterization relating the mixing efficiency with the turbulent activity index, as already suggested by *Gregg et al.* (2012); *Cyr et al.* (2015). Overall, these results underline the importance of diapycnal mixing for heat transfer into deeper layers of the water column and are in good agreement with previous studies (*Palmer et al.*, 2008, 2015). In addition, we provide evidence of the sensitivity of the heat budget to various assumptions, such as thermocline limits, mixing efficiency and ε, which may measurably impact the outcome and should be considered.

3.6.2 Bulk Richardson number and the influence of shear in scalar transport

To assess the role of shear in overcoming stratification to produce the observed dissipation rates and turbulent diffusivities, the bulk Richardson number (Ri_b) is defined for the thermocline region throughout C14 as

$$Ri_b \equiv \frac{g\Delta\rho h}{\rho_o(\Delta u)^2}\,, \tag{24}$$

where Δu and $\Delta\rho$ represent the change in current velocity and the change in density between the top and the bottom of the thermocline. Velocities in the upper and lower layers are calculated using the ADCP data by averaging within bins located between $1-5$ m above and below the top and bottom of the thermocline, respectively. These bins were found to be representative of across-thermocline shears, and do not include significant effects of the deviation of the current within the bottom boundary layer. Ri_b describes the stability of the thermocline in bulk, in which one estimate is obtained every 10 minutes.

If the thermocline and the shear layer have the same thickness and are centred with respect to each other, then $Ri_b < 1/4$ is a *necessary* condition for instability in stratified shear layers to develop (*Smyth et al.*, 2007; *Hazel*, 1972). The resulting instabilities would be of the Kelvin-Helmholtz type causing an overturning of the density interface into the characteristic billow structure. In C14, the thermocline was dominated by stable stratification and weak shear. Figure 3.10 shows Ri_b for C14, which stayed well above the critical value 1/4 during nearly the entire studied period. Of the estimated Ri_b values,

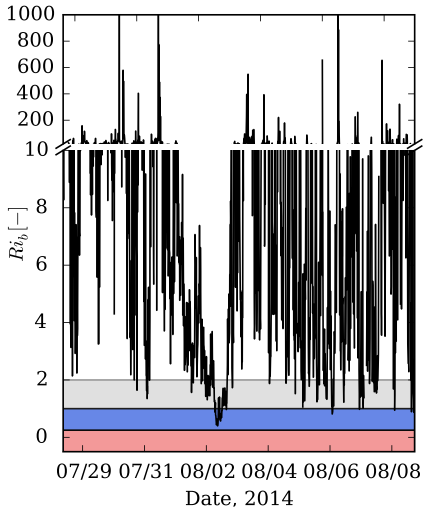

Figure 3.10: Bulk Richardson number during the C14 campaign. The gray shaded area underlines $1 \leqslant Ri_b \leqslant 2$ and the blue shaded area displays $0.25 \leqslant Ri_b \leqslant 1$. The red shaded area marks the $Ri_b \leqslant 0.25$ threshold, which is a necessary condition for turbulence to overcome stratification.

2% were less than or equal to 1 and 11% were less than or equal to 2. In periods where shear and stratification are roughly the same order of magnitude ($0.25 \leqslant Ri_b < 2$), the thermocline is often thought to be marginally stable and shear instabilities are potentially able to drive turbulent mixing (*Rippeth et al.*, 2005; *Rippeth*, 2005). This demonstrates however that the thermocline was stable to Kelvin-Helmholtz instabilities according to linear stability analysis, which is unsurprising given the absence of large-scale overturns of the thermocline.

van Haren et al. (1999); *Rippeth* (2005); *Palmer et al.* (2008) have hypothesized that the thermocline in European shelf seas can often be classified as marginally stable. This is based on the calculation of the gradient Richardson number, $Ri_g(z) = N^2/S^2$, where $S(z)$ denotes a measured vertical profile of shear, and instability becomes possible when $Ri_g(z) < 1/4$ somewhere in the water column. Whilst Ri_g might be able to capture localized instabilities in the water column invisible to the bulk value, Ri_b, its calculation requires high frequency (± 1 Hz) ADCP measurements, which are not available for our dataset. Moreover, high frequency ADCP measurements are necessary to meaningfully filter out the noise generated by the instrument itself without artificially thickening the shear layer and therefore decreasing Ri_g. In our analysis, subcritical values of the bulk Richardson number ($Ri_b < 1/4$) were not observed, indicating that the thermocline is stable to a large-scale overturn triggered by Kelvin-Helmholtz instability (Figure 3.10). However, the possibility remains that localised instabilities of shorter time scales are present on the edges of, or within, the thermocline.

Similar to other studies (*van der Lee and Umlauf*, 2011; *Cyr et al.*, 2015; *Palmer et al.*, 2008), we follow the procedure described in *MacKinnon and Gregg* (2003) to evaluate the relationship between shear, stratification and the dissipation of turbulent kinetic energy. Since our calculations are based on bulk values, ε is averaged across the thermocline and sorted in bins of bulk shear squared $S^2 \sim S_{\mathrm{h}}^2 = \Delta U^2/h^2$ and bulk buoyancy frequency squared $N^2 \sim N_{\mathrm{h}}^2 = g\Delta\rho/\rho_o h$. Further, we compare the parameterization of *MacKinnon and Gregg* (2003), $\varepsilon_{\mathrm{MG}} = \varepsilon_0(N/N_0)(S/S_0)$, with $S_0 = N_0 = 3$ cph and

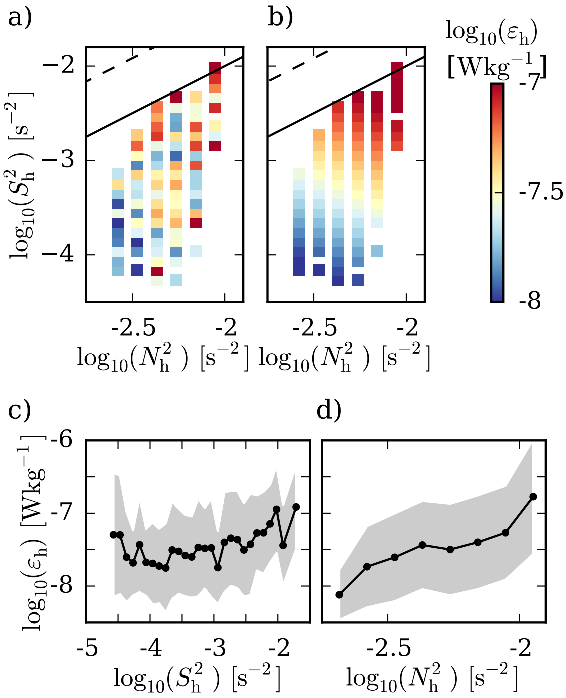

Figure 3.11: Calculated (a) and parameterized (b) dissipation of turbulent kinetic energy as a function of bulk thermocline stratification and shear. The black solid and dashed lines represent $Ri_b = 1$ and $Ri_b = 0.25$, respectively. Relationship between ε_h and bulk thermocline shear squared (c) and buoyancy frequency squared (d). The gray shadows in (c) and (d) represent one standard deviation from the mean.

$\varepsilon_0 = 5.5$ x 10^{-10} Wkg^{-1}, to our observations. Here, ε_0 was chosen to match the average of the parameterization (Figure 3.11(b)) with the observed mean value. Our results do not show a conclusive agreement with the parameterization (Figure 3.11(a) and (b)). Figure 3.11(a) depicts the mean dissipation values for each bin of bulk shear and stratification $\varepsilon_h(N_h^2, S_h^2)$, which does not present a clear dependency on the bulk Richardson number. This seems reasonable considering that Ri_b remained stable throughout the campaign, whilst turbulence within the thermocline varied over several orders of magnitude. However, a tendency for low bulk Richardson numbers ($Ri_b \sim 1$) to be related to higher ε_h was found (Figure 3.11(a)).

A positive dependency is found between ε_h and N_h^2 and between ε_h and S_h^2 across the thermocline, with higher dissipation levels in strongly stratified and sheared areas (Figures 3.11(c) and (d)). Finally, if shear instabilities are responsible for triggering thermocline mixing, these results show that relatively small-scale sheared regions ($<$ 1m) must be resolved in order to assess thermocline stability.

3.6.3 Alterations in turbulence by offshore wind farms

The technological development of offshore wind turbines has led to the planning and construction of offshore wind farms in areas of the North Sea that can exhibit stratification during the summer months. The installation of wind turbines in a region strongly influenced by tidal currents generate a turbulent wake. Assuming that the North Sea would be entirely covered by equally spaced (700 – 800 m) wind turbines, *Carpenter et al.* (2016)

parameterized and tabulated turbulent production values for the German Bight sector of the North Sea based on standard bulk drag models. Depending on expected variations in the drag coefficient and on the foundation structure geometries, the average power production by turbine foundations that could be fed in to turbulence was estimated to be $\mathcal{P} = 4.6\text{x}10^{-8} - 2.5\text{x}10^{-7}\text{Wkg}^{-1}$ (*Carpenter et al.*, 2016). These values should be considered as order of magnitude estimates and are assumed to be constant with depth.

The strength of dissipation of turbulent kinetic energy generated by turbine foundations, ε_{OWF}, can be obtained through the approximate conservation equation of the turbulent kinetic energy ($\mathcal{P}+\mathcal{B}-\varepsilon = 0$), where $\mathcal{B} = -\Gamma\varepsilon$ is the buoyancy flux. For simplicity, we set $\Gamma = 0.2$, and obtain the relation $\varepsilon_{\text{OWF}} \approx 0.8\mathcal{P}$. This simple equation suggests that the possible strength of the dissipation of turbulent kinetic energy generated by wind turbine foundations would be as high as $3.7\text{x}10^{-8}$ – $2.0\text{x}10^{-7}$ Wkg^{-1} (Figure 3.3(a)).

Figure 3.3 shows that, on average, the turbulence generated by OWF foundations is expected to be in the same order of magnitude or weaker than bottom boundary layer turbulence, as already discussed by *Carpenter et al.* (2016). However, the addition of ε_{OWF} to the turbulent kinetic energy being dissipated in a natural stratified environment could enhance thermocline mixing significantly, as ε_{OWF} is estimated to be comparable to mean ε levels found in the thermocline. An increase in dissipation to this extent could locally drive the seasonal thermocline from a dominantly quiescent state to a highly turbulent state, enhancing mixing within stratification in the vicinity of the wind turbines. The response of the thermocline to anthropogenically induced enhanced levels of turbulent kinetic energy is however beyond the scope of this study and will be a topic of further study.

3.7 Conclusion

The present paper reports on extensive datasets for shallow shelf sea turbulence, allowing for the analysis of turbulence under stratified to well-mixed conditions over dozens of tidal cycles. We provided a direct comparison of the measured and estimated physical parameters between both regimes, enabling a better understanding of the processes governing scalar transport under stratified conditions. In recent years, the development of autonomous measurement platforms facilitates the execution of high quality and resolution experiments with a longer duration. The present study described observations from two different campaigns using underwater gliders equipped with microstructure sensors, which enabled the estimation of the dissipation of turbulent kinetic energy, turbulent diffusivity and turbulent activity index, in addition to the commonly measured CTD parameters. A bottom-mounted acoustic doppler current profiler allowed the calculation of the bulk Richardson number, which was compared against turbulence levels.

We provide evidence of the intermittency of turbulence (Figures 3.5(b), 3.7(b) and 3.9), which can be triggered by various processes that occur sporadically and can be captured through long-term measurements with more confidence. For example, approximately 50% of the increase in bottom mixed layer temperature during the spiral missions was caused by four major events, whereas slow, background heat transfer dominated the fluxes otherwise. We therefore stress the importance of long-term measurements to adequately assess the dissipation of turbulent kinetic energy and related parameters (e.g. turbulent activity index and turbulent diffusivity) in the water column, and suggest glider-based platforms as a step forwards.

While diffusion at molecular levels is abundantly present in the thermocline, turbulent mixing also takes place and contributes to vertical heat transport. Our results suggest that, on average, vertical mixing is the main mechanism driving scalar flux through the thermocline. A positive trend between bulk dissipation of turbulent kinetic energy, shear and stratification was found. Further enhanced levels of dissipation, turbulent activity index and turbulent diffusivity, which were continuously observed within the thermocline, might have been created by short-lived instabilities that are not resolved by the bulk Richardson number and by the ADCP. Future work could therefore focus on two different branches: 1. reducing the uncertainties linked with the estimation of ε, e.g. the verification of glider velocity; and 2. focussing on the study of small-scale shear (< 1 m) to improve the understanding of turbulence generation across stably stratified thermoclines and to improve large-scale model parameterizations. As for shallow shelf seas strongly influenced by tidal motion, the impact of the additional turbulence generated by offshore wind farms should be further investigated, as the additional forcing being supplied to the water column and, more specifically, to the thermocline by turbine foundations could locally drive turbulence to levels significantly above those observed in a natural environment. This enhanced mixing could lead to higher scalar fluxes across stratification, possibly affecting its stability and leading to the erosion of the thermocline in the vicinity of the turbine foundations, which could have further reaching implications on biological productivity.

3.8 Supplemental Information

Definition of the turbulent velocity scale

A characteristic velocity of the turbulent flow is defined through dimensional analysis:

$$u_t \equiv (\varepsilon l_t)^{1/3}, \tag{25}$$

where l_t is the turbulent length scale. The turbulent velocity scale, u_t, should be significantly lower than U for Taylor's hypothesis to hold (*Fer et al.*, 2014). In turbulence regimes controlled by stratification, defined here as $N^2 > 10^{-5}$ s^{-2}, the Ozmidov length scale $L_O = (\varepsilon/N^3)^{1/2}$ characterizes the maximum possible length of a turbulent eddy, whereby $N^2 = (g/\rho_o)d\rho/dz$ represents the buoyancy frequency squared (e.g. *Smyth et al.*, 2001). Additionally, to determine l_t for weakly-stratified to well-mixed regimes, the Corrsin scale $L_C = (\varepsilon/S^3)^{1/2}$ is calculated, in which S represents a typical vertical profile of shear in the measurement region. The Corrsin scale determines the maximum length scale of an eddy in regimes dominated by shear (*Smyth and Moum*, 2000; *Corrsin*, 1958). Boundary effects in the water column also limit the size of turbulent eddies and are accounted for by estimating a third, geometric, length scale $L_G = \kappa z(1 - z/H_{\mathrm{tot}})$ (*Simpson and Sharples*, 2012). In this equation, z is the height above bottom, H_{tot} is the water depth and $\kappa = 0.41$ is the von Kármán constant. The maximum turbulent length scale used to test for Taylor's hypothesis is ultimately estimated by taking $l_t = \min(\mathrm{L_O}, \mathrm{L_G})$ for regions of the water column dominated by stratification and $l_t = \min(\mathrm{L_C}, \mathrm{L_G})$ for weakly stratified to well-mixed areas:

$$l_t = \begin{cases} \min(\mathrm{L_O}, \mathrm{L_G}), & \text{if } N^2 > 10^{-5}\ s^{-2} \\ \min(\mathrm{L_C}, \mathrm{L_G}), & \text{if } N^2 \leqslant 10^{-5}\ s^{-2} \end{cases} \tag{26}$$

Acknowledgments

The authors would like to thank the Helmholtz Foundation, which provided funding through the Polar Regions and Coasts in the Changing Earth System II program (PACES II). We also gratefully acknowledge the support of R. Kopetzky, M. Heineke, B. Peters, J. Horstmann, the captain and the crew of the research vessel (RV) Ludwig Prandtl and the RV Heincke in the collection of the glider data. The RV Heincke ship time was provided through the grant AWI_HE445_00. We thank the Bundesamt fuer Seeschifffahrt und Hydrographie (BSH) for the deployment and recovery of the ADCP in 2014. We would also like to thank both reviewers for their insightful comments on the paper. The glider data used are listed in the COSYNA repository at http://codm.hzg.de/codm/. The processed shear microstructure and the ADCP data are made available in the Supplement. Raw microstructure and ADCP data are available upon request.

4 Storm-induced turbulence alters shelf sea vertical fluxes

This chapter is a reprint of the manuscript "Storm-induced turbulence alters shelf sea vertical fluxes" that has been submitted for publication.

Citation: Schultze, L. K. P., Merckelbach, L. M., & Carpenter, J. R. (2018). Storm-induced turbulence alters shelf sea vertical fluxes. Submitted for publication.

Keypoints

- Turbulent mixing in the thermocline increases significantly during storms
- Rapid storm-driven mixing is linked to marginal stability conditions in the thermocline
- Vertical fluxes during storms are estimated to account for a significant fraction of the summer budget

4.1 Abstract

Storms are infrequent, intense, physical forcing events that represent a potentially significant driver of ocean ecosystems. These abrupt physical and ecosystem changes are initiated by elevated levels of storm-driven ocean turbulence, yet despite the crucial role played by turbulence, there is a paucity of observations due to measurement difficulties during such extreme conditions. This difficulty has been overcome through the use of an autonomous underwater glider as it measured the turbulent ocean response to Storm Bertha, when it passed over the North Sea in August 2014. The storm was found to act as a trigger for the rapid mixing of the thermocline through shear instability, increasing vertical fluxes nearly an order of magnitude, and promoting increases in surface layer chlorophyll. The results demonstrate that storms represent a significant fraction of seasonal fluxes, with important consequences for biological production in shelf seas.

4.2 Introduction

Storm Bertha grew to hurricane status as it reached maximum intensity on 4 August 2014 over the Atlantic Ocean north of the Caribbean Islands. After quickly downgrading to an extratropical storm, it moved offshore along the eastern coast of the US and Canada, eventually crossing the North Atlantic, passing over the UK and the North Sea (Figure 4.1A), before ultimately dissipating over Scandinavia around 15 August. Coincident with its passage across the North Sea, an ocean glider was fortuitously deployed in the storm path (Figure 4.1B). Ocean gliders are autonomous underwater vehicles that adjust their buoyancy to vertically profile the water column, while using lift from the hull and wings to glide horizontally through the water like conventional glider aircraft (*Davis et al.*, 2002; *Rudnick*, 2016). Equipped with microstructure sensors, the ocean glider was capable of measuring the small and rapidly fluctuating turbulent current shears required in the direct quantification of the dissipation rate of turbulent kinetic energy (*Fer et al.*, 2014; *Palmer et al.*, 2015; *Schultze et al.*, 2017). In this letter we show that the storm causes a transition in the thermocline from a nearly laminar state to a fully turbulent state through the formation of shear instabilities, resulting in a significantly enhanced turbulent flux from the cool and nutrient-rich bottom waters into the surface layer. The results advance our understanding of the physical mechanisms of storm-driven turbulent mixing, and quantify the importance of storms in influencing biological activity in shelf seas over seasonal time scales. They also provide evidence for a mechanism of rapid storm-driven sea surface cooling crucial to the accurate forecasting of tropical cyclones (*Glenn et al.*, 2016).

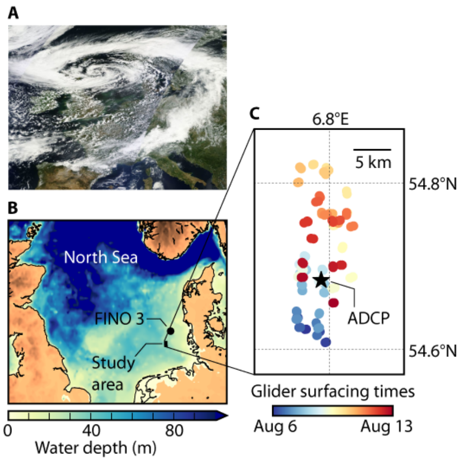

Figure 4.1: Storm Bertha and the North Sea study area. (a) True color satellite image of Storm Bertha taken from multiple passes over the North Sea at times between 09:40 and 11:25 UTC on 11 August 2014 (from NASA Worldview). (b) Topography of the North Sea showing the location of the study area, and the FINO 3 research station where the wind measurements were recorded. (c) Glider surfacing positions during the campaign, with times represented by colors. The position on the sea-bed of the Acoustic Doppler Current Profiler (ADCP) used to measure water velocities, is indicated by the black star.

4.3 Description of the experiment

Temperature, conductivity and depth data used in this letter were collected by a Teledyne Webb Research Slocum Electric autonomous underwater glider (*Davis et al.*, 2002) sampling between 54.61°N, 6.72°E and 54.82°N, 6.85°E in the period from August 6 to August 13. The presented data correspond to a subset of a longer campaign that extended over three weeks, from July 28 until August 18, and took place between 54.26°N, 6.67°E and 54.82°N, 7.54°E. Between August 3 – August 13, the glider remained close to an Acoustic Doppler Current Profiler (ADCP) moored to the sea bed as well as the measurement platform FINO3, located at 55.19°N, 7.15°E, from which we have obtained wind speed data (http://fino.bsh.de).

From August 4 to 10, a special strategy for data collection, hereafter called "spiral missions", was used. In the spiral missions, the tail ruder position of the glider is fixed, such that the glider profiles the water column in a spiral fashion. This flight pattern was chosen to produce measurements that are as close to Lagrangian as possible. The missions typically result in low spatial variability, which enables the assessment of the temporal development of fluid properties (*Schultze et al.*, 2017) (cf. supporting information). After August 13, a continuous increase in the drag coefficient of the glider due to biofouling was observed, compromising the quality of the data set collected in the last days of the campaign, which were therefore rejected. A detailed analysis of the data gathered between July 28 and August 9, as well as the methods used in data processing is presented in *Schultze et al.* (2017).

4.4 Pre-storm conditions

Prior to the arrival of Storm Bertha to the study area at approximately 00:00 UTC on 9 August 2014, winds remained relatively low at levels below 6 Beaufort (i.e., $<$ 10.8 ms^{-1}, Figure 4.2A). During these pre-storm conditions the water column consisted

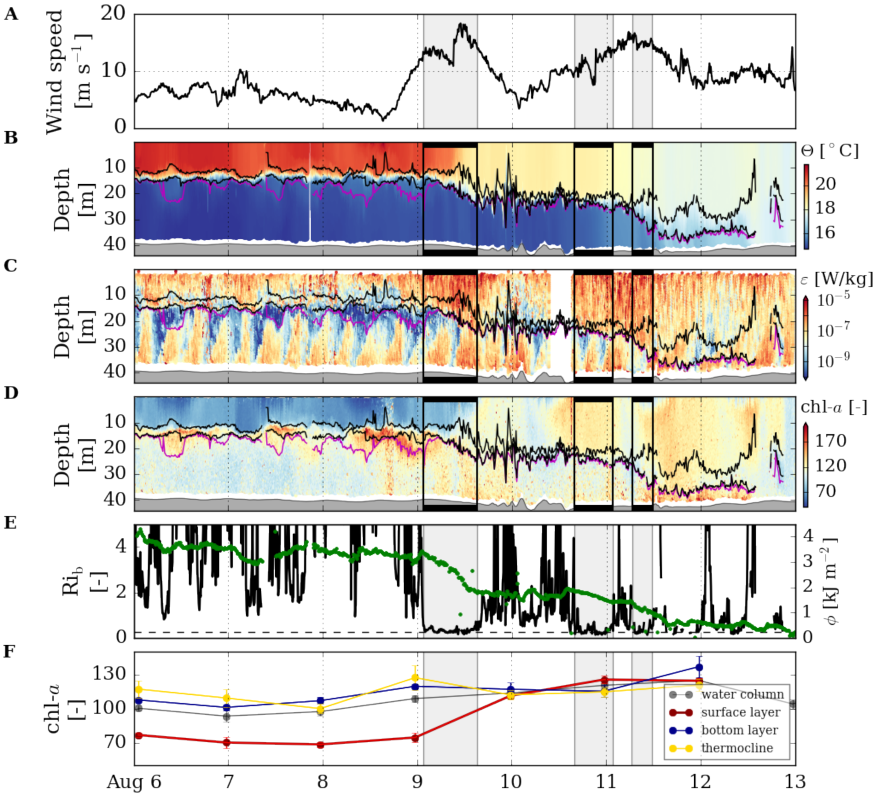

Figure 4.2: Time series of the storm forcing and the physical and biological response. The panels represent (a) wind speed at 10 m height, (b) water temperature, (c) turbulence dissipation rate, (d) chlorophyll-a fluorescence in relative units, (e) bulk Richardson number (black line) together with the stratification index (ϕ, in green), and (f) mean chlorophyll-a in the water column (grey), thermocline (yellow), bottom mixed layer (blue) and surface mixed layer (red). To avoid quenching effects, only nighttime chlorophyll measurements were taken into consideration in the calculation of mean values. In panels (b)-(d) the upper and lower boundaries of the stratified thermocline are indicated by the thin black lines, with the gray area indicating the sea bed. The magenta line denotes the depth of a second, much weaker, thermocline, defined as the depth where a 5% increase of the total change in water column temperature above that of the bottom mixed layer occurs. In each panel the times indicated by the dark rectangles (b)-(d), or gray shaded rectangles (a), (e), (f), correspond to periods of marginal thermocline stability.

of a warm (~21°C) surface mixed layer separated from the cooler (~15°C) bottom mixed layer by a strongly stratified thermocline, characterized by rapidly changing temperatures (Figure 4.2B). During conditions of summer heating, both surface and bottom mixed layers form because they are regularly mixed by turbulence arising from forcing at the boundaries of the water column: through wind and wave stresses at the water surface, and from friction between tidal currents and the sea-bed below. This turbulence can be seen in the glider-based measurements of the turbulent dissipation rate, ε in W kg^{-1}, plotted in Figure 4.2C, which quantifies the strength of the turbulence. A regular cycle of turbulence can be seen in the bottom layer at times corresponding to ebb and flood tides (approximately 6 hours apart). More irregular episodes of higher turbulence are seen in the surface mixed layer coinciding with increased wind forcing.

A different turbulence regime is found in the strongly stratified thermocline region separating these mixed layers. Turbulence in this region is characterized by much lower ε levels that display only intermittent bursts of high-turbulence. The causes of this intermittent turbulence are thought to be associated with internal wave activity and enhanced shear due to intertial oscillations (*van Haren et al.*, 1999; *Rippeth*, 2005; *Burchard and Rippeth*, 2009). However, despite these intermittent bursts, the strong stratification of the thermocline acts to damp mixed layer turbulence and limit the vertical fluxes of heat and nutrients across it. This damping action is demonstrated by the presence of a second, much weaker thermocline, that limits the extent of bottom boundary turbulence to depths often well below the main thermocline (Figure 4.2C). Stratification thus acts as a cap on the transport of nutrients, which remain largely confined to the bottom mixed layer during this time (*Floeter et al.*, 2017; *Voynova et al.*, 2017). This leads to nutrient depleted conditions in the surface layer that limit phytoplankton growth, and often result in a chlorophyll maximum located within the thermocline (*Ross and Sharples*, 2007), as seen in Figure 4.2D.

4.5 Enhanced turbulence and mixing by the storm

The role of thermocline stratification in damping turbulence is altered with the arrival of Storm Bertha at approximately 00:00 UTC on 9 August, when elevated turbulence in the thermocline reaches levels comparable to the surface and bottom mixed layers (Figure 4.2C). The physical mechanism responsible for this change is revealed by examining time series of the dimensionless bulk Richardson number, $Ri_b = \Delta\rho g h/\rho_0(\Delta U)^2$, where $\Delta\rho$ and ΔU are the density and velocity changes across the thermocline, ρ_0 is a representative water density, g the gravitational acceleration, and h denotes the thickness of the thermocline. Ri_b quantifies the relative importance of the destabilizing influence of shear, and the stabilizing influence of stratification. In pre-storm conditions, Figure 4.2E shows that $Ri_b \gg 1$, indicating that stratification is relatively strong, and largely prevents the shear from generating turbulence (*Schultze et al.*, 2017). However, as the wind forcing of the storm increases, we see periods of saturation in Ri_b at a mean ($\pm$ one standard deviation) value between 0.27 ($\pm$0.10) to 0.35 ($\pm$0.17), depending on how Ri_b is calculated (Figure 4.3, and supporting information). The value of $Ri_b = 1/4$ corresponds to a critical value in the stability of stratified shear layers: flows in which $Ri_b < 1/4$ are known to be unstable to the growth of Kelvin-Helmholtz instabilities, whereas $Ri_b > 1/4$ indicates stability (*Thorpe*, 1971; *Hazel*, 1972) (see supporting information). Thus, Figure 4.2E shows that on at least three occasions the storm drives the thermocline to a state of marginal stability. At marginal stability, an increase in the storm forcing, causing

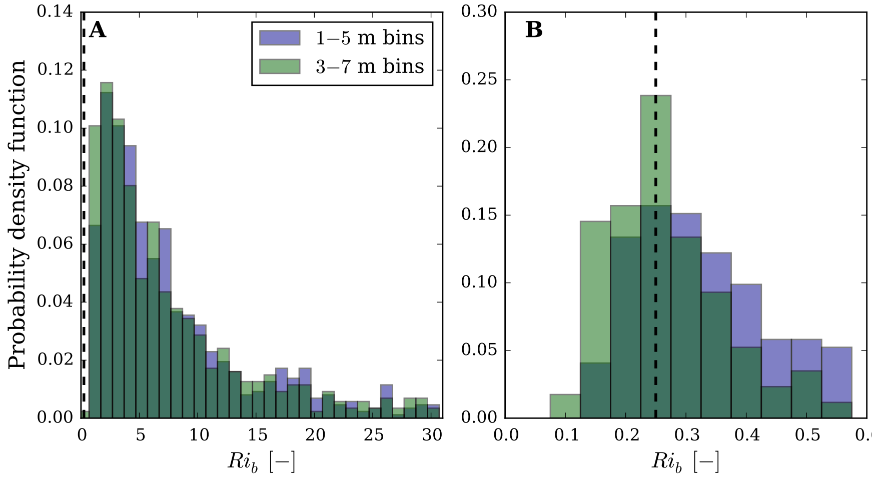

Figure 4.3: (a) Probability density of the bulk Richardson number in pre-storm conditions before the onset of marginal stability. The blue and green colors show Ri_b based on bins $1-5$ m and $3-7$ m above and below the thermocline boundaries, respectively, used for the calculation of ΔU. (b) Same as (a), but during periods of marginal stability.

increased ΔU, will lead to a drop in Ri_b below the critical value and the generation of shear instabilities that rapidly mix the thermocline. This mixing increases the thermocline thickness h, bringing it back to marginal stability. Thus, at marginal stability, any increase in the storm forcing leads to direct increases in mixing the thermocline, whereas at larger Ri_b no such direct link is present. This creates a "mixing trigger" for enhanced storm-forced thermocline fluxes, which we now discuss. Marginal stability has also been observed in a number of other forced, dissipative, stratified shear flows (*Lawrence et al.*, 2004; *Thorpe and Liu*, 2009; *Smyth and Moum*, 2013).

The turbulent state of the thermocline is altered during periods of storm-induced marginal stability. This is best seen in the distributions of ε shown in Figure 4.4, and quantified through the ratio of mean ε levels before and during the periods of marginal stability. Using the method described by *Baker and Gibson* (1987), mean values of ε in the thermocline increase 9-fold during these periods compared to pre-storm conditions (Figure 4.2C, cf. Table 4.1 in the supporting information). Since vertical turbulent fluxes are directly proportional to ε, this results in a 9-fold increase in the fluxes of important quantities such as heat and nutrients across the thermocline. A comparable increase in turbulent fluxes has also been observed through the calculation of a heat budget as an alternative means of estimating turbulent fluxes, which further supports the results obtained from our dissipation estimates (see supporting information).

As a means of quantifying the turbulent state of the thermocline, we compute the dimensionless turbulent activity index, $I_A = \varepsilon/\nu N^2$, where ν is the kinematic viscosity, and $N^2 = -(g/\rho)\partial\rho/\partial z$ is the squared buoyancy frequency, with ρ the density of seawater, and z the vertical coordinate. I_A allows for a turbulence classification into three regimes: (i) non-turbulent or laminar flow, for $I_A < 7$, (ii) transitional, anisotropic turbulence when $7 < I_A < 100$, and (iii) fully isotropic energetic turbulence for $I_A > 100$ (*Ivey et al.*, 2008). Prior to the arrival of the storm, the thermocline was marked by predominantly laminar conditions 60% of the time, with only 9% of observations consisting of energetic turbulence. However, during periods of marginal stability we find energetic (62%) or transitional (28%) turbulence in 90% of observations (Figure 4.4). This indicates a storm-

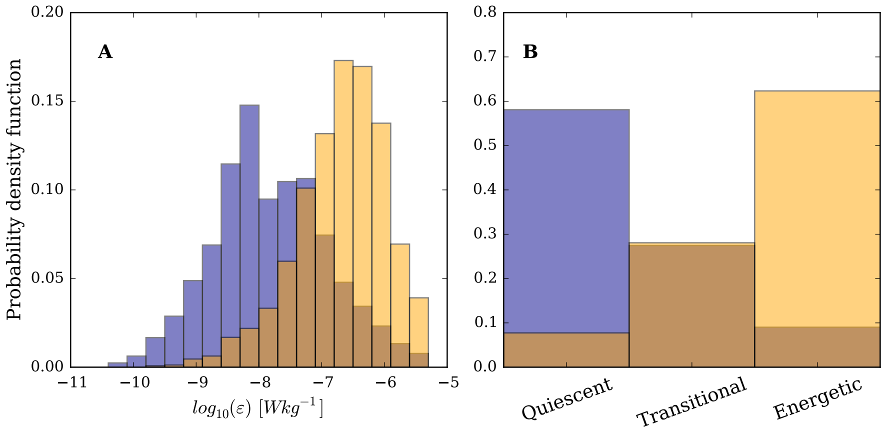

Figure 4.4: (a) Probability density functions of the dissipation of turbulent kinetic energy within the thermocline during background conditions (blue, starting from August 6) and during the periods of marginal stability (orange). (b) Turbulent activity index (I_{A}) following the color code from (a). A "quiescent" flow has been defined when $I_{\mathrm{A}} \leqslant 7$ and "energetic" when $I_{\mathrm{A}} \geqslant 100$. Transitional flow is found between quiescent and energetic conditions.

induced transition to a turbulent thermocline with the onset of marginal stability.

One result of this enhanced thermocline turbulence is a rapid destruction of the stratification through turbulent mixing. A quantitative measure of the strength of stratification is given by $\phi = \int_0^H (\rho_{\mathrm{mix}} - \rho) gz \, \mathrm{d}z$, with the integral taken over the depth of the water column H. Expressed in kJ m^{-2}, ϕ is the amount of potential energy contained in the stratification, relative to the completely mixed state. This mixed state is characterized by a constant water density of $\rho_{\mathrm{mix}} = \int_0^H \rho \, \mathrm{d}z/H$. Figure 4.2E shows that the greatest drops in ϕ coincide with the periods of marginal stability. In fact, from the onset of marginal stability at 01:30 UTC on August 9, to the time of complete mixing shortly before August 13, 71% of the total drop in stratification occurs during the three periods of marginal stability, with the remainder occurring after the thermocline has descended well into the bottom boundary layer. These periods of marginal stability also correspond to drops in the temperature of the surface mixed layer (Figure 4.2B), as a result of the increase in turbulent heat flux across the thermocline.

As a means of assessing the biological response of this enhanced mixing we examine glider-based measurements of chlorophyll-a fluorescence (hereafter chlorophyll), expressed in relative units in Figure 4.2D,F. Pre-storm conditions show low chlorophyll in the surface mixed layer, consistent with low nutrient availability. However, with the passage of the storm, chlorophyll in the surface mixed layer rose by 67%, bringing it to levels comparable to those in the thermocline and bottom mixed layer. Such a biological response is primarily related to a redistribution of phytoplankton cells over the water column, but also to an observed net increase in chlorophyll (see supporting information). Due to a myriad of influences affecting phytoplankton growth (e.g., light and temperature dependence, predation), higher chlorophyll cannot be readily associated with primary production without the support of direct measurements of biomass. An increase in photosynthetic activity as a result of primary production is likely responsible for the observed increase in chlorophyll over the water column (*Falkowski and Kiefer*, 1985; *Babin et al.*, 2004), however changes in the physiological status of the cells cannot be ruled out (*Kiefer*, 1973;

Falkowski and Kiefer, 1985).

4.6 Implications for the shelf seas

Although storms are known to episodically increase biological productivity (*Dagg*, 1988; *Babin et al.*, 2004; *Walker et al.*, 2005; *Rumyantseva et al.*, 2015), the importance of such extreme events on a seasonal basis is currently a matter of debate (*Hanshaw et al.*, 2008; *Foltz et al.*, 2015). Given that in our study, thermocline fluxes were observed to increase 9-fold during the 29 hours of marginal stability conditions, we find that Storm Bertha was responsible for a flux equivalent of 11 days at normal background levels. Since the mean duration of the stratified season in this region of the North Sea is 85 days (*van Leeuwen et al.*, 2015; *Carpenter et al.*, 2016), this implies that the storm would be responsible for 13% of the mean seasonal fluxes, thus contributing a significant share of the local budget. Such storm conditions, with wind speeds of 6 Beaufort or greater (i.e., > 10.8 ms^{-1}), are found at an average of 8.3 days during the summer stratified period. Assuming that a similar fraction of time is spent at marginal stability (67%), storms would then account for approximately 40% of the total mean seasonal fluxes. This indicates that during the stratified season, net storm-induced turbulent fluxes are comparable to the net background flux. Therefore, we find that storms act as a significant supply of nutrients to the depleted surface mixed layer during the summer growing season.

In a changing climate system, for which most studies predict an increase in the frequency and strength of storms over the North Sea (*Feser et al.*, 2015), it is therefore crucial to investigate the extent to which storms impact ecosystem dynamics on a seasonal basis. Changes in storm-enhanced mixing will have direct implications for net phytoplankton growth (*van Beusekom and Diel-Christiansen*, 2009; *Rumyantseva et al.*, 2015) and carbon dioxide uptake (*Thomas et al.*, 2004), as well as will cause alterations in the timing of the fall bloom, and the duration of summer stratification (*Richardson and Pedersen*, 1998). In addition, rapid storm-induced changes in sea surface temperature on the continental shelf, caused by enhanced thermocline mixing, have been found to be a crucial unknown component influencing the evolution and forecasting of tropical cyclones (*Glenn et al.*, 2016). Since the shelf seas have a disproportionately high influence on global biological production (*Simpson and Sharples*, 2012), their response to extreme storm events must be understood in order to predict future alterations from storms.

Acknowledgments

We would like to acknowledge B. Baschek, Y. Voynova, and J.-P. Mellado for helpful discussions. Support for the preparation, deployment, and recovery of instrumentation were provided by R. Kopetzky, B. Peters, A. Werner, M. Heineke and the captain and crew of the *RV Ludwig Prandtl*. Funding was provided through the Polar Regions and Coasts in the Changing Earth System (PACES II) programme of the Helmholtz Association. We would like to acknowledge the German Federal Ministry of Economic Affairs and Energy (BMWi) and the Project Management Jülich (PTJ), which made the wind measurements of the platform Fino 3 available for use. The wind data can be assessed in the Fino database under http://fino.bsh.de. We also thank the German Federal Maritime and Hydrographic Agency (BSH) for their support in deploying and recovering the ADCP.

4.7 Supplemental Information

Text S1. Extended Methods

In the supporting information, unless otherwise specified, we extend the results presented in the main article by reporting on the measurement period August 3 – August 13, during which the glider is close to the ADCP.

Glider-based measurements

The glider was equipped with a Seabird free flush CTD (Seabird SBE41 CTD, 0.5 Hz) and a Wetlabs FLNTU fluorescence and turbidity optical sensor (1 Hz). The CTD measurements were used to calculate temperature, the buoyancy frequency, and in the identification of the thermocline boundaries. Due to errors in the time delay and response characteristics of the CTD conductivity cell, the calculation of density profiles was carried out by assuming that the vertical structure of the temperature field was representative of density, and the total change in density across the pycnocline is calculated based on conductivity and temperature changes in the mixed layers. More details are discussed in *Schultze et al.* (2017).

The glider also carried a navigation pressure sensor (Micron Instruments, MP50 – 2000), an attitude sensor (TCM3), an altimeter (AIRMAR Technology), an Iridium modem, and a global positioning system.

Turbulence measurements

A microstructure package (MicroRider-1000LP, Rockland Scientific International) carrying two shear microstructure sensors (SPM – 38, 512 Hz) was mounted on the top of the glider and recorded shear microstructure measurements during both up- and downcasts. The characterization of turbulence during the measurement period was performed through the calculation of the dissipation of turbulent kinetic energy ε.

Under the assumption of isotropic turbulence at small scales, ε was calculated from one component of the shear tensor following the general methods extensively described in *Lueck et al.* (2002); *Wolk et al.* (2002); *Fer et al.* (2014). A full description of the methods used to determine ε, and the steps taken to control the quality of glider-based measurements, are found in *Schultze et al.* (2017). Data processing encompasses the conversion of the collected measurements into physical units, matching the time and pressure signals of the glider and the microstructure package, and the estimation of the velocity of the glider, which is used to obtain shear microstructure information from the shear probes. Taylor's hypothesis of frozen turbulence enables the conversion of the shear measurements from the frequency domain into the wavenumber domain, which are used to generate power spectra. The dissipation of turbulent kinetic energy is calculated through the integration of the power spectra (Φ) over an appropriate wavenumber range $\varepsilon \approx 7.5\ \nu \int \Phi(k)dk$, where ν is the kinematic viscosity of seawater (*Lueck et al.*, 2002; *Wolk et al.*, 2002). Subsequently, the quality of the shear spectra is controlled using the procedure described in *Schultze et al.* (2017) and the conditions for satisfying Taylor's hypothesis are tested following *Fer et al.* (2014). Dissipation estimates above $\varepsilon > 10^{-5}$ Wkg^{-1} and below $\varepsilon < 10^{-11}$ Wkg^{-1} were related to badly resolved spectra and therefore disregarded in the scientific analysis, with no influence on the final results. Approximately 4% of the data were rejected during quality control, 84% of which can be explained by low quality spectra. A total of 117,557 ε measurements were left for scientific analysis.

Due to the sensitivity of ε to the glider flight characteristics, a check can be performed by comparing the up- and downcasts of the glider, which are found to have different

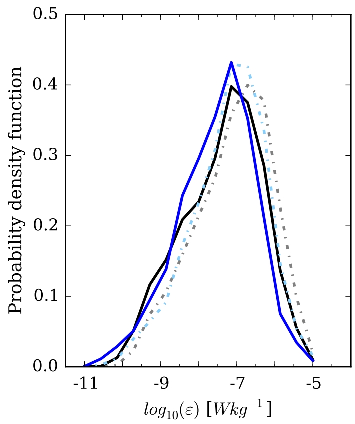

Figure 4.5: Probability density function (PDF) of the dissipation of turbulent kinetic energy ε for downcasts (black) and upcasts (blue) (cf. *Schultze et al.* (2017)) for the period between August 6 and August 13. The dot-dashed lines in the respective colors depict the PDFs of the raw ε estimates. The solid lines show the PDFs of ε obtained after the use of the Goodman algorithm (*Goodman et al.*, 2006).

flight behaviors. Dissipation estimates from up- and downcasts agreed by a factor of 0.6 (median), which points to the accuracy of the flight model, considering that ε varies over several orders of magnitude. Throughout the water column, ε exhibited a log-normal distribution (Figure 4.5), and the interquartile range of the ratio between up- and downcast measurements, defined here as the 25^{th} and the 75^{th} percentiles, was 0.4 – 0.9. This uncertainty in the glider flight behavior does however, contribute to an additional source of uncertainty in ε that is otherwise estimated at a factor of two (*Dewey and Crawford*, 1988; *Moum et al.*, 1995). Due to the agreement between up- and downcasts, the data are analyzed together to enhance statistical significance.

Prior to obtaining ε estimates, the Goodman algorithm (*Goodman et al.*, 2006) is applied to eliminate vibration noise from the shear signal. The Goodman algorithm is used as a measure to avoid an overestimation of ε through contamination with glider motions. It has been suggested that the use of the algorithm can lead to an underestimation of ε (*Fer et al.*, 2014), however its influence appears as a shift in the distribution by the factor 1.9 (Figure 4.5). This possible influence of the Goodman algorithm is discussed further below in the context of the heat budget.

Chlorophyll-a fluorescence

The WET Labs FLNTU sensor measured turbidity at a wavelength of 700 nm, and chlorophyll-*a* (chl-*a*) fluorescence with excitation at 470 nm and emission recorded at 695 nm at a sampling rate of 1 Hz. The sensor measures fluorescence, a proxy for the concentration of chl-*a*, and is configured to measure in the range of 0.01 – 50 μgL^{-1} chl-*a*, with a linear response over this span of pigment concentration. The fluorometer mounted on the glider was factory calibrated, but lacked field calibration. Considering that the amount of chl-*a* in phytoplankton cells varies among different phytoplankton groups, and depends on the physiological status of the cells, the chl-*a* fluorescence data is reported in this letter in a qualitative sense. Hence, the data are presented in relative units. Spikes in the turbidity and chl-*a* signal were identified and discarded by selecting a maximum noise threshold that corresponded to twice the 99$^{\text{th}}$-percentile value of the complete dataset. Daytime variations in chl-*a* fluorescence due to quenching were avoided by considering only nighttime measurements in the calculations, as well as in Figure 4.2F.

To ensure that the enhanced chl-*a* concentrations measured during and after the periods of marginal stability were not a result of storm-triggered sediment resuspension, we have compared both signals against each other (Figure 4.6). Each data point in Figure 4.6 and Figure 4.2F correspond to an average of the measurements collected during the night (5 pm – 2 am UTC) in the corresponding layers. No clear relation between turbidity and chl-*a* was observed in the surface or bottom mixed layers, nor in the thermocline, suggesting that changes in chl-*a* occurred largely independent from sediment concentration (Figure 4.6).

The large and continuous increase in the drag coefficient of the glider after August 13 impedes the consideration of the turbulence measurements collected thereafter. Measurements from the remaining sensors should also be regarded with extreme caution after August 13. It is however, interesting to note that an approximately 2-fold increase in chl-*a* integrated over the water column was observed between August 8 and August 16. This increase in chl-*a* could be a result of spatial variability (as spiral missions were not performed), but may also indicate that significant biological growth has occurred, consistent with the rapid biofouling.

ADCP data

Horizontal current velocities were sampled from 5 to 38 m depth every 10 minutes by an RDI 600 kHz bottom-mounted ADCP in the vicinity of the buoy Nordseeboje 3 (NSB3, 54.68°N, 6.78°E) measurement station. The ADCP data were used in the calculation of the bulk Richardson number for the discussion of marginal stability triggered by the storm.

Wind data

Wind velocities at 10 m height were obtained through the power law for wind profiles $w_{10} = w_{30}(z_{10}/z_{30})^{\alpha_\mathrm{w}}_{\mathrm{w}}$, where $\alpha_\mathrm{w} = 1/7$, and w and z stand for the wind velocity at a given height, respectively (*Hellmann*, 1919; *Spera and Richards*, 1979). The subscripts denote estimates at 10 m and 30 m.

Calculation of the bulk Richardson number

The calculation of $Ri_b = g\Delta\rho h/\rho_0(\Delta U)^2$ requires an estimation of ΔU, h, and $\Delta\rho$, from the measurements. The procedure used to calculate each of these is now discussed in turn.

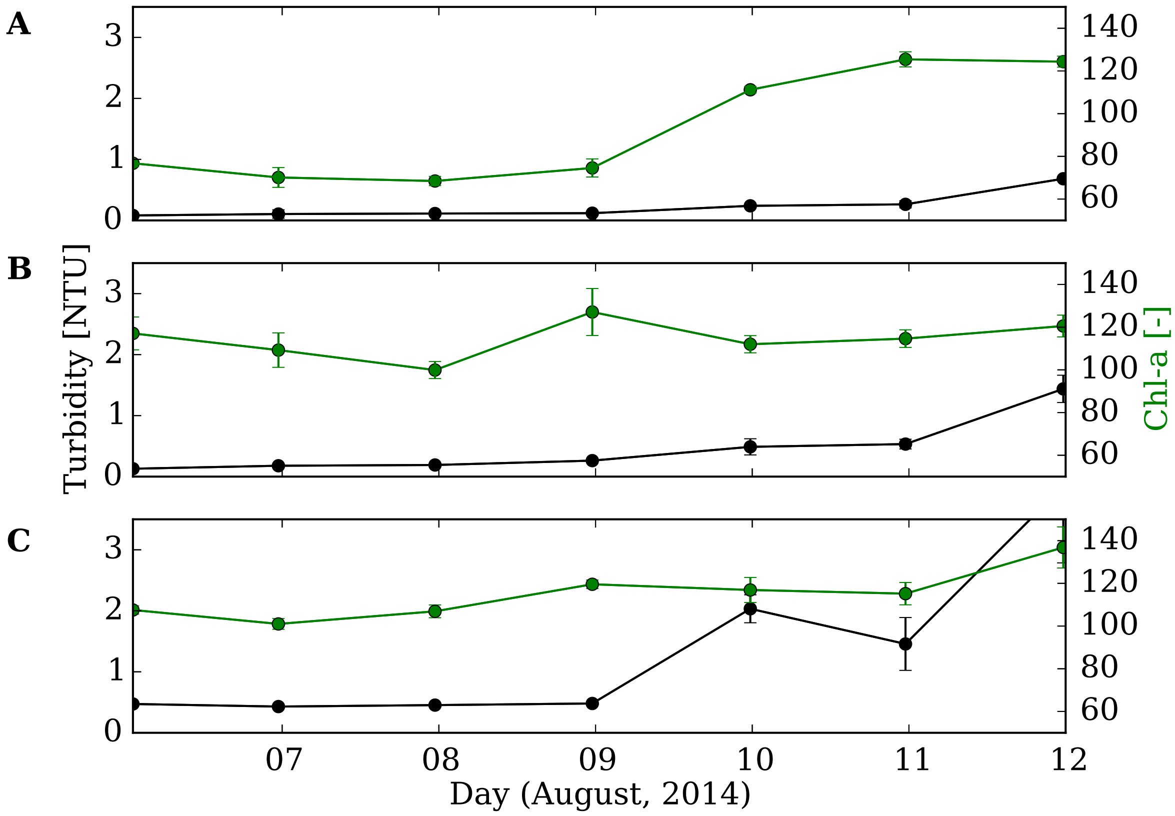

Figure 4.6: Chlorophyll-a (raw units) and sediment concentration (NTU) in the surface mixed layer (a), thermocline (b) and bottom mixed layer (c). The error bars indicate one standard deviation from the mean. Changes in chl-a concentration in the three different layers are to a great extent independent from the storm-triggered resuspension of sediments.

ΔU must be chosen as being representative of the total change in velocity across the shear layer. It is defined as $\Delta U = [(U_\mathrm{s}-U_\mathrm{b})^2+(V_\mathrm{s}-V_\mathrm{b})^2]^{1/2}$, where U, V represent eastward and northward horizontal velocities, respectively, and the subscripts refer to averages in the surface (s) and bottom (b) layers. These averages are computed across bins situated $1-5$ m above $(U_\mathrm{s}, V_\mathrm{s})$ and below $(U_\mathrm{b}, V_\mathrm{b})$ the thermocline boundaries. These bins, as well as the current magnitudes $(U^2+V^2)^{1/2}$, are shown in Figure 4.7. It can be seen that the bins adequately capture the total change in current across the thermocline, while not extending too far into the bottom boundary layer, or into the noisy near-surface levels during strong wind forcing. Note that if the bins reach outside of the ADCP measurement range due to excursions of the thermocline height, the upper or lower boundary is adjusted to this range (Figure 4.7). The choice of a different depth interval (e.g. $3-7$ m) for the bins does not significantly change the results (Figure 4.3). Independently of the bins chosen, low Ri_b is found in periods of stronger storm forcing, however the mean ($\pm$ one standard deviation) saturation level of Ri_b varies between 0.27 ($\pm$0.10) and 0.35 ($\pm$0.17) depending on the selected averaging interval, varying between $1-5$ m and $3-7$ m (Figure 4.3).

In order to compute the thermocline thickness, h, we follow the method outlined in

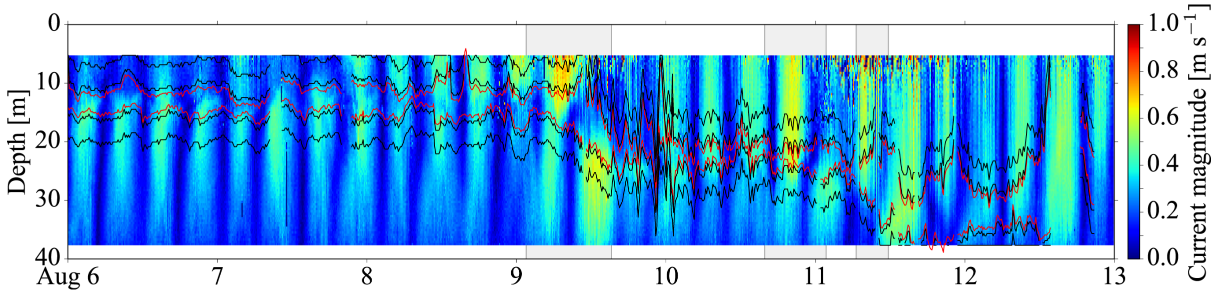

Figure 4.7: Current magnitude measured during the experiment by the bottom-mounted ADCP. Red lines indicate the location of the thermocline, and black lines the boundaries of one choice of the bins used for averaging in the calculation of ΔU, i.e., defined as 1 to 5 m above and below the thermocline boundaries. Times of marginal stability are shown in gray.

Carpenter et al. (2016), which we now briefly describe. In the discussion that follows, all temperatures referred to are understood to be conservative temperature calculated based on the TEOS-10 equation of state (*IOC et al.*, 2010). The vertical temperature profile measured by the glider is resorted to be monotonically decreasing with depth. From this sorted profile, $T_*(z)$, the total change in temperature, ΔT, is estimated by averaging the upper and lower four measurement points and taking the difference between these values. If $\Delta T < 0.3$°C, the water column is considered completely mixed, and no thermocline is identified. Otherwise, h is calculated as the vertical distance between the levels over which the central $0.9\Delta T$ change in temperature occurs. *Carpenter et al.* (2016) compared this measure of h to an alternative definition, h_2, in *Smyth et al.* (2007) based on the integral

$$h_2 = \int_0^H \left\{1 - \left[\frac{T_*(z) - (T_s + T_b)}{\Delta T}\right]^2\right\} \mathrm{d}z. \tag{27}$$

The two different definitions resulted in mean values of thermocline thickness that differ by less than 4%. This is encouraging because when $T_*(z)$ is taken as a hyperbolic tangent curve, and the thermocline thickness is defined through the maximum gradient by $h_3 = \Delta T/(\mathrm{d}T_*/\mathrm{d}z)_{\max}$, then the integral representation gives $h_2 = h_3$. This shows that our chosen definition of h generally corresponds well to the hyperbolic tangent model that is commonly used in studies of the linear stability properties of stratified shear layers, as discussed in the following.

The density change across the thermocline, $\Delta\rho$, is calculated based on both the temperature change, ΔT, as discussed above, as well as the accompanying change in salinity at the top and bottom of the mixed layers. In this case, the response of the conductivity cell and matching with the thermistor does not affect $\Delta\rho$.

Text S2. Extended results and further supporting information

Intensity of turbulence within the thermocline

The identified periods of marginal stability are characterized by significantly higher levels of dissipation of turbulent kinetic energy, ε. Similar to Figure 4.4, Figure 4.8 shows probability density functions of ε and I_{A} measurements taken within the thermocline for two different periods corresponding to background turbulence levels, and during the defined periods of marginal stability. Background conditions are identified to be in the

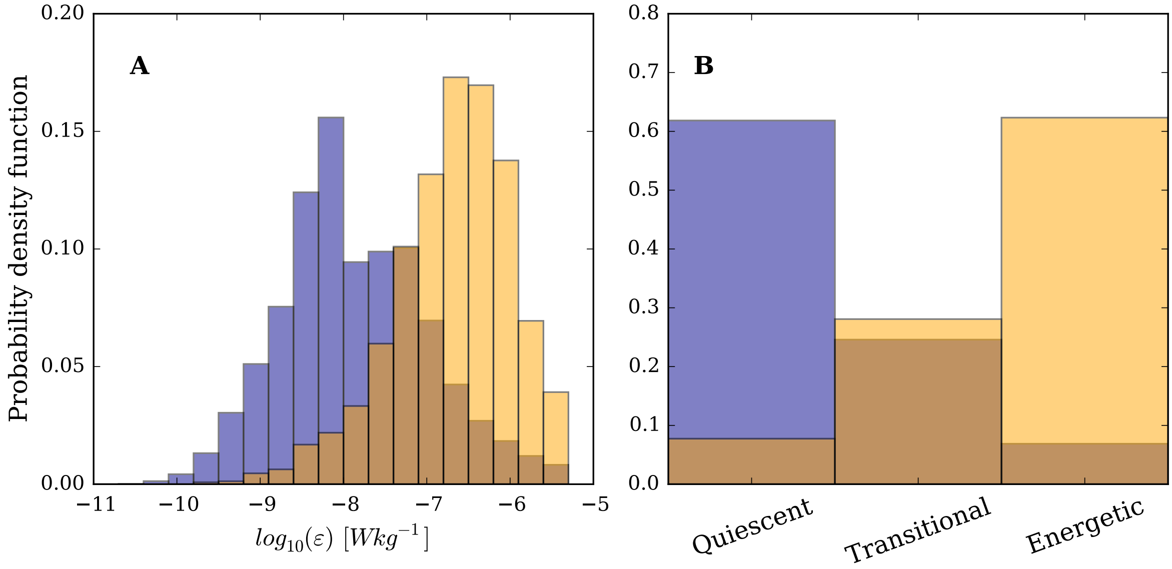

Figure 4.8: (a) Probability density functions of ε within the thermocline. Blue indicates background conditions (starting from August 3) and orange indicates conditions during the periods of marginal stability. (b) Same as in (a) for the turbulent activity index (I_{A}). The flow has been defined as "quiescent" for $I_{\mathrm{A}} \leqslant 7$ and "energetic" for $I_{\mathrm{A}} \geqslant 100$. Transitional flow is found for $7 < I_{\mathrm{A}} < 100$.

time range beginning on August 3, and extending to 19:54 UTC on 8 August. This end time was chosen before a clear increase in ε associated with the first storm period, before the first marginal stability period. In Figure 4.8b, a change in the turbulent regime in the thermocline from mainly quiescent to predominantly energetic was observed, which can be largely explained by higher rates of dissipation of turbulent kinetic energy during marginal stability periods (Figure 4.8a).

Figure 4.9 depicts the entire time series of ε available for 2014 (cf. *Schultze et al.* (2017)). We now focus on the difference between the average dissipation measured in periods of marginal stability occurring during storm Bertha, $\langle\varepsilon\rangle_{\mathrm{ms}}$, and average turbulence levels obtained under background conditions before the onset of marginal stability, $\langle\varepsilon\rangle_{\mathrm{bg}}$. The average is taken over all values of ε within the thermocline during the specified time period indicated by the subscript. Because ε distributions are approximately log-normal, the data is averaged based on the method described by *Baker and Gibson* (1987). Specifically, we calculate $\langle\varepsilon\rangle = \exp(\mu + \sigma^2/2)$, where μ and σ are the arithmetic mean and the variance of $\ln(\varepsilon)$, respectively. A summary of the statistics of ε is presented in Table 4.1.

We find that the mean dissipation of turbulent kinetic energy in the thermocline during the periods of marginal stability is $\langle\varepsilon\rangle_{\mathrm{ms}} = 1.2 \times 10^{-6}$ Wkg^{-1}. The mean of background dissipation in the thermocline was $\langle\varepsilon\rangle_{\mathrm{bg}} = 1.3 \times 10^{-7}$ Wkg^{-1}, suggesting that storm fluxes are a factor of 9 higher than stratified background levels (see Table 4.1 and Figure 4.8).

Thermocline fluxes and the heat budget

The intensity of turbulent mixing triggered by the storm reported in this study can be independently tested through the calculation of a heat budget (*Palmer et al.*, 2008; *Schultze et al.*, 2017). The calculated heat budget lies within the time frame at which

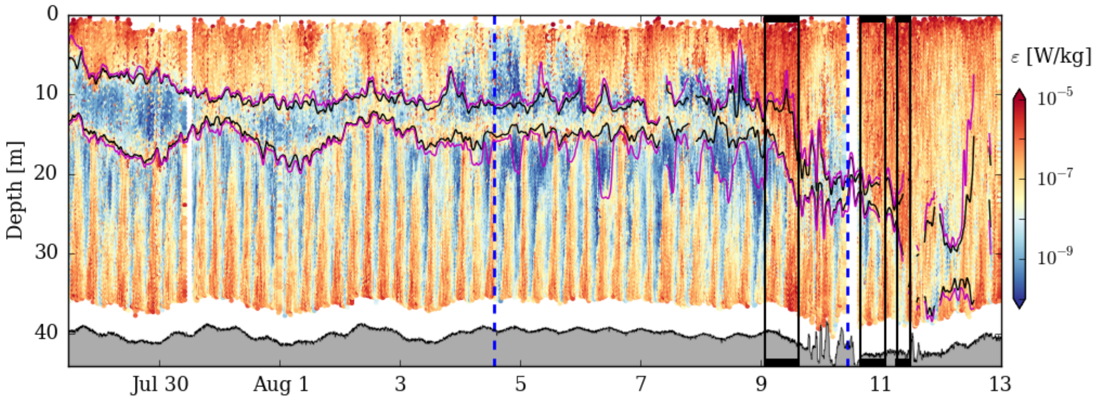

Figure 4.9: Decadic logarithm of the dissipation of turbulent kinetic energy ε for downcasts from the beginning of the research campaign of 2014 (cf. *Schultze et al.* (2017)). The thin black and magenta lines represent two different definitions of the thermocline. The black rectangles show the three identified periods of marginal stability. The gray area at approximately 40 m depth represents the sea bed. The vertical blue dashed lines depict the period at which the spiral missions took place.

Table 4.1: Mean, median and interquartile range of ε for the thermocline before and during periods of marginal stability (MS). Mean values were calculated according to the method described by *Baker and Gibson* (1987). The 25^{th} and the 75^{th} percentiles are given under "25th" and "75th", respectively. Sample sizes are: 13709 (Aug. 3 - Aug. 9), 3219 (during marginal stability, i.e. MS). All values are given in Wkg^{-1}.

	Before MS 08/03 – 08/09	During MS 08/09 – 08/13
minimum	1.4×10^{-11}	4.2×10^{-11}
maximum	9.8×10^{-6}	9.8×10^{-6}
mean	1.3×10^{-7}	1.2×10^{-6}
median	6.4×10^{-9}	2.4×10^{-7}
25th	1.2×10^{-9}	6.5×10^{-8}
75th	3.6×10^{-8}	6.5×10^{-7}

Table 4.2: Summary of heat flux calculations using both direct turbulence measurements, as well as the heat budget methods. The range in heat fluxes for the turbulence measurements reflects the use of the Goodman algorithm, producing lower heat fluxes. The values are summarized for the periods before and during marginal stability (MS).

	Heat budget	Turbulence measurement
Before MS (W m^{-2})	113	60-100
During MS (W m^{-2})	1718	644-1076
Ratio	15	11

the spiral missions were conducted, and includes the first period of marginal stability. Limiting the analysis to include only the spiral missions was found necessary by *Schultze et al.* (2017) in order to eliminate terms in the heat budget due to lateral spatial variability.

With the passage of the first storm period, a rapid decrease of surface mixed layer temperature by 2.2°C is observed (all temperatures used are conservative, as described in *IOC et al.* (2010)), whereas the mean temperature of the water column remained largely constant at 17.0 (±0.2) °C, with a net increase of 0.06°C. This suggests a relatively small air-sea heat flux during the first marginal stability period. In addition, the change in heat content of the thermocline was smaller than that of the minimal net change over the entire water column, and is therefore neglected. Thus, considering that the heat transfer between the sea surface and the atmosphere is small, and neglecting lateral advection, the heat flux, Q_T, across the thermocline can be estimated from the temporal rate of change of temperature in the surface mixed layer, T_{SML}, from $Q_T = c_p \rho_0 H_{\mathrm{SML}}(\mathrm{d}T_{\mathrm{SML}}/\mathrm{d}t)$. Here we have used H_{SML} to represent the thickness of the surface mixed layer, and $c_p = 3993$ Jkg^{-1}K^{-1} for the heat capacity of sea water at 20°C. Given the evolution of the depth and temperature of the surface mixed layer, a mean heat flux can be found, which we denote by $\bar{Q}_T$, where the overbar henceforth represents an arithmetic mean. This method results in mean background heat fluxes of 113 Wm^{-2}, as well as during the first period of marginal stability of 1720 Wm^{-2}. These flux estimates are independent of those from direct turbulence measurements, and serve as an approximate check on the turbulent quantities. A summary of the heat fluxes calculated from the different methods is shown in Table 4.2.

An average heat flux across the thermocline can also be obtained directly from the dissipation measurements as $\bar{Q}_T = \rho_0 c_p K_{\mathrm{thm}} \overline{\partial T/\partial z}$, where $\rho_0 = 1025$ kgm^{-3} is a reference density, and $\overline{\partial T/\partial z}$ is the mean vertical temperature gradient within the thermocline. The averaged turbulent diffusivity through the thermocline, K_{thm} [m^{2}s^{-1}], is estimated for each half profile (up- and downcasts) through $K_{\mathrm{thm}} = h^{-1} \int_{h_{top}}^{h_{bot}} K_\rho \, dz$, where h is the thermocline thickness, and h_{bot} and h_{top} are the thermocline boundaries. The turbulent diffusivity is calculated as $K_\rho = \Gamma \varepsilon N^{-2}$, where $\Gamma = 0.2$ is the mixing efficiency that was set to a constant value following several studies (*Gregg et al.*, 2012; *Cyr et al.*, 2015). Moreover, K_ρ was estimated using both ε with, and without, the Goodman algorithm. An extensive discussion on the effect of different parameters on the calculation of the heat budget (e.g. mixing efficiency, thermocline definition) is provided in *Schultze et al.* (2017).

Considering the thermocline boundaries corresponding to the region where the central 90% of the total change in temperature occurs, turbulent fluxes obtained through our dissipation estimates were able to explain 44 – 68% of the temperature loss in the surface mixed layer during the first period of marginal stability. The spread refers to the choice of using the Goodman algorithm, and is within the uncertainty range of ε estimates. Further, the mean heat flux obtained through the turbulence measurements during the first period of marginal instability was 10 – 11 times greater than the background flux of 60 – 100 Wm^{-2} (cf. *Schultze et al.* (2017)) (Table 4.2). Thus, considering the measurement uncertainty of ε estimates, agreement is found between the heat flux estimates from the two methods.

Stability properties of stratified shear layers

A general necessary (but not sufficient) criterion for the stability of stratified shear flows is that the gradient Richardson number $Ri_g(z) < 1/4$ somewhere in the water column (*Miles*, 1961; *Howard*, 1961), where $Ri_g(z) = N^2/(\mathrm{d}U/\mathrm{d}z)^2$. However, if we constrain the profiles of horizontal velocity, $U(z)$, and $N^2(z)$, such that the thickness of the shear layer and the density stratified region are equal (*Smyth et al.*, 2007), and centered with respect to each other, then the stability properties may be described entirely by Ri_b, as in (*Thorpe*, 1971; *Hazel*, 1972). The definition of length scale used in Ri_b corresponds to h_3, defined above. In this case, the stability boundary is found to be described by $Ri_b = 0.25$ for an analysis of hyperbolic tangent, error function, and piecewise linear profiles (*Miles and Howard*, 1964; *Thorpe*, 1971; *Hazel*, 1972; *Smyth et al.*, 2007). This is related to the gradient Richardson number condition above, as the minimum of $Ri_g(z)$ is equal to Ri_b, and found to occur in the center of the stratified layer. In all of these cases that we are aware of $Ri_b < 0.25$ serves as a *sufficient* condition for instability. This does not, however, constitute a proof that all profiles observed in our study area should have $Ri_b = 0.25$ as a stability boundary. This seems likely though given the close correspondence between the observations at $Ri_b = 0.25$ during heightened storm forcing.

Occurrence of elevated wind speeds in the North Sea during summer

From an analysis of the wind speed measurements at the FINO 3 offshore platform from the years 2010 – 2016, we are able to assess the relative occurrence of summer storm events. Here the summer is taken during the months of May, June, July, August, corresponding to the stratified period (*Carpenter et al.*, 2016), and a storm event is defined as wind speeds of Beaufort 6 and higher, i.e., greater than 10.8 ms^{-1}. This strength of wind forcing was shown in Figure 4.2 to be sufficient to initiate marginal stability in the thermocline during conditions of strong stratification. The analysis shows that an average of 8.3 days (200 hours) of storm conditions occur per summer season (Figure 4.10). Given the rapid mixing that was measured during these conditions in Storm Bertha, we may provide a rough estimate of the seasonal importance of these storms under the assumption of a similar ocean response. During Storm Bertha, we observe that 67% of storm conditions exhibit marginal stability. Given also that an average of 85 days of continuous stratification are found in the summer season (consisting of 123 days), we have 69% of the summer with continuous stratification. Finally, during these marginal stability periods, an increase in turbulent thermocline fluxes by a factor of 9 was found. This leads to the equivalent of 35 days of storm-induced fluxes at background stratified levels, corresponding to 40% of the summer stratified fluxes.

There are many uncertainties associated with this analysis that are not quantified here, such as dependencies on wind speeds, stratification levels, as well as thermocline depths and thicknesses. Note also that the definition of a storm as greater than 10.8 ms^{-1} wind speeds is somewhat arbitrary, and the onset of marginal stability is observed at wind speeds of close to 10 ms^{-1} at the beginning of the second storm event. In addition, we have neglected increases in storm-driven mixing that take place outside of the periods of

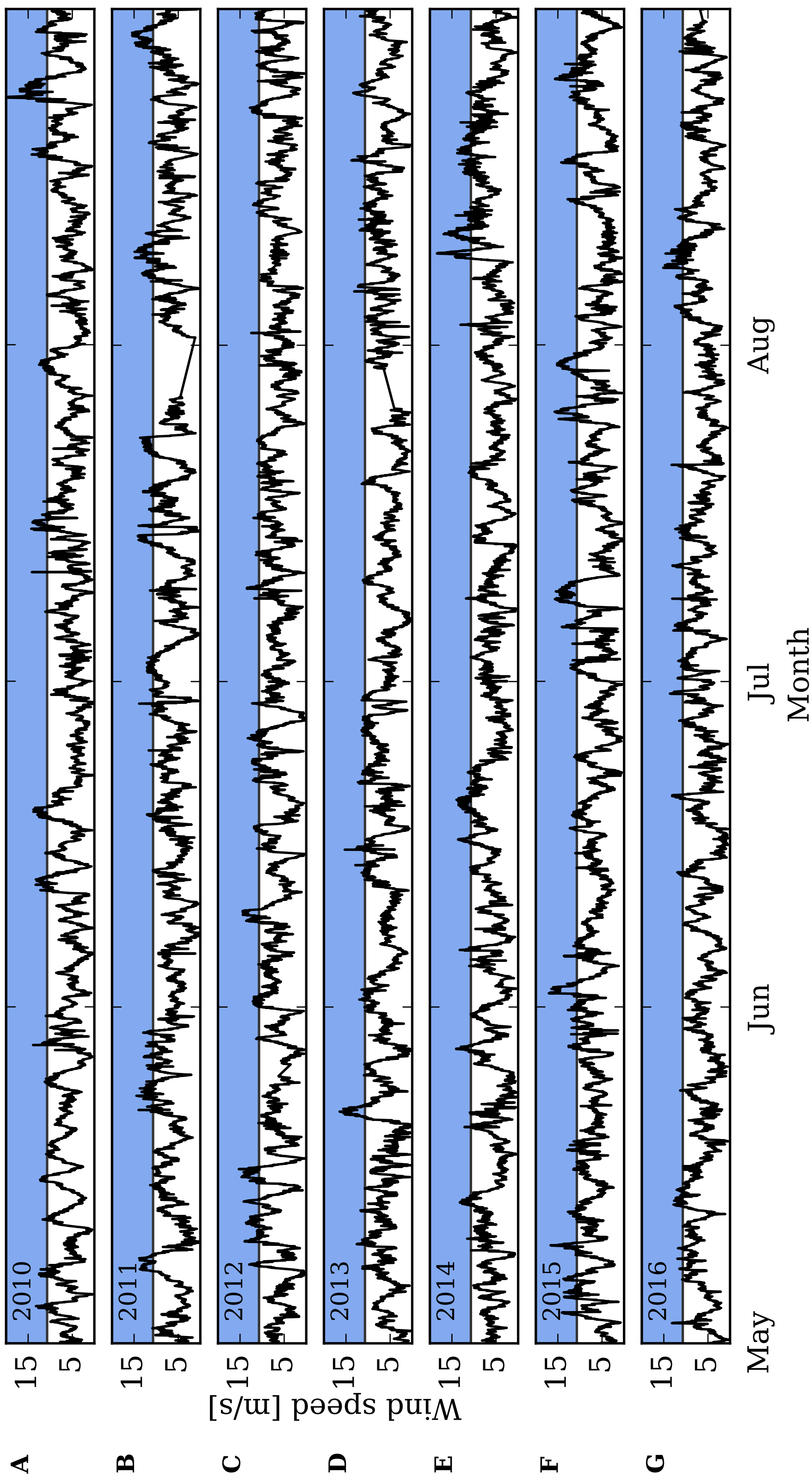

Figure 4.10: (a)-(g) Wind velocities recorded by the platform FINO 3 at 55.19°N, 7.15° between 2010 and 2016. Velocities have been converted to 10 m height. The blue shaded area marks wind speeds equal to and higher than 6 Beaufort ($\geqslant 10.8\mathrm{ms}^{-1}$).

marginal stability. This could also have an influence in increasing storm-driven fluxes, as seen at the end of the last marginal stability period in Figure 4.2E. Despite these uncertainties, these findings highlight the potential importance of storms in providing a significant fraction of seasonal fluxes on the North Sea shelf.

5 Increased mixing and turbulence in the wake of offshore wind farm foundations

This chapter is a reprint of the manuscript "Increased mixing and turbulence in the wake of offshore wind farm foundations", which is in preparation for submission.

Citation: Schultze, L. K. P., Merckelbach, L. M., Raasch, S., & Carpenter, J. R. (2018). Increased mixing and turbulence in the wake of offshore wind farm foundations. In preparation for submission.

Keypoints

- Enhanced mixing in the wake of monopiles and its dependence on stratification is traceable in field observations, as well as numerical experiments.
- Elevated levels of the dissipation of turbulent kinetic energy are found in a narrow region downstream of single foundation structures, with a bulk mixing efficiency of approximately 10%.
- One monopile promotes little additional mixing of the water column, however enhanced scalar transport occurs in close proximity to single structures.

5.1 Abstract

The optimization of technologies based on renewable energy sources has been promoted in the past years and sustained the development of offshore wind farms in stratified regions of shelf seas. The addition of wind turbines to the water column poses an anthropogenic source of turbulence, in which single pylons remove power from the flow that is fed into turbulent mixing. A quantification of such mixing is performed for the first time by means of field observations of single wind turbine wakes together with high-resolution large-eddy simulations of four different stratification strengths. The wake of the monopile is narrow and highly energetic within the first 100 m, with the dissipation of turbulent kinetic energy well above background levels. Directly behind the turbine, there is enhanced scalar transport from the bottom mixed layer into the stratified region. The upwelled passive scalar remains confined within stratification until the end of the domain and suggests that upwelled nutrients in a similar scenario would remain available in the light surface region, possibly supporting primary production. In a set-up with realistic spacing between turbine structures, stratification and depth, a single monopile is responsible for $1-3\%$ additional mixing to that of the bottom mixed layer, whereby approximately 10% of the turbulent kinetic energy generated by the pylon is used in mixing. Although the effect of a single turbine on stratification is relatively low, a rough estimate of relevant time scales suggest that the combined effect of multiple turbines could significantly affect the vertical structure of a weakly stratified water column.

5.2 Introduction

The reduction of greenhouse gas emissions through the advancement and promotion of renewable energy technologies is one of the strategies that have been adopted for the mitigation of anthropogenic climate change. The created legal frameworks, together with a series of governmental incentives, have facilitated the growth and development of offshore wind technology worldwide. Within the EU, a total of 15.8 GW have been installed and connected to the grid until December 2017, and the installation of an additional 10 GW has been planned (*Wind Europe et al.*, 2018). Among the relevant sea basins for the construction of offshore wind farms, the North Sea leads as the most important basin, with 71% of the total offshore wind capacity within the EU (*Wind Europe et al.*, 2018).

Advances in the offshore wind sector have allowed the construction of offshore wind farms (OWFs) in deeper areas of the coastal seas further away from the shores, where stronger winds are found. While in 2013 the mean depth of OWFs was 16 m, the mean depth reached 27.5 m in 2017 (*Corbetta et al.*, 2014; *Wind Europe et al.*, 2018), and therefore increasingly affect areas that undergo thermal stratification. This study focuses on the impact of offshore wind farm structures on turbulence and mixing of stratification, whereby the North Sea (German Bight) is used as the study region due to its relevance in the offshore wind energy sector.

5.2.1 Seasonal stratification and mixing by offshore wind farms

The German Bight is situated in a relatively shallow area of the North Sea with typical water depths between 20 – 50 m (Figure 5.1). In this region, thermal stratification often occurs during the summer months, whereas saline stratification is concentrated close to the coastal areas (*Huthnance*, 1991). Seasonal stratification in shelf seas is known to suppress vertical fluxes, controlling nutrient transport to the upper layer and therefore primary production. This has an influence on the storage and export of carbon dioxide through the shelf sea pump to a large extent (*Thomas et al.*, 2004; *Simpson and Sharples*, 2012). Quantifying stratification and how it is affected by different sources of mixing in shelf seas is therefore of major global and societal importance.

Shelf seas are often strongly influenced by tidal constituents, which, with the presence of OWF foundations in the water column, will repeatedly drive currents through the structures and potentially lead to enhanced turbulent mixing within their wake. Moreover, stirring by OWF foundations presents a mixing mechanism additional to the naturally-occurring processes acting upon the water column.

It remains largely unknown if OWF mixing is significant compared to natural variability in tidal shelf seas. There are a few analytical and numerical studies characterizing the hydrodynamic impacts of OWFs available in the literature (e.g. *Roulund et al.*, 2005; *Broström*, 2008; *Paskyabi and Fer*, 2012; *Ludewig*, 2015; *Grashorn and Stanev*, 2016). However, most studies focus on the wind wake and the resulting generation of up-/downwelling cells in the water column, or the wake generated in a neutrally stratified water column.

Rennau et al. (2012) have studied the influence of offshore wind farm structures on dense bottom currents in the Baltic Sea through the General Estuarine Transport Model (GETM, *Burchard and Bolding* (2002)) using the Reynolds–averaged Navier-Stokes (RANS) equations with the k-ε scheme. The grid used was circular and highly resolved within 3 cylinder diameters (D) and transformed to a rectangular shape within the next $3D$. The simulations with realistic wind farm set-up have found that OWF induced mixing was expected to be relatively low, decreasing the salinity at the bottom by 0.1 – 0.3 PSU, which is below natural variability (*Rennau et al.*, 2012). *Cazenave et al.* (2016) used an unstructured grid model to study single turbine foundations in the context of the shelf sea circulation, focusing mostly on the Irish Sea. The simulations included both well-mixed and stratified periods, and the grid resolution varied between 2.5 m and 20 m depending on the run and on the distance from the turbine foundation. The RANS equations are used to describe the turbulent flow, and turbulence closure is obtained through a k-ε scheme, modeled using the General Ocean Turbulence Model (GOTM, *Umlauf and Burchard* (2005)). With the modeled set-up, vertical mixing was enhanced by the foundations up to 200 m distance, and an OWF was found to possibly affect the stratification by 5 – 15% over an area nearly 80,000 times the area of the farm itself.

Whilst *Rennau et al.* (2012) and *Cazenave et al.* (2016) provided a first attempt to characterize OWF-induced mixing of stratification, shortcomings are present regarding the parameterization of turbulence through RANS, underlining the need of resolving the large, energy-containing eddies and parameterizing only the scales smaller than the diameter of a foundation.

Carpenter et al. (2016) conducted an idealized study to assess the large-scale impact of OWFs on stratification in tidal shelf seas. According to their study, a significant decrease in stratification in the North Sea could take place if a considerable portion of the shelf would be filled with OWFs, a possible scenario given current expansion plans of the wind energy sector. One of the caveats mentioned in *Carpenter et al.* (2016) addressed the lack of understanding of the interaction between turbulence production by OWF foundations and naturally-occurring turbulent processes, as well as the evolution of the thermocline in response of the additional OWF forcing.

Using the averaged estimates of power production by OWFs presented in *Carpenter et al.* (2016), *Schultze et al.* (2017) calculated the average dissipation rate of turbulent kinetic energy that can be expected from the OWF structures, $\langle \varepsilon_{OWF} \rangle$, and compared it with field observations of turbulence. The $\langle \varepsilon_{OWF} \rangle$ was estimated to be comparable to turbulence levels found in the thermocline. The power production by OWFs, and therefore also the dissipation rate of turbulent kinetic energy, were estimated assuming that a large section of the shelf would be covered with OWFs, and should be interpreted as average values over the entire section. In reality, production and dissipation of turbulent kinetic energy are expected to be largely concentrated in the wake of each structure. Furthermore, vertical mixing on the wake of the OWF foundations could be significantly enhanced, with possible consequences to the ecosystem (*Carpenter et al.*, 2016; *Schultze et al.*, 2017).

Towards this aim, *Floeter et al.* (2017) have assessed biophysical parameters in two OWFs in the North Sea while the water column was stratified. Empirical evidence of the doming of the thermocline caused by enhanced vertical mixing was found, predicting higher nutrient fluxes to the surface layer. Field observations that characterize the physical impact of OWFs are however rare, and it is especially challenging to discern the signal of the OWF from natural variability (*Floeter et al.*, 2017).

Given the increased interest in OWF technology and their potential to alter turbulence and mixing levels, we provide the first small-scale study of the thermally stratified wake to assess the importance of this additional turbulence source. The present study uses field observations and a large-eddy simulation model to assess turbulence and mixing induced by a turbine foundation. Although the amount of mixing generated by OWFs is expected to depend on the type of turbine foundation considered, the monopiles, which are vertical circular cylinders, are the most relevant within the EU, with a share of 87%. Therefore, this study focuses on the possible impact of a monopile on the mixing of a stratified water column. The present study is organized as follows: Section 5.3 gives an overview of the field campaigns and equipment used, with findings presented in Section 5.4. To compare the field observations with numerical modeling, and to gain more information about the stratified wake, large-eddy simulations are used. The large-eddy simulation model and the set-up of the simulations are briefly described in Section 5.5. The large-eddy simulations were set-up to resemble the conditions found in the field campaigns, of which results are presented in Section 5.6. A general discussion and the conclusions of this study are presented in Sections 5.7 and 5.8, respectively.

5.3 Overview of field campaigns and equipment

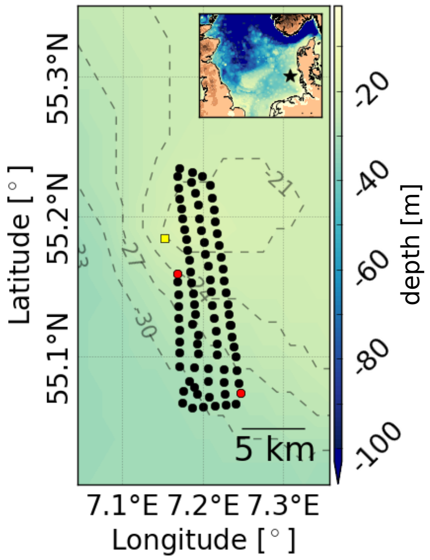

Figure 5.1: Illustration of the offshore wind farm DanTysk with single monopiles shown as black dots. The red dots mark the monopiles surveyed with the towed chain. The map on the top right corner of the figure shows the North Sea, and indicates the position of DanTysk through the black star. The colorbar depicts depth across the whole North Sea and the gray dashed contour lines detail depth in the exact study area. The position of the platform FINO3 is shown through the yellow square.

Field measurements in the OWF DanTysk were conducted in two different years, 2015 and 2017, during the summer stratified period in the German Bight of the North Sea. The OWF DanTysk is centered at 55.14°N and 7.20°E, and was primarily chosen because it is composed of monopiles, the turbine foundation of interest. A further advantage of DanTysk is the occurrence of vertical stratification, despite the fact that the water depth within the farm is relatively low, ranging from 20 – 30 m depth (Figure 5.1).

Before the surveys were conducted, tidal times, direction and height were analyzed and a single monopile was selected each day for the wake analysis. In 2015, the survey took place on May 25th between approximately 12:10 – 12:40 pm UTC, and the chosen monopile, hereafter MP1, was situated at 55.16°N and 7.17°E (Figure 5.1). Conversely, in 2017, the monopile at 55.07°N and 7.25°E was selected (MP2), and the survey was conducted on July 19th between 09:20 – 10:40 am UTC (Figure 5.1)

The wake of the monopile was surveyed using a chain of conductivity, temperature and depth (CTD) sensors that was towed from a Zodiac in 2015. Hereafter, the chain of CTD sensors is referred to as the towed chain. In 2015, the towed chain was composed of 6 sensors that were fixed $1-2$ m apart from each other and measured from 1.5 m to 8 m depth. In 2017, the wave heights reached over 2.5 m, such that deploying the Zodiac became unfeasible. Therefore, in 2017, the towed chain was attached to the RV Ludwig Prandl, which had its rear propeller switched off as it surveyed the monopile to avoid the contamination of the measurements. Similarly to 2015, 8 sensors were attached to the chain situated 1.5 m apart from each other, starting from 3.5 m to 14 m depth. On both campaigns, the CTD sensors used were manufactured by Sea & Sun Technology GmbH.

Additionally, we have used the temperature data measured by sensors available at the fixed platform FINO3, which is located in the vicinity of DanTysk (Figure 5.1). At FINO3, the water temperature is recorded at 3 different depths (-6 m, -12 m, -

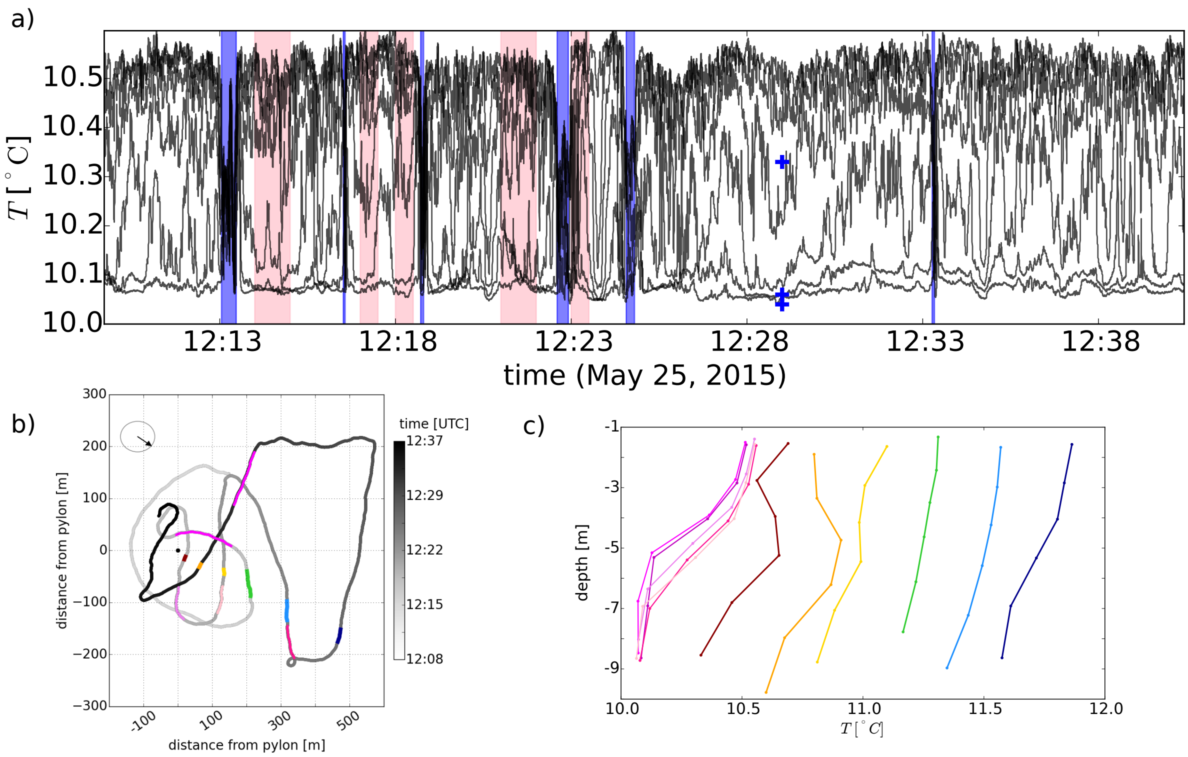

Figure 5.2: (a) Time series of the towed chain measurements in 2015. Each black line represents one CTD sensor. Areas in which the temperature measured by the sensors overlap are marked blue. Additional sections marked in pink have been selected to illustrate the background structure of temperature in the study area. The blue crosses show the temperature measured at platform FINO3 at -6 m, -12 m, and -18 m. (b) Measurement path of the towed chain measurements in 2015. The position of the blue sections marked in (a) are shown by the red, orange, yellow, green, blue and dark blue lines. The pink lines illustrate the location of the sections taken to demonstrate the background temperature stratification. The black arrow on the top left corner depicts the mean ocean current direction. (c) The water column within the wake of the monopile was considerably disturbed within a narrow area. Vertical profiles averaged over the sections marked in (b) are shown for the respective color-coded sections. The profiles in (c) have been intentionally offset by 0.25°C from each other for better visualization.

18 m). The temperature data is available at the FINO database (http://fino.bsh.de/), which is maintained by the German Maritime and Hydrographic Agency (Bundesamt für Seeschifffahrt und Hydrographie, BSH).

5.4 Assessment of the wake of monopiles with the towed chain

Weak stratification: The monopile surveyed in 2015 was situated in a shallow area at approximately -24 m that was nevertheless weakly stratified with 0.5°C between the sea surface and the bottom mixed layer, which started at about 10 m depth. At the time of the measurement, the tidal current direction and speed were 127° from the North and 0.3 m/s, respectively, and wind speeds were between 5 – 7 m/s at 10 m height.

Figure 5.2(a) shows the temperature measured by the different sensors fixed in the towed chain in time. The vertical separation of the lines shows the background temperature structure, where the temperature decreased with depth. The overlapping areas in which all sensors measured similar temperature are highlighted in blue and are considered as an indication of disruption of the background temperature structure. The same areas are identified if salinity or density estimates are considered (not shown). Further, the disturbed regions follow a coherent pattern that can be identified as the wake region downstream of the monopile, which is displayed in Figure 5.2(b-c) along with their respective vertical temperature profiles averaged over the wake region. For comparison, several additional regions were selected in Figure 5.2(a) to depict the original, background temperature structure of the water column during the measurement period (highlighted in pink). Similar to the wake regions, the location of the background temperature profiles is shown in Figure 5.2(b) along with their horizontally averaged vertical profiles in Figure 5.2(c) (pink areas and profiles).

The monopiles and OWF structures in general are expected to contribute to mix the water column by extracting energy from the flow and feeding it into turbulent motion. In our measurements in 2015, the disruption of background stratification by the wake is observed within a narrow region of up to 50 m width that reaches at least 500 m downstream of the monopile. Although no measurements were taken further downstream of the wake, the vertical profile obtained at approximately 500 m exhibits a stronger temperature gradient than the previous profiles between 200 m and 350 m. This could be an indication that the turbulence produced by the monopile has decayed sufficiently for restratification to occur. This is supported through the calculation of the potential energy anomaly $\phi = g \int (\rho - \rho_{\text{mix}}) z dz$, where z is the depth, ρ the density estimated at a given depth, and ρ_{mix} is the density of the mixed water column. To calculate ϕ based on the towed chain measurements, it was assumed that the density outside the measured depth range remained unchanged from the last data point. This assumption is supported by the data collected at the platform FINO3 (Figure 5.3). Within the wake of the monopile, ϕ decreased by up to 35% at 250 m, after which the strength of stratification increased again.

<u>Strong stratification:</u> Similar to 2015, the monopile selected for analysis in 2017 was situated on the upstream edge of the OWF at a 27 – 30 m depth region, though upstream of the wind farm. The temperature reached 17.2°C near the sea surface and decreased to 15.1°C until 18 m depth. Wind speeds were about 7 m/s and the ocean current direction and speed were 305° (clockwise rotation) from the North and 0.3 m/s, respectively. Despite having tracked the region of the monopile wake, no clear signal from the monopile could be identified that stood out from the naturally occurring variability (Figure 5.3). Other than in 2015, where the focus was laid up to about 500 m from the monopile, the analyzed region in 2017 extended over 1000 m downstream from the monopile with cross-sections that were approximately 200 m apart from each other. No clear influence of the monopile was observed in the cross-section at 400 m or at 200 m downstream, which is the closest that the measurements came to the monopile on that campaign (not shown).

The observations with the towed chain have provided evidence that the wake of single monopiles can be identified by field measurements, depending on the vertical structure of the water column. Further, the wake of the obstacle was found to be narrow, whereby its width increased with distance from the pylon itself. Under weak stratification, the disturbance of the vertical structure of the water column by the wake seemed to reach up to approximately 450 m downstream, after which restratification of the wake region

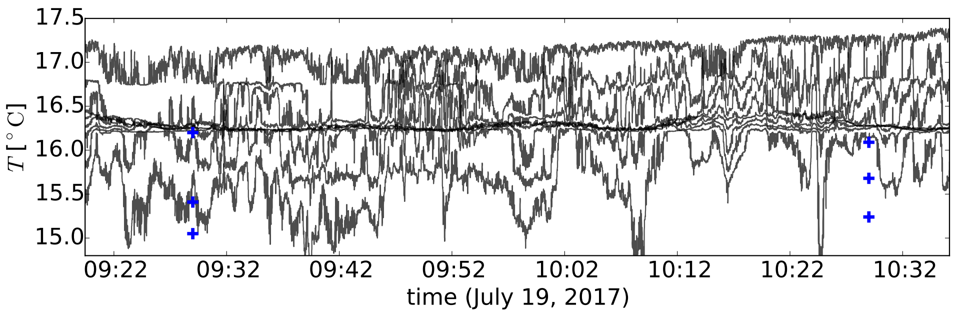

Figure 5.3: Time series of the towed chain measurements in 2017. Each black line denotes one CTD sensor. The blue crosses show the temperature measured at platform FINO3 at -6 m, -12 m, and -18 m at two different times.

began. Moreover, the towed chain raises questions that can be answered by high resolution numerical modeling, in which turbulence and mixing by the pylon can be isolated and quantified. Therefore, the next subsection describes our approach to analyze the flow downstream from a monopile using large-eddy simulations.

5.5 Large–eddy simulations

Analyzing the wake of a structure in the field is challenging due to difficulties in isolating the natural variability of the flow from the true signal of the structure. To complement the empirical evidence obtained through the towed chain measurements, we use large–eddy simulations (LES) to assess the wake of a monopile under different levels of stratification and therefore quantify turbulence and mixing by the pylons under different scenarios. Large–eddy simulations resolve the large, energy-containing eddies and filter the small eddies, which are parameterized by means of a subgrid-scale model. This allows the simulation of flows with high Reynold's numbers at grid resolutions on the order of 1 m, and therefore resolves the most important energetic scales of turbulence, which is not possible when using RANS models.

The LES model used is the Parallelized Large-Eddy Simulation Model for atmospheric and oceanic flows (PALM, version 4.0, revision 2504M), which has been developed at the Institute of Meteorology and Climatology of the Leibniz University of Hannover (*Raasch and Etling*, 1991, 1998). PALM is in continuous development, and its most recent thorough description can be found in *Maronga et al.* (2015).

PALM solves the non–hydrostatic, incompressible Navier–Stokes equations after the Boussinesq approximation. The parameterization of the subgrid-scales is performed after *Deardorff* (1980); *Moeng and Wyngaard* (1988); *Saiki et al.* (2000), and presuposes that the energy transported by small eddies is proportional to the respective gradients of the mean quantities. PALM uses a Cartesian Arakawa staggered C-grid (*Harlow and Welch*, 1965; *Arakawa and Lamb*, 1977) with equidistant spacing between the grid cells. The representation of the monopile, a circular cylinder, is therefore approximated in the simulations described below, whereby the resemblance to a real cylinder increases with the grid resolution. The following subsection describes the set-up used in the simulations, which has been defined based on a grid sensitivity analysis (cf. Section 5.9).

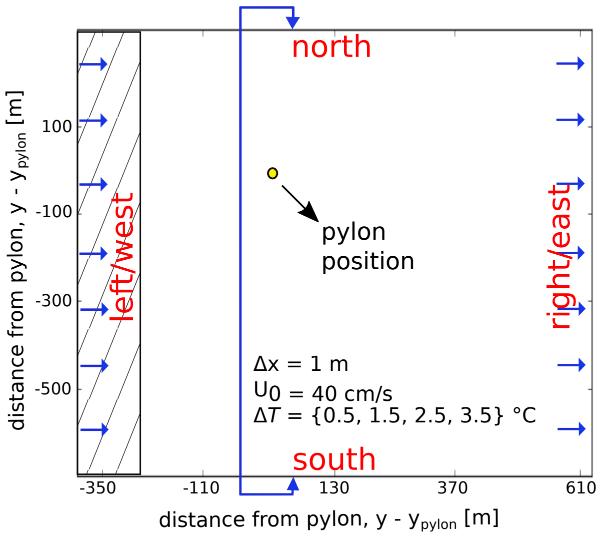

Figure 5.4: Sketch of the simulations ran in PALM for scientific analysis. The monopile, located at x_{pylon},y_{pylon}, is shown in yellow. The axis have been centered at the pylon location. The simulations were run using cyclic boundary conditions in the north and south boundaries, which is indicated by the blue arrow. West and east boundaries were non-periodic (inflow and outflow). The hatched pattern marks the turbulence recycling domain.

Simulation set-up

The domain size of all simulations used in scientific analysis was 1024 m $\times$ 1024 m $\times$ 32 m, with the grid size $\Delta x = 1$ m in all directions (Figure 5.4). The monopile was positioned at 512 m from the left boundary and at 750 m from the south boundary. At the sea surface, Neumann boundary conditions were used for all velocity components and scalar variables and the Dirichlet (no-slip) boundary condition was applied at the sea bed. Further, to be able to isolate the turbulence generated by the monopile from turbulence generated at the sea bed, separate identical simulations tackling solely the impact of bottom boundary layer turbulence (i.e. without the monopile) on stratification were performed.

The south and north boundaries of the domain were assigned periodic conditions and, to investigate the impact of a single monopile on stratification, non-periodic boundary conditions were applied along the main flow direction (left and right boundaries) for all velocity components and scalar variables (Figure 5.4). When using non-periodic boundary conditions, a turbulent inflow has to be defined to trigger bottom boundary layer turbulence generated by friction at the sea bed throughout the entire domain, such that the effect of the obstacle can be separated from other turbulence sources. A turbulent inflow is implemented in PALM through the "turbulence recycling method", in which a precursor simulation with periodic lateral boundary conditions is run until turbulence has developed and the set-up has reached a quasi steady-state (*Lund et al.*, 1998; *Kataoka and Mizuno*, 2002; *Maronga et al.*, 2015). Once the precursor run has reached a quasi steady-state, its output is used to stir the main run. If the domain size of the main run is greater than that of the precursor run, the output data of the latter is used to fill up the larger domain through cyclic repetition (*Maronga et al.*, 2015).
The domain size in the precursor simulations was 128 m $\times$ 512 m $\times$ 32 m, and the same

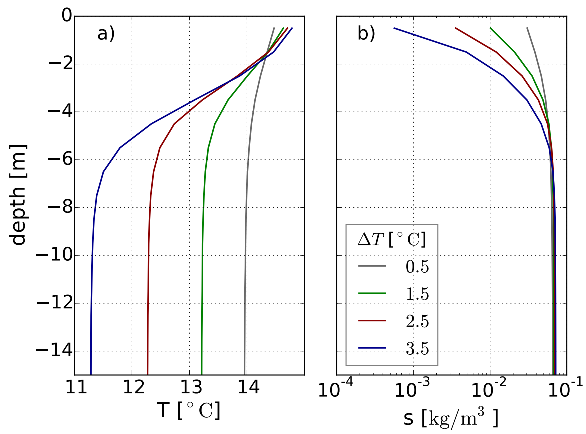

Figure 5.5: Initial vertical profiles of temperature (a) and passive scalar concentration (b) for the main simulations of the four stratification cases considered. No further changes in the profiles were observed below 15 m depth.

grid size, $\Delta x = 1$ m, as in the main run was used. A current velocity of 0.4 m/s was defined along the domain length, which corresponds to typical values found in the study region. Random disturbances up to 10^{-4}m/s were imposed within the bottom 5 m of the domain to trigger bottom boundary layer turbulence. No obstacle was added to the precursor run.

Four different scenarios of vertical stratification were analyzed in this study, all of which have been defined in the precursor runs by a temperature gradient, whereas salinity was kept constant at 33 PSU. The implementation of the stratification in all cases was given by a linear gradient of temperature, which was motivated by field measurements, i.e. (i) -1.5 °C/10 m; (ii) -2 °C/10 m; (iii) -3 °C/10 m and (iv) -4 °C/10 m, which started from the top of the domain and persisted until 10 m depth. To investigate the impact of a single structure of 7 m in diameter, D, on scalar suspension and advection, a passive scalar at a concentration of 6 kg/m^3 was added up to 2 m above the sea bed. The precursor simulation of each of the four cases was run until the quasi-steady state was reached, at what point some mixing and scalar suspension had inevitably already taken place. Therefore, the initial temperature and passive tracer profiles for the respective main runs differ from the initial conditions of the precursor runs, and are shown in Figure 5.5. Differences in initial passive scalar concentrations among cases (i) – (iv) are explained by the differences in stratification and therefore vertical fluxes across it.

Planetary rotation was included in the precursor and main simulations for 54 °N latitude to resemble conditions found in the German Bight of the North Sea. No additional heat, wind forcing or pressure gradient is applied to stir the simulations.

All main analyzed runs were carried out for approximately 10 hours simulation time. The quasi steady-state of the simulations was reached at approximately 2 hours and the remaining 8 hours were used in the calculation of the unavailable potential energy anomaly (ϕ), dissipation of turbulent kinetic energy (ε) and the bulk mixing efficiency (η), which are described in the following sections.

Table 5.1: Summary of the precursor and main simulations to investigate the wake of the monopile (MP) at a Reynolds number of $Re = U_0 D/\nu = 2.8 \times 10^6$, with ν the kinematic viscosity of sea water, and U_0 the characteristic flow velocity, $L_x/D = 146$, and $L_y/D = 146$. To stir the non-periodic simulations with a quasi-steady turbulent flow, precursor runs (PRE) have been set-up prior to the main runs (MAIN). The results from a precursor run are used as input in the main run. The salinity was kept constant at 33 PSU in all cases. In the precursor runs, the temperature and thus density gradients were generated from the sea surface until 10 m depth. Similarly, the passive scalar was added at the bottom 2 m of the domain at the concentration indicated below. Using the same results from the respective precursor run, identical main simulations without the obstacle have been conducted for each case (not listed). The respective Froude numbers $Fr = (\pi/2)U_0/Nb$ at the start of the precursor and main runs, where b is the thickness of the stratified region, are indicated in the table.

	Domain size [m × m × m]	Δx [m]	U_o [m/s]	ΔT [°C]	c [(kg/m^3)/m]	MP	Fr
Case i							
PRE	128 × 512× 32	1	0.4	-1.5	0.6	no	3.6
MAIN	1024 × 1024× 32	1	PRE	PRE	PRE	yes	7.4
Case ii							
PRE	128 × 512× 32	1	0.4	-2	0.6	no	3.2
MAIN	1024 × 1024× 32	1	PRE	PRE	PRE	yes	4.9
Case iii							
PRE	128 × 512× 32	1	0.4	-3	0.6	no	2.6
MAIN	1024 × 1024× 32	1	PRE	PRE	PRE	yes	3.5
Case iv							
PRE	128 × 512× 32	1	0.4	-4	0.6	no	2.3
MAIN	1024 × 1024× 32	1	PRE	PRE	PRE	yes	2.8

5.6 Qualitative analysis of a monopile wake in stratified regimes

The weakest (i) and strongest (iv) stratification cases are summarized in Figures 5.6 and 5.7, which depict the wake of the monopiles in the context of the velocity magnitude, relative vorticity, temperature and passive scalar concentration. Identical figures for the remaining stratified cases (ii) and (iii) have been included in the supplemental material (Section 5.9). Figures 5.6(a-b) and 5.7(a-b) have been centered with respect to the position of the monopile, which can be clearly identified along with its wake generated downstream. Figures 5.6(a) and 5.7(a) show the relative vorticity $\zeta = \partial v/\partial x - \partial u/\partial y$ at 0.5 m depth for simulations (i) and (iv), respectively. On both figures, it is seen that the tendency of a fluid particle to rotate is enhanced in the wake of the monopiles, with the rotation of the fluid particles inside and outside the wake being negatively influenced by the strength of stratification.

Time averaged horizontal cross-sections of temperature and scalar concentration at 0.5 m depth for cases (i) and (iv) are depicted in Figures 5.6(b) and 5.7(b). In all analyzed cases, the wake of the monopiles can be identified at the surface by a decrease in temperature and velocity magnitude, and an increase in relative vorticity and passive scalar concentration immediately behind the structure. The analyzed wakes were 50 – 100 m wide and the disturbances in the flow field, temperature and the passive tracer were observed until the end of the domain at 600 m past the monopile. Even though the wake signature reaches up until the end of the domain, the extent of the strongest departures in temperature and scalar concentration generated by the monopile at the surface are found to decrease with increasing stratification (cf. Figures 5.6(b) and 5.7(b)). Moreover, the greater the temperature gradient, the stronger the forcing towards the re-stabilization of the flow, which limits the range of influence of the wake downstream. This can also be observed in Figures 5.7(c-f) and 5.6(c-f), where vertical cross-sections of temperature from the simulations are shown. Upstream of the monopile, the water column is being stirred by bottom boundary layer turbulence and the temperature gradient reaches from the sea surface up to 8 – 10 m depth. As the flow passes by the structure, the water column is further disturbed and vertical motion is enhanced in a narrow region of the domain. These qualitative observations are further analyzed in the next subsections, in which the change in stratification and mixing caused by single monopile structures, as well as the dissipation of turbulent kinetic energy, are quantified.

5.6.1 Turbulent mixing by wakes

The unavailable potential energy anomaly (ϕ) was calculated for each yz-cross-section corresponding to every grid point in the x-direction as

$$\phi = \frac{g}{L_z} \int [\langle\rho\rangle - \rho(z^*)] z^* dz^*, \text{with} \tag{28}$$

$$\langle\rho\rangle = \frac{1}{L_z} \int \rho(z^*) dz^*. \tag{29}$$

Through ϕ, the change in stratification along the domain in flow direction could be quantified for each of the simulations. The 3D density cross-sections of dimensions $\Delta x \times L_y \times L_z$ are each reordered and sorted into a vector $\rho(z^*)$, where z^* is the depth vector that ranges from 0 to L_z, L_z is the total depth of the water column, and L_y is the width of the cross-section (*Winters et al.*, 1995; *Caulfield and Peltier*, 2000; *Burchard and Hofmeister*, 2008).

Figure 5.8(a) depicts the loss of stratification attributed to mixing by bottom boundary layer turbulence only (semi-transparent lines) and with the addition of the monopile (colored lines). The change in unavailable potential energy in the simulations without the monopile is explained by turbulence generated by bottom boundary layer friction. In the simulations with the structure, vertical mixing before the monopile is due to bottom boundary layer turbulence, which is intensified by 1 – 3% at the monopile location and downstream, as shown in Figure 5.8(a) by the enhanced drop in ϕ after the monopile.

After calculating the change of unavailable potential energy, the gradual mixing of the water column in time-space can be quantified by $m = U_{yz} d\phi/dx$, with U_{yz} the mean velocity of the respective yz-cross-section, and the total mixing within the domain is obtained through integration $M = \int m dx$. The total mixing promoted by the monopile M_{OWF} is then calculated by subtracting the value of the simulations without the foundation structure M_{BBL} from the total mixing including the monopile effects $M_{\mathrm{OWF}} = M_{\mathrm{TOPO}} - M_{\mathrm{BBL}}$. For all analyzed cases, the total mixing generated by one monopile is estimated to be 7 – 10% that of the mixing induced by bottom boundary layer turbulence, and is confined to the near field of the monopile.

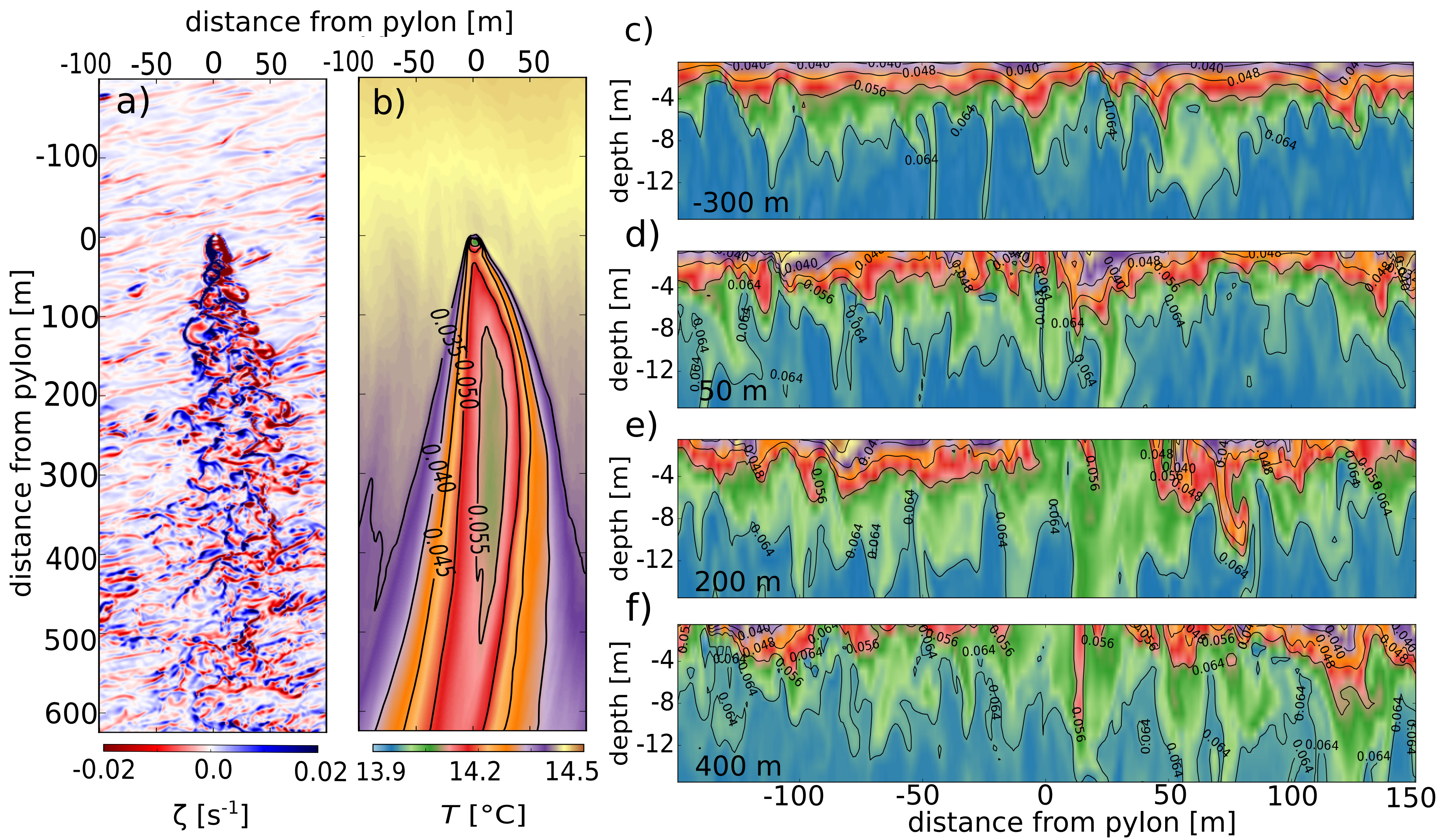

Figure 5.6: Summary of the simulation results for case (i) with $\Delta\ T \approx 0.5°C$. (a) Horizontal instantaneous cross-section of relative vorticity ζ at 0.5 m depth. (b) Horizontal cross-section of temperature at 0.5 m depth averaged over 5000 s. The black contours illustrate the enhanced passive scalar concentrations in the wake of the monopile. (c)-(f) Vertical cross-sections of temperature perpendicular to initial flow direction. Similar to (b), the black contours represent the scalar concentration. The horizontal axis has been centered to the monopile location, with the current traveling from (c) to (f). The vertical axis has been restricted to the first 15 m from sea surface for a more detailed visualization. Identical figures depicting the whole vertical extent are provided in the supplemental material. The different panels stand for a specific distance from the structure, which is shown in the bottom left corner. Negative numbers stand for regions before the monopile, positive numbers for cross-sections downstream.

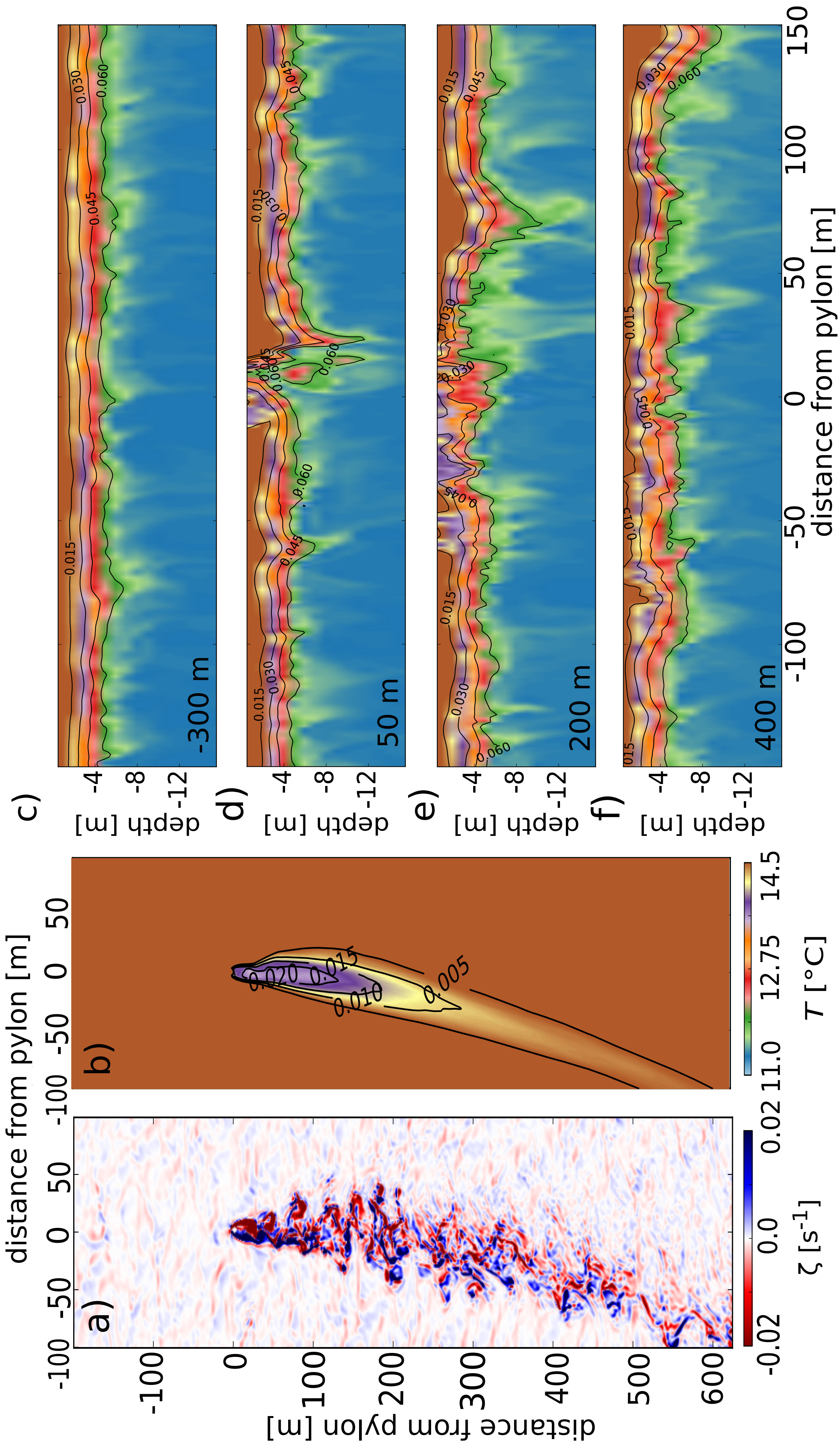

Figure 5.7: Same as Figure 5.7, but for the simulation results of case (iv) with $\Delta T \approx 3.5°C$.

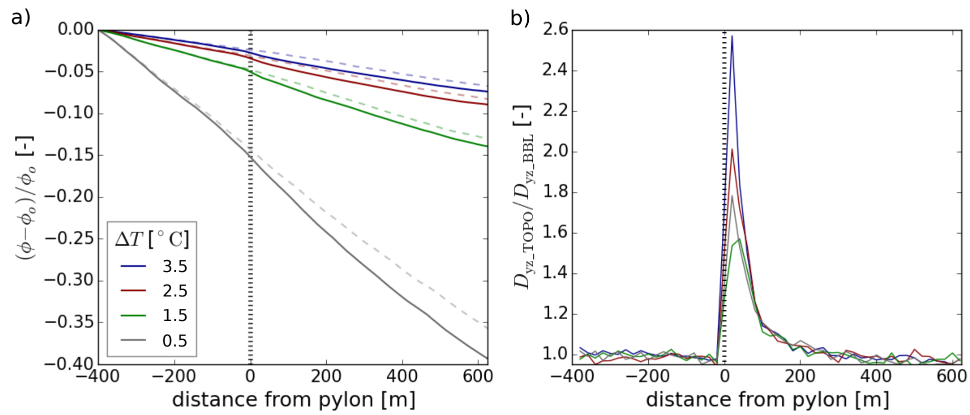

Figure 5.8: Change in unavailable potential energy (a) and total dissipation $D_{\mathrm{yz\_TOPO}}/D_{\mathrm{yz\_BBL}}$ (b) for cases (i) – (iv) along the domain length (x-axis), which has been centered with respect to the position of the monopile. In (a), solid lines depict results of simulations with the pylon, whereas dashed lines show the change in unavailable potential energy for the simulations without the structure. The color code in (b) is the same as in (a), however each line stand for the ratio $D_{\mathrm{yz\_TOPO}}/D_{\mathrm{yz\_BBL}}$ of a given case.

5.6.2 Dissipation of turbulent kinetic energy

We now estimate the dissipation of turbulent kinetic energy from the simulation results to better understand the mixing promoted by the OWF structures. The subgrid-scale dissipation of turbulent kinetic energy, ϵ, returned by the LES model gives a general impression about the order of magnitude of turbulence downstream from the obstacle.

However, the subgrid-scale (SGS) dissipation ϵ has been shown to underestimate the absolute value of the true dissipation of turbulent kinetic energy ε as a consequence of numerical dissipation of the advection scheme (*Maronga et al.*, 2013). To obtain the true dissipation of turbulent kinetic energy ε, we use the method described by *Tennekes and Lumley* (1973) and *Maronga et al.* (2013), which is based on the assumption of isotropy. The dissipation ε is thus estimated through the calculation of power spectra for a velocity component u_i:

$$S_{u_i}(k) = \alpha\varepsilon^{2/3}k^{-5/3}, \tag{30}$$

with the constant $\alpha \approx 0.52$, and u_i as one of the horizontal velocity components on a Cartesian coordinate. The simulations in *Maronga et al.* (2013) were horizontally homogeneous, which enabled the calculation of power spectra for each depth level using all data points available at each vertical grid point. As a result, a vertical profile of ε was obtained. The presence of a monopile in our simulations generates anisotropic flow downstream and the calculation of spectra based on data points collected horizontally is invalid. Therefore, to obtain ε, a time series of single grid points is collected instead, from which a power spectrum in the spatial domain is generated under the assumption of Taylor's hypothesis of frozen turbulence. Similar to *Maronga et al.* (2013), the dissipation ε was calculated if an inertial subrange could be identified in the spectrum, and if the variance within the inertial subrange was below 50%. The ε estimates obtained from the spectra compared well with the SGS ϵ, although the agreement between both methods improved away from the boundaries where the eddies are not influenced by them (cf. supplemental material). This was expected as the size of the eddies is decreased close to

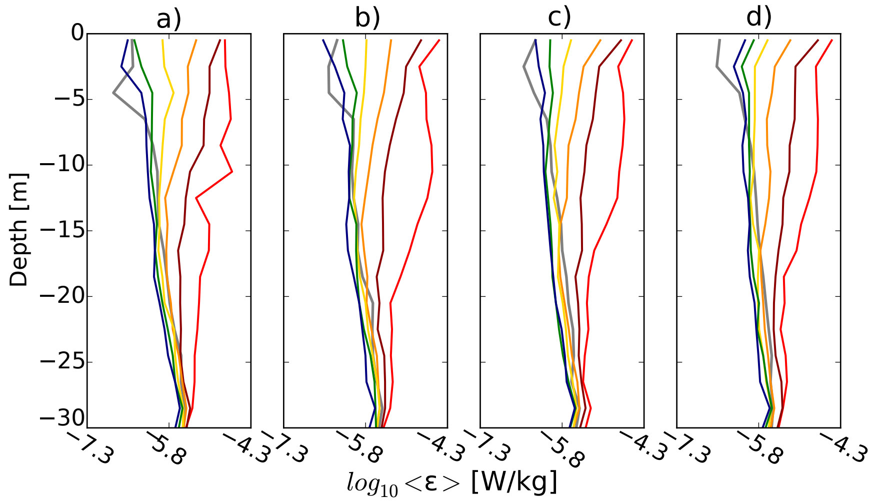

Figure 5.9: Vertical profiles of the dissipation of turbulent kinetic energy ε averaged within the wake of the monopile. Different colors stand for a given distance from the monopile. The colors red, dark red, dark orange, yellow, green and blue depict profiles that are situated 60 m, 100 m, 160 m, 260 m, 360 m, 460 m downstream the monopile, respectively. The gray profile depicts ε without the influence of the structure.

the boundaries and the performance of the subgrid-scale model drops (*Maronga et al.*, 2013; *Gibbs et al.*, 2016).

Vertical profiles of ε averaged within the wake of the monopile in the different case studies are shown in Figure 5.9, with the gray line representing the dissipation of turbulent kinetic energy estimated in the simulations without the monopile. The high $\langle\varepsilon\rangle$ ($O(10^{-6}$ W/kg)) found in the bottom boundary layer is caused by friction at the sea bed, and is comparable to that observed in field measurements at similar current magnitude (cf. Figures 4.2 and 4.7 in Section 4). In all analyzed cases, ε was the highest in close proximity to the monopile, with the turbulence in the upper 10 m exceeding that of background levels by over an order of magnitude.

The total dissipation of turbulent kinetic energy attributed to the monopiles (D_{OWF}) can be estimated by subtracting the total ε of the simulations without the monopile D_{BBL} from those with it ($D_{\mathrm{OWF}} = D_{\mathrm{TOPO}} - D_{\mathrm{BBL}}$), where $D = (\rho_o/A_{\mathrm{yz}}) \int \varepsilon dV$, and A_{yz} is the cross-sectional area of each slice along the domain length. For the analyzed simulation set-ups, a single monopile is expected to increase the total dissipation of turbulent kinetic energy by $4-9\,\%$ compared to a natural environment without the structure. Additionally, the total dissipation of each slice along the domain length D_{yz} demonstrates that the increase in total dissipation is concentrated within the first $200-300$ m past the monopile, after which $D_{\mathrm{yz\_TOPO}}$ and $\langle\varepsilon\rangle$ itself are comparable to background levels $D_{\mathrm{yz\_BBL}}$ (Figures 5.8(b) and 5.9).

5.7 Discussion

5.7.1 Mixing by monopiles

The towed chain measurements have shown that structure of temperature in the wake of a monopile is significantly disturbed under weak stratification ($\Delta T \sim 0.5$ °C), which could be verified in the large-eddy simulations (case (i), Figure 5.6). The impact of a turbine structure under stronger stratification is however less pronounced, which can be explained by the magnitude of the temperature anomalies generated by a monopile. Moreover, whilst a temperature anomaly of 0.2 °C is clearly visible under weak stratification of $\Delta T \sim 0.5$ °C, in cases with a stronger temperature gradient, e.g. $\Delta T \sim 1.5$ °C, such temperature anomaly could be masked by other mixing mechanisms.

Despite the elevated turbulence levels generated by single turbines, the amount of mixing obtained is relatively low compared to BBL mixing, with the total change in unavailable potential energy by monopiles between $1-3\%$ at a realistic pylon spacing. This suggests that most of the generated turbulence is acting upon already mixed fluid. With the total amount of mixing and turbulence attributed to a monopile, the bulk mixing efficiency can be calculated as $\eta = M_{\mathrm{OWF}}/(M_{\mathrm{OWF}} + D_{\mathrm{OWF}})$. The bulk η is a modified measure of the empirically defined mixing efficiency $\gamma = R_f/(1 - R_f) \approx 0.2$, where $R_f = -\mathcal{B}/\mathcal{P} = -\mathcal{B}/(-\mathcal{B}+\varepsilon)$ with $\mathcal{B}$ the buoyancy flux and $\mathcal{P}$ the shear production of turbulent kinetic energy, which is used for purely stratified shear flows (*Osborn*, 1980; *Gregg et al.*, 2012; *Cyr et al.*, 2015). The bulk mixing efficiency η is estimated to be approximately 0.1 for the four studied cases and is therefore slightly smaller than $\gamma \approx 0.2$. This seems reasonable considering that the pylon is not only acting upon stratified fluid, and therefore its mixing efficiency is expected to be smaller than the usual γ.

Carpenter et al. (2016) has provided estimates of the power removed from the flow in the German Bight of the North Sea assuming that its complete area would be filled with by equidistant monopiles, $P_{\mathrm{str-NS}}$. The calculations were based accounting for mean tidal current velocities and realistic spacing between single turbines, and have estimated that $P_{\mathrm{str-NS}} \approx 6 - 10$ mW/m^2 for a drag coefficient $C_D = 1$, which is comparable to the $C_D = 0.7$ of the monopile in our simulations (cf. Section 5.9). Using our estimates of the mixing efficiency η by a monopile and P_{str-NS}, the mixing rate accounting for the tidal motion can be obtained by $m_{\mathrm{NS}} = -\eta P_{\mathrm{str-NS}}$. Further, assuming large farms with equally spaced turbines while disregarding non-linear interactions among structures, and neglecting additional sources of heat or mixing, the approximate time needed to entirely mix the water column for the two cases with weaker stratification (i and ii) would be $t_{\mathrm{mix}} = -\phi_o/m_{\mathrm{NS}} \sim 2-7$ days, depending on $P_{\mathrm{str-NS}}$ and the stratification ($\Delta T = 0.5 - 1.5$ °C). This time scale is comparable to the advection time of drifters through a wind farm, which has been observed to be approximately 7 – 10 days in the German Bight (*Carpenter et al.*, 2016; *Floeter et al.*, 2017). Thus, whilst the effect of a single foundation on stratification is relatively small, with $< 5\%$ additional mixing, the contribution of an entire wind farm to mixing could be significant under weak stratification. Under stronger stratification ($\Delta T > 2.5$ °C, or $\Delta\rho > 0.6$ kg/m^3), as in cases (iii) and (iv), time scale of mixing was 8 – 20 days and could become important in the context of a whole farm, even though complete mixing is not necessarily expected.

5.7.2 Scalar transport on the wake of the monopiles

A passive scalar c was added to the simulations to analyze possible nutrient pathways and their supply to the surface layer. The initial concentration of c in the precursor run in all simulations was 0.6 (kg/m^3)/m in the bottom 2 m, whereas the rest of the domain was started free of the passive scalar. This initial profile was chosen to simulate a nutrient rich bottom layer in contrast to the sea surface, which has been observed to be nutrient-limited during the summer months in shelf seas as a result of stratification (*Sharples*

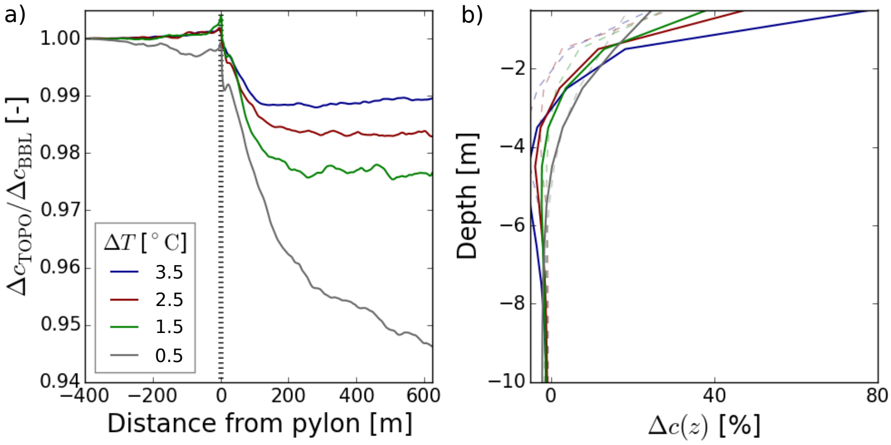

Figure 5.10: (a) Relative change in the concentration of passive scalar between the upper and the bottom 2.5 m in the vertical axis along the domain length for the simulations with the monopile Δc_{TOPO} and those without it Δc_{BBL}. (b) Average change in scalar concentration along the domain length with depth. The x-axis in (a) has been centered to the pylon position. In (b), solid lines represent the simulations with the pylon, whereas dashed lines show the change in scalar concentration due to bottom boundary layer turbulence.

et al., 2001; *Ross and Sharples*, 2007).

Due to differences in stratification intensity and therefore stability, c was distributed differently in the water column among the different simulations (Figure 5.5). Figure 5.10(b) shows horizontally averaged vertical profiles of the percentage change in scalar concentration in the simulations with and without the obstacle. The monopile has increased the c concentration in the upper 2.5 m on average by 3 – 25% from the weakest to the strongest stratification case. The turbulence generated by the monopile decreased the gradient of the concentration of passive scalar between the bottom layer (last 2.5 m) and the surface (upper 2.5 m) only slightly along the domain length, whereby the strongest exchange took place within the first 100 – 200 m downstream (Figure 5.10(a)).

The elevated levels of c remained concentrated in the narrow region of the wake, up to the end of the simulated domain (Figures 5.6, 5.7 and 5.13 – 5.16), and the strongest scalar input into the surface was observed within 100 m downstream the structure. Considering that the mixing by one monopile does not destroy the temperature stratification, the passive scalar is expected to remain available within the temperature gradient and spread out within the surface region. The enhanced concentration of the passive scalar to the upper layer suggests that also nutrients from the bottom would be increasingly supplied to the light-rich surface, which could support primary production. It is however outside the scope of this study to estimate possible biological effects of the monopiles on biological productivity.

5.7.3 Considerations

The conducted simulations provided simplified case studies of monopile-induced mixing, in which sources of stabilization of the water column, e.g. heat influx, and other mixing mechanisms, e.g. wind forcing and wave breaking, have been neglected. Further, our analysis is based on steady-state simulations with a constant in- and outflow, thus tidal effects are yet to be evaluated. Therefore, future studies could extend the analysis by including further parameters to the problem and assessing how the mixing by the foundation structures is modified.

By studying the impact of a single monopile, non-linear effects of interacting wakes from different structures have been disregarded in the estimates of large-scale mixing, which should be regarded as a rough estimate for the analyzed foundation type. Non-linear effects from wake interaction as well as other foundation types, e.g. tripiles or jackets, are more complex cases and expected to generate more mixing than single monopiles.

The addition of a passive scalar to the simulation was a first step towards a better understanding of nutrient pathways in the wake of offshore wind farm structures. Future work could concentrate on the evaluation of possible chemical and biological effects of the enhanced mixing and scalar influx to the stratified region.

The scenarios analyzed in this study were composed of a bottom mixed layer that reached up until 20 m from the sea bed, where temperature stratification took over and was extended until the sea surface. This set-up was chosen to enable the comparison between the field observations presented. It is known however that stratification in shelf seas is often characterized by a surface and a bottom mixed layer, which are separated by a stratified region known as the thermocline (*Ross and Sharples*, 2007; *Palmer et al.*, 2008; *Schultze et al.*, 2017). Future studies could focus on understanding this three layer system and how it is affected by the offshore wind farm foundations.

5.8 Conclusions

Offshore wind farms have been increasingly installed in shelf sea regions in which density gradients develop. The foundation structures generate additional turbulence in the water column and are therefore an additional, anthropogenic, source of mixing. Little is known about the small-scale physical effects of such structures on the natural state, and their possible further reaching implications for primary productivity has yet to be investigated. The present study provided for the first time observational and numerical evidence of monopile induced mixing from a small-scale perspective in a thermally stratified water column. A chain of CTDs towed by a vessel circulated around an offshore wind farm pylon to gain insight on its effect on the stratified structure of the water column. Large-eddy simulations replicating the initial conditions found in the field campaigns were conducted for comparison, with a closer analysis of the wake itself and its effect on turbulence and mixing made possible. From the foundation structures of offshore wind farms available, the monopiles have been chosen due to their broad use and application area as this type of foundation can be installed in deeper regions that become seasonally stratified.

During the field observations in 2015 (weak stratification), a decrease in stratification within the wake of the pylon was observed and reached up to 35% at approximately 250 m downstream, after which restratification took place. Further, in an LES scenario with realistic spacing between OFW structures, a similar decrease in the strength of stratification within the wake was observed. However, the mixing promoted by a monopile alone within a 600 m range was found to be around 10% of that triggered by bottom boundary layer turbulence. The wake of this type of structure is characterized by a narrow region of strong turbulence within the first $50 - 100$ m downstream, with the dissipation of turbulent kinetic energy being one order of magnitude higher than the background.

The elevated turbulence levels dissipate within 300 m past the monopile, after which ε becomes comparable to background levels. The addition of a passive scalar to the bottom mixed layer has provided valuable insight on the intensity at which scalars are upwelled into the stratified region in the wake of the structure.

The region with the sharpest decrease of potential energy matches with the turbulence signal, and the overall mixing efficiency lies between $8 - 14\%$. The time interval estimated for the complete mixing of the water column under weak stratification was estimated to be below 10 days, which is comparable to the advection time of particles through an offshore wind farm in its current length (8 km). Therefore, whilst one monopile has shown to have little effect in decreasing stratification in its surroundings, the effect of an entire farm could be significant. Under stronger stratification, the impact of offshore wind farm structures on mixing is less pronounced and a fully mixed water column is not expected. Future work could focus on (1) complementing the present simulations with further forcing mechanisms such as wind and tidal effects, (2) analyzing the interaction of the wake of neighboring structures, (3) assessing the impact of other foundation types (e.g. jackets) on turbulence and mixing, and (4) studying possible effects of enhanced scalar fluxes on primary productivity and biological activity in general.

Acknowledgements

This project was conducted within the Polar Regions and Coasts in the Changing Earth System II program (PACES II) funded by the Helmholtz Foundation, which we gratefully acknowledge. The authors would like to thank the support of J. Horstmann, R. Kopetzky, M. Heineke, B. Peters, T. Kock, the captain and the crew of the research vessel (RV) Ludwig Prandtl and the RV Heincke during the towed chain measurements. The RV Heincke ship time was provided through the grant AWI_HE445_00. We gratefully acknowledge the German Federal Ministry of Economic Affairs and Energy (BMWi) and the Project Management Jülich (PTJ), which provided access to the temperature measurements of the platform Fino 3. The temperature data is published in the Fino database under http://fino.bsh.de. We would like to thank the PALM group at the Leibniz Univertität Hannover, especially Björn Maronga and Matthias Sühring, for their support with the PALM model.

5.9 Supplemental Information

Grid sensitivity analysis

Prior to the main simulations used in the quantification of turbulence and mixing by a monopile, a grid sensitivity analysis was performed. For this analysis, a model domain of 512 m length, 256 m width and 32 m depth was chosen and a square column of 6 m width and 32 m height was placed at 300 m from the left boundary and 128 m from the south boundary. A square column was chosen instead of a cylindric one for simplicity, assuring that the volume of the structure remained unchanged despite varying grid resolution. Three different grid sizes were used in this analysis, $\Delta x = \{2, 1, 0.5\}$m, whereby the grid size was kept equal in all directions. A constant temperature gradient of $3.5°C/10$ m was added from the top of the domain until 10 m depth and the salinity was kept homogeneous at 33 PSU. The turbulent inflow is generated by means of a precursor run with periodic lateral boundary conditions, dimensions of 128 m $\times$ 128 m $\times$ 32 m, and

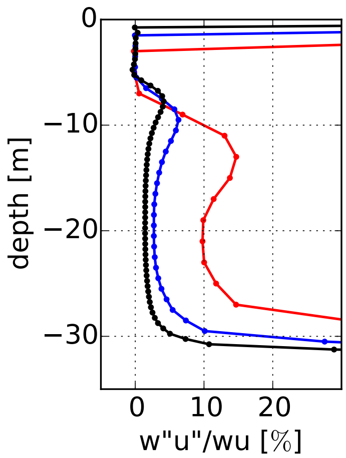

Figure 5.11: Horizontally and temporally averaged vertical profiles of the share of the subgrid-scale vertical momentum flux $w''u''$ in the total fluxes wu for the 2 m- (red), 1 m- (blue) and 0.5 m-simulations (black). The variables have been averaged over a 10,000 s interval after the simulations had reached a quasi steady-state.

the same grid size as in the main run. The boundary conditions and initial flow velocity were identical to the simulations described in Chapter 5.5.

To determine an appropriate grid size, our first step is to verify whether each of the simulations at different grid resolutions fulfill the basic requirement of a large-eddy simulation, in which the total momentum flux (wu,wv) is dominated by the resolved scales (w^*u^*, w^*v^*). Figure 5.11 shows profiles of the percentage of wu that is in account of the sub-grid scale vertical momentum flux ($w''u''$). The profiles depicted in Figure 5.11 have been averaged horizontally upstream the obstacle and temporally over 10,000 s. As expected, the percentage of the total fluxes that is parameterized decreases with grid size, and the 2 m-resolution exhibits the worst performance. Except at the boundaries, where the subgrid-scale parameterization is used, the share of the unresolved scales is below 10% in all simulations, thus indicating that the largest portion of the total flux is being resolved in the tested grid sizes.

The second step is to compare the velocity anomaly $U-U_0$, with $U=(u_i^2+u_j^2+u_k^2)^{1/2}$ and the initial velocity magnitude U_0, observed in all three grids. The simulations with $\Delta x=\{1,0.5\}$m show similar wake characteristics, with a width of approximately 10 m immediately behind the obstacle that is widened downstream up to about 80 m at the end of the domain (250 m distance, not shown). The wake in the 2 m resolution simulation is narrower and less resolved in the vicinity of the obstacle, especially until 150 m downstream. In the higher resolution simulations, the strongest negative velocity anomaly is concentrated up to 50 m behind the structure, and quickly decays with distance.

In the third and last step, the effect of the grid resolution on turbulence and mixing can be analyzed by means of the calculation of the total dissipation of turbulent kinetic energy D and of the total change in unavailable potential energy along the domain length (cf. *Winters et al.*, 1995; *Cazenave et al.*, 2016), where the latter essentially indicates a change in stratification due to mixing by the obstacle and bottom boundary layer turbulence. To quantify the stratification strength and its change along the domain length, we calculate ϕ [J/m^3], the unavailable potential energy anomaly (cf. Chapter 5.8), with the 3D domain separated into yz-cross-sections for each grid point along the domain length. The decrease in stratification observed in the analyzed grid sizes was similar, with a total decrease in ϕ of $6-7$ % along the domain length.

The total dissipation of turbulent kinetic energy and mixing efficiency are calculated as described in Chapter 5.6.2. For the coarse ($\Delta x = 2$ m), medium-sized ($\Delta x = 1$ m) and fine ($\Delta x = 0.5$ m) grid resolutions, D estimates were 0.8, 1.7, and 2.0, respectively. Whilst the total amount of dissipation still increases with grid resolution, the D obtained from the medium-sized grid is comparable to the fine resolution, such that the mixing efficiency η between both grids varies between $0.10 - 0.15$. Whilst the $\Delta x = \{1, 0.5\}$m simulations show similar results, the low resolution simulation might overestimate the impact of the OWF significantly through an unrealistically high mixing efficiency of 0.25.

Finally, both the medium sized grid and the fine grid show comparable results in all steps, and could be used for scientific analysis. Moreover, the calculation of the drag coefficient of the monopile in our simulations at $\Delta x = \{1, 0.5\}$m has shown that both grid sizes present a similar drag of 0.7, which is comparable to laboratory and numerical experiments (see below and *ESDU* (1985); *Schlichting and Gersten* (2000)). Given the similarity of results obtained at the fine and medium sized grids, the latter ($\Delta x = 1$ m) has been selected to be used in scientific analysis.

Calculation of the drag coefficient

The flow past a circular cylinder has been frequently studied by means of experimental and numerical analysis of the drag coefficient (*Eça et al.*, 2014). The drag coefficient is a dimensionless number used to express the resistance of an obstacle within a flow volume and is defined by $C_D = 2F_D/(\rho_0 U_0^2 A)$, with F_D the drag force, A the frontal area of the obstacle, U_0 the flow velocity in free stream and ρ_0 a reference density. For a cylinder, the frontal area is calculated by multiplying the monopile diameter D by its length. The drag coefficient of an obstacle is known to vary with the Reynolds Number $Re = U_0 D/\nu$, a ratio of the inertial to the viscous forces acting on the flow with ν the kinematic viscosity of sea water. This relationship can be used to evaluate how the approximation of a circular cylinder within the quadratic grid used in PALM compares to typical values.

For this purpose, a neutrally stratified, non-rotating domain of length 256 m, width 128 m and depth 128 m is considered, with a grid resolution of 0.5 m and 1 m. A structure with 7 m diameter is placed at 128 m and 64 m from the left boundaries, respectively, and its height is equivalent to the depth of the domain (128 m). Non-periodic boundary conditions for all velocity components are used at the inflow and outflow (Figure 5.12), and a homogeneous inflow current of 0.4 m/s is defined. This yields a Reynolds number of $Re = 2.8 \times 10^6$, which is representative for all simulations used in scientific analysis in this study. At the sea surface, i.e. the top boundary of the domain, Neumann boundary conditions are applied for velocity and scalars, whereas at the bottom of the domain, the Dirichlet conditions are used due to model constrains. To eliminate possible effects of bottom boundary layer turbulence in the calculation of the drag force, only the upper half of the vertical axis (64 m) is considered in the calculations, eliminating the effect of the bottom boundary layer.

Using the principles of mass and momentum conservation, the drag force can be estimated by calculating the momentum balance through the following equations:

$$F_D = \iint_{\mathrm{IN}} \rho_o U^2 dydz - U_0 \iint_{\mathrm{LAT}} \rho_o U dydz - \iint_{\mathrm{OUT}} \rho_o U^2 dydz \tag{31}$$

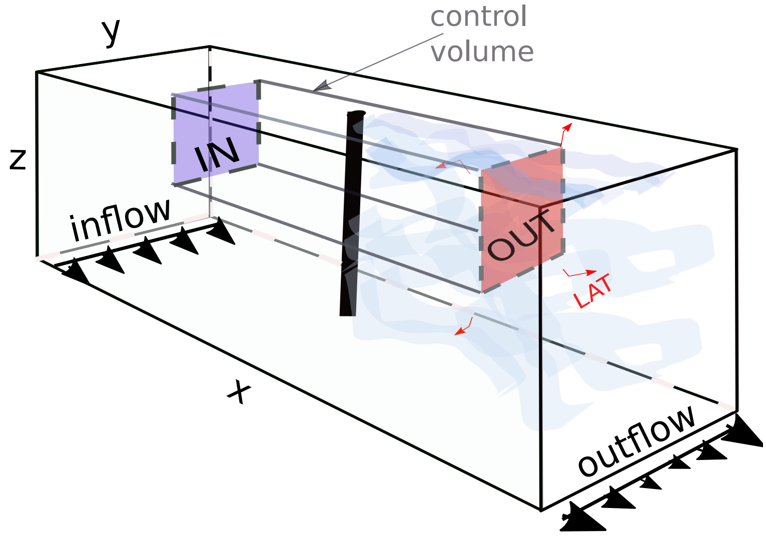

Figure 5.12: Sketch of the simulation and control volume used in the calculation of the drag coefficient. The control volume was selected such that the north and south boundaries reached the free stream region. The red surface in the control volume is within the wake of the monopile whereas the blue surface of the control volume stands for the undisturbed flow. Inflow (IN), outflow (OUT) and lateral (LAT) boundaries of a control volume are illustrated.

$$\iint_{\mathrm{LAT}} \rho_o U dydz = \iint_{\mathrm{IN}} \rho_o U dydz - \iint_{\mathrm{OUT}} \rho_o U dydz, \tag{32}$$

with $\rho_o = 1025$ kg/m^3 the reference density and the total velocity U, with the subscripts (IN, OUT, LAT) referencing the plane considered in Figure 5.12. Moreover, the mass flux in the lateral boundaries can be quantified by the difference between the mass flow in the inflow and outflow in a defined control volume (Figure 5.12).

The cylinder in the simulations with $Re = 2.8 \times 10^6$ has a drag coefficient of $C_D = 0.7$. Considering that the realization of the cylinder in the simulations herein is an approximated form, the calculated drag coefficient is considered reasonable compared to experimentally defined values $C_D \sim 0.6 - 0.7$ (*ESDU*, 1985; *Schlichting and Gersten*, 2000) and the spread obtained from different numerical simulations $C_D \sim 0.2 - 0.6$ (*Eça et al.*, 2014) for smooth cylinders at this Re. Given that monopiles in the field often become biofouled (*Petersen and Malm*, 2006; *Baeye and Fettweis*, 2015) and therefore possibly exhibit a higher drag coefficient than that of smooth circular cylinders, our approximation of a monopile is expected to be representative.

Summary figures of the simulations with a stratified regime and a monopile : Case (i)

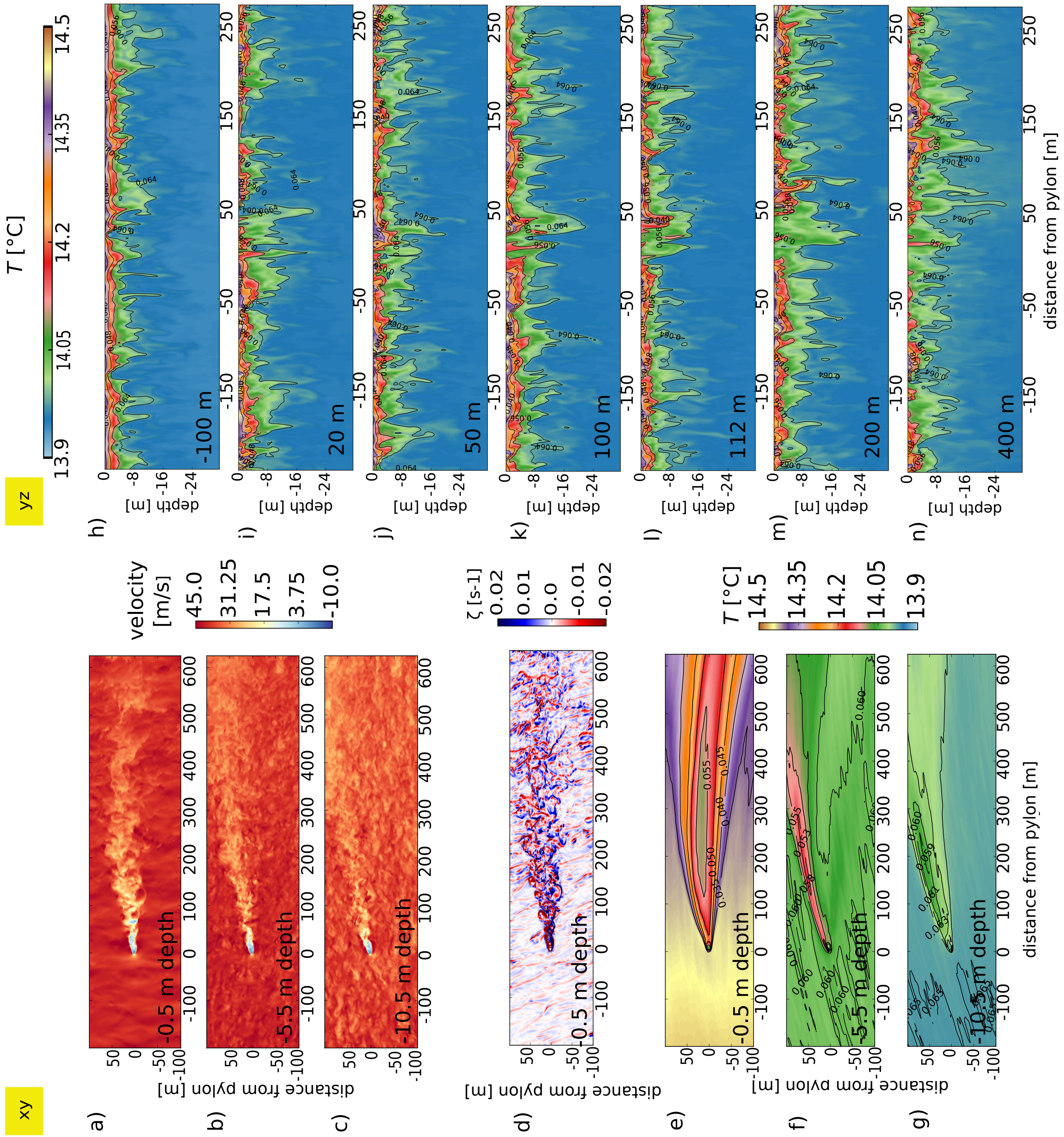

Figure 5.13: Extended summary of the simulation results for case (i) with $\Delta\ T \approx 0.5°C$. (a) – (c) Horizontal instantaneous cross-section of the velocity magnitude at -0.5 m, -10.5 m, and -15.5 m depth. (d) Relative vorticity ζ at -0.5 m depth. (e) – (g) Same as (a) – (c), but for temperature averaged over 5000 s. The black contours show the sediment concentrations in the wake of the monopile. (h) – (n) Vertical cross-sections of temperature perpendicular to initial flow direction. As in (e) – (g), the black contours illustrate the scalar concentration. The horizontal axis has been centered to the monopile location, with the flow going from (h) to (n). The different panels depict a cross-section situated at a given distance from the structure, which is specified in the bottom left corner of each panel. Negative cross-section positions stand for regions before the cylinder, positive positions for cross-sections after it.

Summary figures of the simulations with a stratified regime and a monopile : Case (ii)

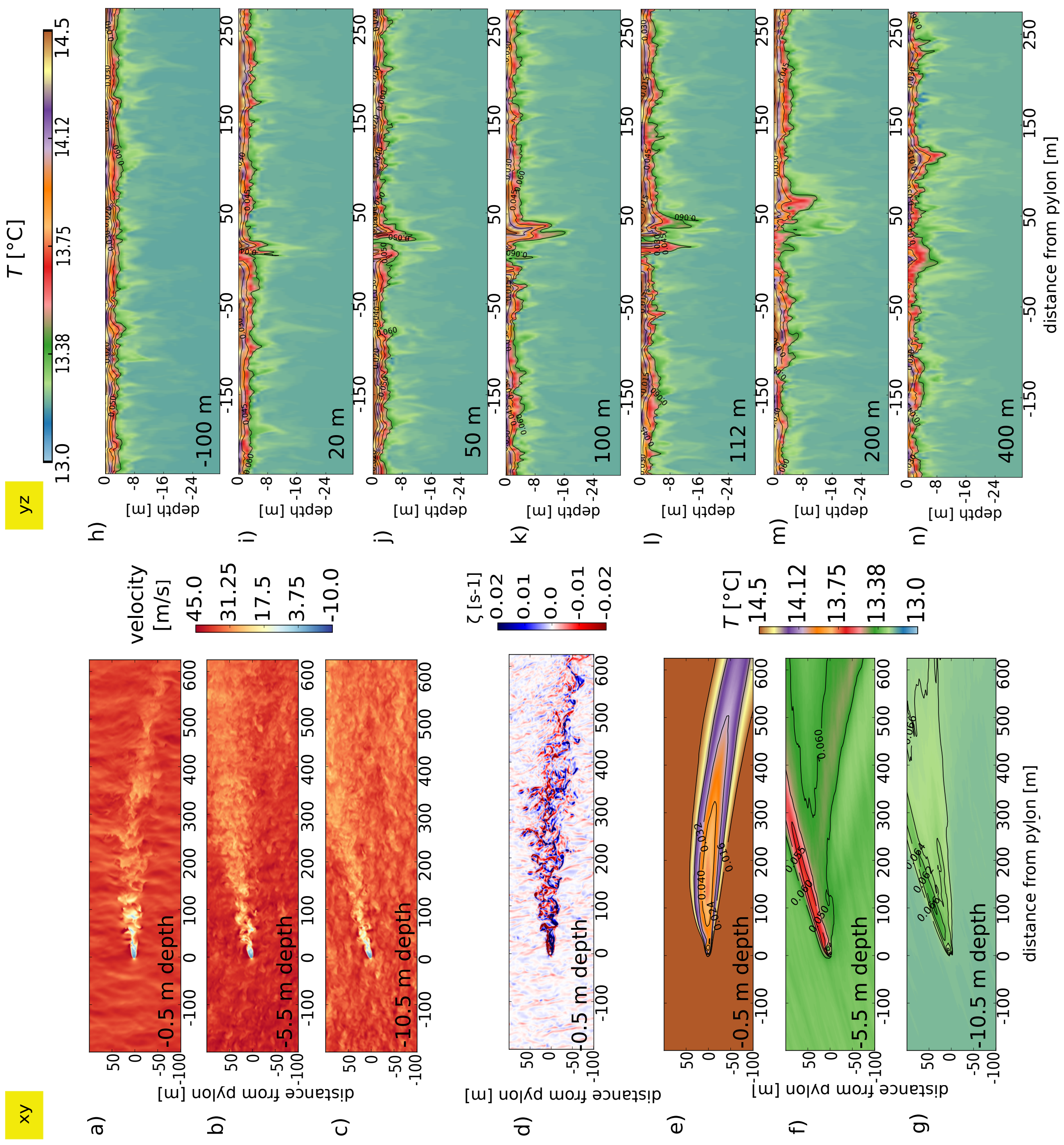

Summary figures of the simulations with a stratified regime and a monopile : Case (iii)

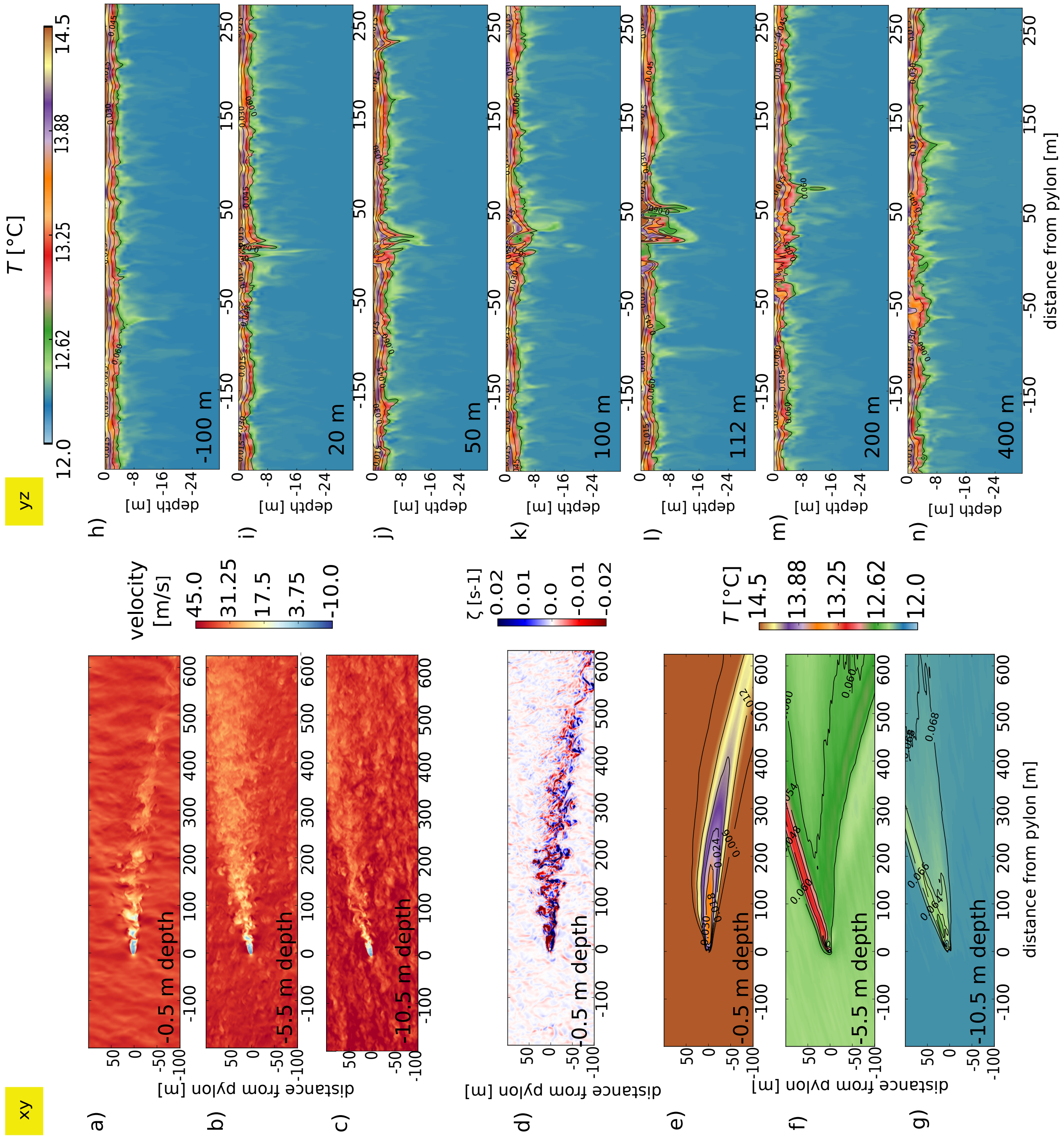

Summary figures of the simulations with a stratified regime and a monopile : Case (iv)

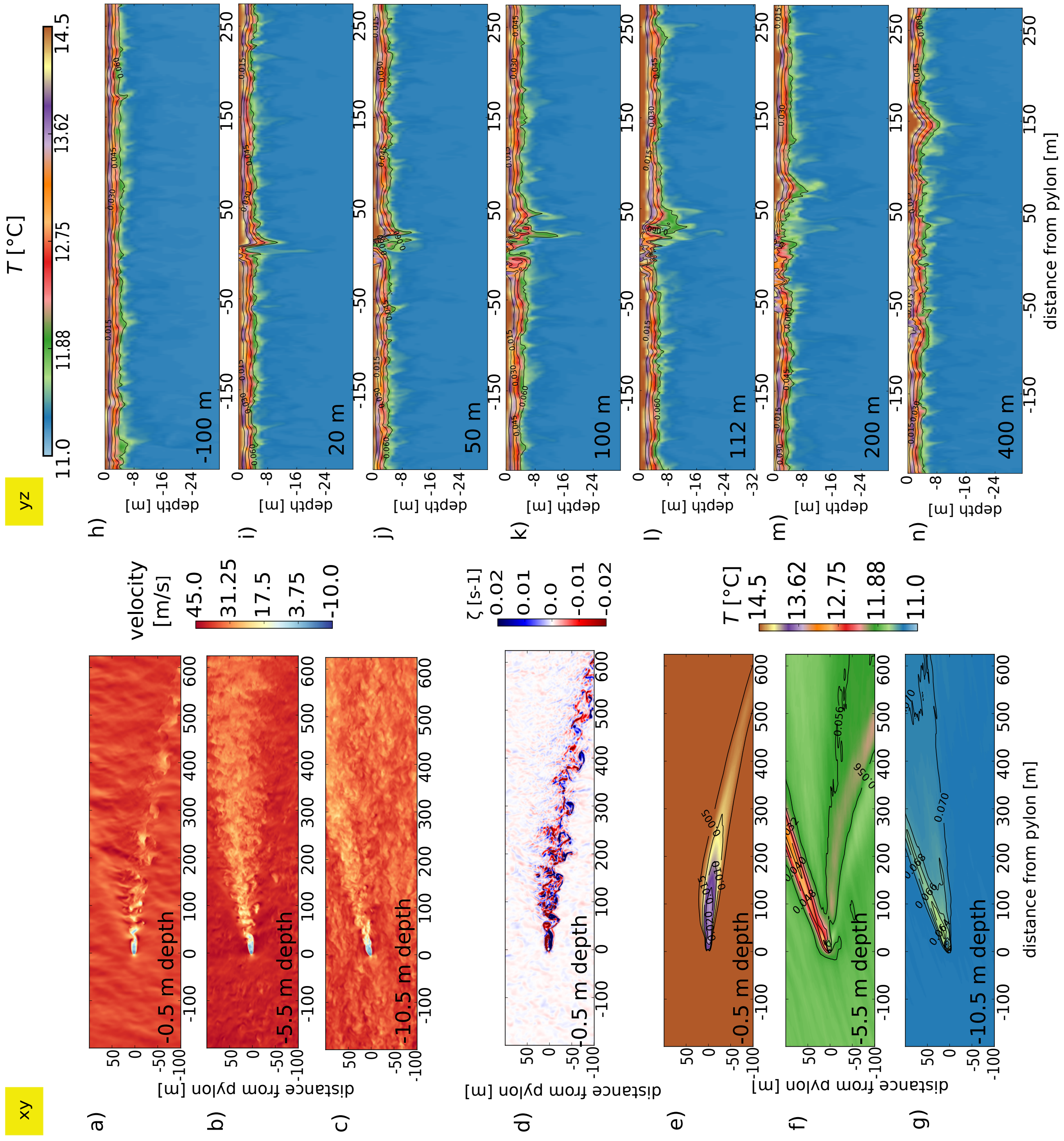

Comparison of ε and ϵ estimated for the same regions of cases (i) –(iv) for the simulations with and without the monopile

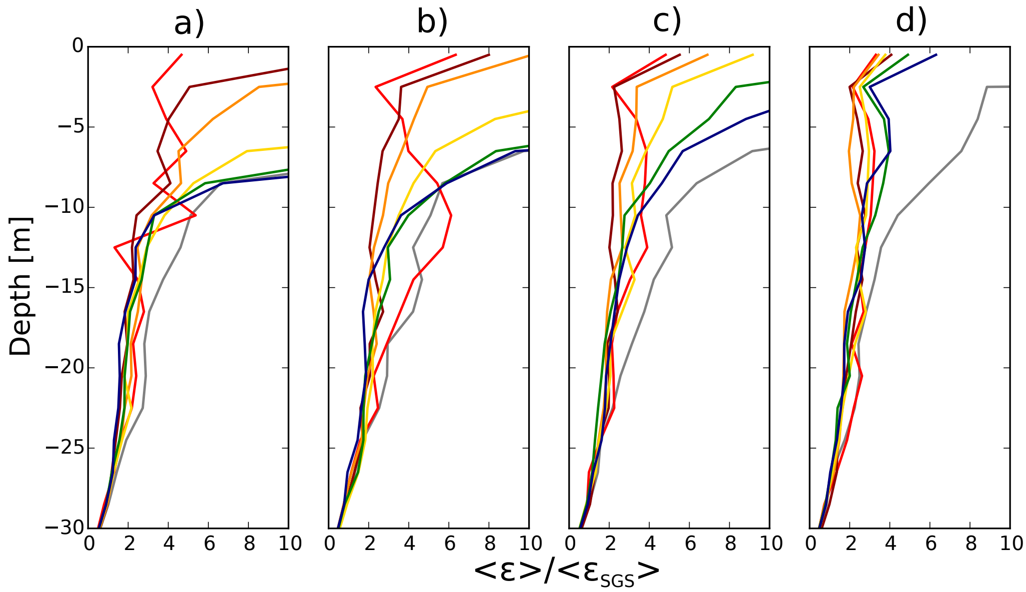

Figure 5.17: Ratio of the dissipation of turbulent kinetic energy calculated from power spectra, ε, to the subgrid-scale dissipation ϵ for cases (a) iv, (b) iii, (c) ii, and (d) i. Both estimates of dissipation compare well between 8 m and 30 m depth. The SGS model is known to underestimate dissipation due to numerical dissipation of the advection scheme, which partly explains the difference observed between the two methods below approximately 8 m depth. Close to the boundaries of the domain, the size of the eddies decreases and the performance of the subgrid-scale model drops.

6 Conclusions and Outlook

The present thesis assessed the natural variability of turbulence in a shallow shelf sea by means of two extensive datasets of shear microstructure measurements from gliders spanning over 30 days. The datasets have recorded shear microstructure measurements during weak to strongly stratified conditions and have captured the complete overturn of the strongly stratified thermocline during and after the passage of a storm. The measurements from these two campaigns provided valuable insights on the variability of the rate of dissipation of turbulent kinetic energy, turbulent diffusivity and intensity of turbulence within the water column.

It is seen that stratification in the study region during summer is highly variable. This is important because stratification controls the vertical fluxes in the water column, and therefore separates the turbulent surface and bottom mixed layers. Active, isotropic turbulence within stratification was identified but was shown to be intermittent. It does, however, play a major role in heat transfer between layers. This highlights the importance of collecting long-term measurements of small-scale turbulence, without which the adequate assessment of vertical transport could be biased. An attempt to identify possible shear instabilities across the thermocline through the bulk Richardson number (Ri_b) has shown instead a stable thermocline during approximately 96% of the measurement period. Short-lived small-scale shear instabilities that were not captured by our low frequency ADCP measurements, and therefore by Ri_b, could still be responsible for the intermittent pulses of elevated turbulence observed across the thermocline. However, the precise mechanism of this export is unknown.

On the other hand, high temporal variability of thermocline dissipation can also come from storm events, in which case the mechanism could be identified. During the storm, as a result of marginally stable conditions caused by elevated shear across stratification, turbulence levels in the thermocline were approximately one order of magnitude higher than during background stratified levels. Storms have been known to have a high contribution to biological productivity (*Dagg*, 1988; *Babin et al.*, 2004; *Walker et al.*, 2005; *Simpson and Sharples*, 2012; *Rumyantseva et al.*, 2015), however their importance on a seasonal basis is still uncertain (*Hanshaw et al.*, 2008; *Foltz et al.*, 2015). In this study, one storm event was estimated to account for 13% of the mean summer fluxes, and a rough extrapolation of this share to a mean number of storms during summer has indicated that they could be responsible for about 40% of the total seasonal fluxes. This suggests that storms add a significant portion of nutrient supply to the thermocline and surface mixed layer, which could indeed play a significant role for biological productivity during summer time.

Future work based on glider microstructure measurements could concentrate on reducing existing sources of error in the estimation of the dissipation of turbulent kinetic energy by refining the estimation of the glider flight and behavior. Small-scale shear below one meter resolution could be combined with the turbulence measurements to tackle the mechanism responsible for the short-lived turbulence bursts and therefore work towards an advancement of model parameterizations. Further turbulence datasets under stormy conditions are needed to understand the impact of summer storms on the seasonal budget. A holistic view of the system dynamics could be attained by combining turbulence measurements with large-scale observations of phytoplankton growth and nutrient availability. The impact of storms on the ecosystem could be also further investigated with high resolution large-eddy simulations, which could be compared to observations.

The last section of this PhD project was directed to the anthropogenic influence on shelf sea turbulence and mixing through the operation of offshore wind farms. Studies assessing the impact of the offshore wind farms on hydrodynamics are however scarce and this thesis provides a first small-scale study focused on turbulence and mixing at different levels of thermal stratification. Unique CTD observations of the vertical structure of the water column in- and outside the wake of wind farm foundations were combined with large-eddy simulations to provide a direct analysis of wake characteristics, and the extent of monopile generated mixing and vertical scalar transport. The wake of single offshore foundation structures is characterized by a narrow region past the monopile that continuously broadens with distance but at the same time also rapidly loses its strength.

The average impact of offshore wind farms on the dissipation of turbulent kinetic energy is expected to be comparable to thermocline levels under background conditions. Locally, within the first 100 m downstream the monopile, the vertical structure of the dissipation of turbulent kinetic energy was found to be approximately one order of magnitude higher than at background levels. The additional input of kinetic energy by the monopiles is dissipated rapidly downstream, which coincides with elevated levels of scalar transport and mixing on the wake. In the observed scenarios, a single foundation structure decreases stratification by 1 – 3% in 600 m distance, and the amount of turbulent kinetic energy that is used to mix the stratification lies between 8 – 14%. If non linear interactions among structures and other sources of mixing or heat input are neglected, weak stratification would be overturned in less than 10 days, which is in the same order of the advection time scale of the residence time of water within a farm (approximately 8 km) in the study region. If stronger stratification is present, an offshore wind farm in its current size is not expected to fully mix the water column. Overall, especially if compared to the natural variability of the area, the impact of a single structure on overall mixing and turbulence levels is low. Still, a monopile was estimated to increase the concentration of a passive scalar in the upper meters of the water column by 3 – 25%. Such additional pumping of tracer into the light surface layer, while at the same time maintaining temperature stratification, suggests that the sea surface would be locally enriched with valuable nutrients that support primary productivity. Moreover, the combined effect of multiple pylons over entire offshore wind farms could still locally alter the stability of the water column and alter the rates of primary production.

Future studies on offshore wind farm mixing could include additional sources of mixing (e.g. wave breaking, wind forcing) and stabilization such as solar heating, which have been neglected in this first analysis. The study of non-linear effects from the wakes of interacting structures could also be tackled to improve understanding of the impact of an entire farm on the local and regional stratification. These steps would enable the parameterization of the effect of offshore wind farms on regional models, enabling a broader understanding of their true impact.

In summary, considering the importance of shelf seas on the global rates of primary productivity, as well as their conspicuous role on a series of human activities, it is crucial to understand the governing mechanisms, natural or anthropogenic, underlying their variability. In the long term, understanding the natural state and variability of shelf seas, as well as their response to different events, will help us to predict mixing events and changes occurring in the dynamic coastal and shelf seas.

Acknowledgements

A couple of years ago, shortly before diving into this project, I would never have imagined how exciting and likewise challenging it would turn out to be. I would like to thank my supervisor Jeff Carpenter for all his support, encouragement and endless opportunities given. I would also like to express my sincere gratitude to the other members of my advisory panel throughout these past years, which was composed of Carsten Eden, Hans Burchard, Burkard Baschek and Peter Franks. It was a great honor for me to be able to receive their feedback, guidance and to participate in fruitful discussions with such a diverse panel with truly great scientists. In this context, special thanks go also to Jeff, Burkard and Peter, who have enabled and encouraged my stay at the Scripps Institution of Oceanography from the beginning. I am very grateful for this enriching opportunity.

Many thanks also go to Lucas Merckelbach, who has played a major role in my scientific and technical skill development in these past years, including glider maintenance and piloting, interesting discussions, and the introduction of Python and Linux into my world. Nowadays, I could barely imagine doing all the programming and data processing without these skills. Furthermore, I thank everyone else from KO (Division Operational Systems at HZG) for the friendly atmosphere, team work, lunches and coffee breaks, as well as the administrative department for their support. I gratefully acknowledge the financial support through the project PACES II (Polar Regions and Coasts in a Changing Earth System), funded by the Helmholtz Association.

I would also like to express my sincere gratitude to the PALM group for patiently answering my questions and their helpful suggestions related to LES. I thank Berit and Ingo from the School of Integrated Climate System Sciences (SICSS) for their help with administrative questions at the University, organization of retreats and events, and the team work during my two years in the team of doctoral representatives at SICSS. I will always be grateful for the guidance, continuous interest and support from Michael Melkonian and Björn Podola, who have introduced me to academia and have awaken my interest in the scientific topics that motivate me every single day.

All of this would have never been possible without the continuous trust, motivation and encouragement I have received from my family and friends. Thanks to Ingrid, Maria, Ryan, Jeff, Marc, Yoana, Ben and Julianna for our discussions, fellowship and countless rides together. In these years, I was also very lucky to get to know Elina, Jairo and Leo, with whom I shared many aspects of the PhD life and who have always been there for me - it feels like I owe you endless ice cream rounds. Hilke, many thanks for your enthusiasm, interest and the relaxing coffee breaks. Thorsten, Ingrid, Renan, Lau, Cici, Fe, Amina, Cau, Hartmut, Ruth and Izilda: thank you for being there for me throughout my life unconditionally. Niki, thank you for standing by me at all times and your endless endurance, which I truly admire. I feel incredibly lucky to have you all in my life.

Bibliography

Arakawa, A., and V. R. Lamb (1977), Computational design of the basic dynamical processes of the UCLA general circulation model, *Methods Comput. Phys.*, *17*, 173–265.

Babin, S. M., J. A. Carton, T. D. Dickey, and J. D. Wiggert (2004), Satellite evidence of hurricane-induced phytoplankton blooms in an oceanic desert, *J. Geophys. Res. Ocean.*, *109*(C3), doi:10.1029/2003JC001938.

Baeye, M., and M. Fettweis (2015), In situ observations of suspended particulate matter plumes at an offshore wind farm, southern North Sea, *Geo-Marine Lett.*, *35*, 247–255, doi:10.1007/s00367-015-0404-8 41.

Baker, M. A., and C. H. Gibson (1987), Samplig turbulence in the stratified ocean: statistical consequences of strong intermitency, *J. Phys. Oceanogr.*, *17*, 1817–1836, doi:https://doi.org/10.1175/1520-0485(1987)017<1817:STITSO>2.0.CO;2.

Bluteau, C. E., N. L. Jones, and G. N. Ivey (2016), Estimating Turbulent Dissipation from Microstructure Shear Measurements Using Maximum Likelihood Spectral Fitting over the Inertial and Viscous Subranges, *J. Atmos. Ocean. Technol.*, *33*(4), 713–722, doi:10.1175/JTECH-D-15-0218.1.

Bouffard, D., and L. Boegman (2013), A diapycnal diffusivity model for stratified environmental flows, *Dyn. Atmos. Ocean.*, *61-62*(June 2013), 14–34, doi: 10.1016/j.dynatmoce.2013.02.002.

Briscolini, M., and P. Santangelo (1989), Development of the mask method for incompressible unsteady flows, *J. Comput. Phys.*, *84*, 57–75.

Broström, G. (2008), On the influence of large wind farms on the upper ocean circulation, *J. Mar. Syst.*, *74*, 585–591, doi:10.1016/j.jmarsys.2008.05.001.

BSH (2016), North Sea: Existing and Perspective Uses and Nature Conservation, *Bundesamt für Schifffahrt und Hydropraphie*, p. 1.

Burchard, H., and K. Bolding (2002), GETM — a general estuarine transport model.

Burchard, H., and R. Hofmeister (2008), A dynamic equation for the potential energy anomaly for analysing mixing and stratification in estuaries and coastal seas, *Estuar. Coast. Shelf Sci.*, *77*(4), 679–687, doi:10.1016/j.ecss.2007.10.025.

Burchard, H., and T. P. Rippeth (2009), Generation of bulk shear spikes in shallow stratified tidal seas, *J. Phys. Oceanogr.*, *39*(4), 969–985, doi:10.1175/2008JPO4074.1.

Burchard, H., P. D. Craig, J. R. Gemmrich, H. van Haren, P. P. Mathieu, H. E. Meier, W. A. M. Smith, H. Prandke, T. P. Rippeth, E. D. Skyllingstad, W. D. Smyth, D. J. Welsh, and H. W. Wijesekera (2008), Observational and numerical modeling methods for quantifying coastal ocean turbulence and mixing, *Prog. Oceanogr.*, *76*(4), 399–442, doi:10.1016/j.pocean.2007.09.005.

Carpenter, J. R., L. Merckelbach, U. Callies, S. Clark, L. Gaslikova, and B. Baschek (2016), Potential impacts of offshore wind farms on North Sea stratification, *PLoS One*, *11*(8), doi:10.1371/journal.pone.0160830.

Caulfield, C. P., and W. R. Peltier (2000), The anatomy of the mixing transition in homogeneous and stratified free shear layers, *J. Fluid Mech*, *413*, 1–47, doi: 10.1017/S0022112000008284.

Cazenave, P. W., R. Torres, and J. I. Allen (2016), Unstructured grid modelling of offshore wind farm impacts on seasonally stratified shelf seas, *Prog. Oceanogr.*, *145*, 25–41, doi: 10.1016/j.pocean.2016.04.004.

Corbetta, G., I. Pineda, and J. Moccia (2014), The European offshore wind industry - key trends and statistics 2013, *Tech. rep.*, The European Wind Energy Association.

Corrsin, S. (1958), Local isotropy in turbulent shear flow, *N.A.C.A.*, *RM58B11*.

Cyr, F., D. Bourgault, and P. S. Galbraith (2015), Behavior and mixing of a cold intermediate layer near a sloping boundary, *Ocean Dyn.*, *65*(3), 357–374, doi:10.1007/s10236-014-0799-1.

Dagg, M. J. (1988), Physical and biological responses to the passage of a winter storm in the coastal and inner shelf waters of the northern Gulf of Mexico, *Cont. Shelf Res.*, *8*(2), 167–178.

Davis, R., C. Eriksen, and C. Jones (2002), Autonomous buoyancy-driven underwater gliders, in *Technol. Appl. Auton. Underw. Veh.*, edited by Taylor and Francis, p. 324, London, doi:doi:10.1201/9780203522301.ch3.

Deardorff, J. W. (1980), Stratocumulus-capped mixed layers derived from a three-dimensional model, *Boundary-Layer Meteorol.*, *18*(4), 495–527, doi: 10.1007/BF00119502.

Dewey, R. K., and W. R. Crawford (1988), Bottom stress estimates from vertical dissipation rate profiles on the continental shelf, doi:10.1175/1520-0485(1988)018<1167:BSEFVD>2.0.CO;2.

Eça, L., G. Vaz, G. Rosetti, and F. Pereira (2014), On the Numerical Prediction of the Flow Around Smooth Circular Cylinders, in *ASME 33rd Int. Conf. Ocean. Offshore Arct. Eng.*, pp. 1–11, San Francisco, California, doi:10.1115/OMAE2014-23230.

ESDU (1985), Circular Cylindrical Structures: Dynamic Re- sponse to Vortex Shedding, Part 1: Calculation Procedures and Derivation, *Tech. rep.*, Engineering Sciences Data Unit (ESDU), London.

European Parliament and the Council of the European Union (2009), Directive 2009/28/EC of the European Parliament and of the Council of 23 April 2009 on the promotion of the use of energy from renewable sources and amending and subsequently repealing Directives 2001/77/EC and 2003/30/EC, doi: 10.3000/17252555.L_2009.140.eng.

Falkowski, P., and D. A. Kiefer (1985), Chlorophyll a fluorescence in phytopankton: relationship to photosynthesis and biomass, *J. Plankt. Res.*, *7*(5), 715–731.

Fer, I., A. K. Peterson, and J. E. Ullgren (2014), Microstructure measurements from an underwater glider in the turbulent Faroe Bank Channel overflow, *J. Atmos. Ocean. Technol.*, *31*(5), 1128–1150, doi:10.1175/JTECH-D-13-00221.1.

Feser, F., M. Barcikowska, O. Krueger, F. Schenk, R. Weisse, and L. Xia (2015), Storminess over the North Atlantic and northwestern Europe-A review, *Q. J. R. Meteorol. Soc.*, *141*(687), 350–382, doi:10.1002/qj.2364.

Floeter, J., J. E. van Beusekom, D. Auch, U. Callies, J. Carpenter, T. Dudeck, S. Eberle, A. Eckhardt, D. Gloe, K. Hänselmann, M. Hufnagl, S. Janßen, H. Lenhart, K. O. Möller, R. P. North, T. Pohlmann, R. Riethmüller, S. Schulz, S. Spreizenbarth, A. Temming, B. Walter, O. Zielinski, and C. Möllmann (2017), Pelagic effects of offshore wind farm foundations in the stratified North Sea, *Prog. Oceanogr.*, *156*, 154–173, doi:10.1016/j.pocean.2017.07.003.

Foltz, G. R., K. Balaguru, and L. R. Leung (2015), A reassessment of the integrated impact of tropical cyclones on surface chlorophyll in the western subtropical North Atlantic, *Geophys. Res. Lett.*, *42*(4), 1158–1164, doi:10.1002/2015GL063222.

Franks, P. J. S. (2015), Has Sverdrup's critical depth hypothesis been tested? Mixed layers vs. turbulent layers, *ICES J. Mar. Sci.*, *72*(6), 1897–1907, doi:10.1093/icesjms/fsu175.

Froehlich, J. (2006), *Large Eddy Simulation turbulenter Strömungen*, 416 pp., Wiesbaden.

Garau, B., S. Ruiz, W. G. Zhang, A. Pascual, E. Heslop, J. Kerfoot, and J. Tintoré (2011), Thermal lag correction on slocum CTD glider data, *J. Atmos. Ocean. Technol.*, *28*(9), 1065–1071, doi:10.1175/JTECH-D-10-05030.1.

Gibbs, J. A., E. Fedorovich, B. Maronga, C. Wainwright, and M. Dröse (2016), Comparison of Direct and Spectral Methods for Evaluation of the Temperature Structure Parameter in Numerically Simulated Convective Boundary Layer Flows, *Mon. Weather Rev.*, *144*(6), 2205–2214, doi:10.1175/MWR-D-15-0390.1.

Glenn, S. M., T. N. Miles, G. N. Seroka, Y. Xu, R. K. Forney, F. Yu, H. Roarty, O. Schofield, and J. Kohut (2016), Stratified coastal ocean interactions with tropical cyclones, *Nat. Commun.*, *7*, 10,887, doi:10.1038/ncomms10887.

Goodman, L., E. R. Levine, and R. G. Lueck (2006), On measuring the terms of the turbulent kinetic energy budget from an AUV, *J. Atmos. Ocean. Technol.*, *23*(7), 977–990, doi:10.1175/JTECH1889.1.

Grashorn, S., and E. V. Stanev (2016), Kármán vortex and turbulent wake generation by wind park piles, *Ocean Dyn.*, *66*(12), 1543–1557, doi:10.1007/s10236-016-0995-2.

Gregg, M. C., M. H. Alford, H. Kontoyiannis, V. Zervakis, and D. Winkel (2012), Mixing over the steep side of the Cycladic Plateau in the Aegean Sea, *J. Mar. Syst.*, *89*(1), 30–47, doi:10.1016/j.jmarsys.2011.07.009.

Halpern, B. S., S. Walbridge, K. A. Selkoe, C. V. Kappel, F. Micheli, C. D'Agrosa, J. F. Bruno, K. S. Casey, C. Ebert, H. E. Fox, R. Fujita, D. Heinemann, H. S. Lenihan, E. M. P. Madin, M. T. Perry, E. R. Selig, M. Spalding, R. Steneck, and R. Watson

(2008), A global map of human impact on marine ecosystems, *Science*, *319*(5865), 948–952, doi:10.1126/science.1149345.

Hanshaw, M. N., M. S. Lozier, and J. B. Palter (2008), Integrated impact of tropical cyclones on sea surface chlorophyll in the North Atlantic, *Geophys. Res. Lett.*, *35*(1), doi:10.1029/2007GL031862.

Harlow, F. H., and J. E. Welch (1965), Numerical calculation of time- dependent viscous incompressible flow of fluid with free surface, *Phys. Fluids*, *8*, 2182–2189.

Hazel, P. (1972), Numerical studies of the stability of inviscid stratified shear flows, *J. Fluid Mech.*, *51*(1), 39–61.

Hebert, D. A., and S. M. de Bruyn Kops (2006), Predicting turbulence in flows with strong stable stratification, *Phys. Fluids*, *18*(6), 1–10, doi:10.1063/1.2204987.

Hellmann, G. (1919), *Über die Bewegung der Luft in den untersten Schichten der Atmosphäre*, Kgl. Akademie der Wissenschaften [G.] Reimer.

Ho, A., A. Mbistrova, and G. Corbetta (2016), The European Offshore Wind Industry: Key Trends and Statistics 2015, *Tech. rep.*, The European Wind Energy Association (EWEA).

Holligan, P., P. Williams, D. Purdie, and R. Harris (1984), Photosynthesis, respiration and nitrogen supply of plankton populations in stratified, frontal and tidally mixed shelf waters, *Mar. Ecol. Prog. Ser.*, *17*, 201–213, doi:10.3354/meps017201.

Howard, L. N. (1961), Note on a paper of John W. Miles, *J. Fluid Mech.*, *10*(4), 509–512, doi:https://doi.org/10.1017/S0022112061000317.

Huisman, J., J. Sharples, J. M. Stroom, P. M. Visser, W. E. A. Kardinaal, J. M. H. Verspagen, and B. Sommeijer (2004), Changes in turbulent mixing shift competition for light between phytoplankton species, *Ecology*, *85*(11), 2960–2970, doi:10.1890/03-0763.

Huthnance, J. (1991), Physical oceanography of the North Sea, *Ocean Shorel. Manag.*, *16*(3-4), 199–231, doi:10.1016/0951-8312(91)90005-M.

IOC, SCOR, and IAPSO (2010), *The international thermodynamic equation of seawater - 2010: Calculation and use of thermodynamic properties*, Intergovernmental Oceanographic Commission, Manuals and Guides No. 56, UNESCO.

Itsweire, E. C., K. N. Helland, and C. W. Van Atta (1986), The evolution of grid-generated turbulence in a stably stratified fluid, *J. Fluid Mech.*, *162*(1986), 299–338, doi:10.1017/S0022112086002069.

Ivey, G., K. Winters, and J. Koseff (2008), Density stratification, turbulence, but how much mixing?, *Annu. Rev. Fluid Mech.*, *40*(1), 169–184, doi:10.1146/annurev.fluid.39.050905.110314.

Jackett, D. R., T. J. McDougall, R. Feistel, D. G. Wright, and S. M. Griffies (2006), Algorithms for density, potential temperature, conservative temperature, and the freezing temperature of seawater, *J. Atmos. Ocean. Technol.*, *23*(12), 1709–1728, doi:10.1175/JTECH1946.1.

Kataoka, H., and M. Mizuno (2002), Numerical flow computation around aeroelastic 3d square cylinder using inflow turbulence, *Wind Struct.*, *5*, 379–392, doi: 10.12989/was.2002.5.2_3_4.379.

Kiefer, D. A. (1973), Chlorophyll a fluorescence in marine diatoms: Response of chloroplasts to light and nutrient stress, *Mar. Biol.*, *23*, 39–46.

Kolmogorov, A. N. (1941), Dissipation of energy in the locally isotropic turbulence, *Dokl. Akad. Nauk. SSSR*, *32*, 16–18.

Lauria, M. L., D. A. Purdie, and J. Sharples (1999), Contrasting phytoplankton distributions controlled by tidal turbulence in an estuary, *J. Mar. Syst.*, *21*(1-4), 189–197, doi:10.1016/S0924-7963(99)00013-5.

Lawrence, G., R. Pieters, L. Zaremba, T. Tedford, L. Gu, S. Greco, and P. Hamblin (2004), Summer exchange between Hamilton Harbour and Lake Ontario, *Deep. Res. Part II Top. Stud. Oceanogr.*, *51*(4-5), 475–487, doi:10.1016/j.dsr2.2003.09.002.

Ledwell, J. R., T. F. Duda, M. A. Sundermeyer, and H. E. Seim (2004), Mixing in a coastal environment: 1. A view from dye dispersion, *J. Geophys. Res. C Ocean.*, *109*(10), 1–20, doi:10.1029/2003JC002194.

Ludewig, E. (2015), *On the Effect of Offshore Wind Farms on the Atmosphere and Ocean Dynamics*, 1–162 pp., Springer International Publishing, Ludewig2015, doi: http://dx.doi.org/10.1007/978-3- 319-08641-5.

Lueck, R. (2013), RSI Technical Note 028: Calculating the rate of dissipation of turbulent kinetic energy, *Tech. rep.*, Rockland Scientific, Victoria.

Lueck, R. G., and J. J. Picklo (1990), Thermal Inertia of Conductivity Cells: Observations with a Sea-Bird Cell, doi:10.1175/1520-0426(1990)007<0756:TIOCCO>2.0.CO;2.

Lueck, R. G., F. Wolk, and H. Yamazaki (2002), Oceanic velocity microstucture measurements in the 20th century, *J. Oceanogr.*, *58*, 153–174.

Lund, T. S., X. Wu, and K. D. Squires (1998), Generation of turbulent in- flow data for spatially-developing boundary layer simulations, *J. Comput. Phys.*, *140*, 233–258.

MacKinnon, J. A., and M. C. Gregg (2003), Mixing on the Late-Summer New England Shelf - Solibores, Shear, and Stratification, *J. Phys. Oceanogr.*, *33*(7), 1476–1492, doi: 10.1175/1520-0485(2003)033<1476:MOTLNE>2.0.CO;2.

Maronga, B., A. F. Moene, D. van Dinther, S. Raasch, F. C. Bosveld, and B. Gioli (2013), Derivation of Structure Parameters of Temperature and Humidity in the Convective Boundary Layer from Large-Eddy Simulations and Implications for the Interpretation of Scintillometer Observations, *Boundary-Layer Meteorol.*, *148*(1), 1–30, doi:10.1007/s10546-013-9801-6.

Maronga, B., M. Gryschka, R. Heinze, F. Hoffmann, F. Kanani-Sühring, M. Keck, K. Ketelsen, M. O. Letzel, M. Sühring, and S. Raasch (2015), The Parallelized Large-Eddy Simulation Model (PALM) version 4.0 for atmospheric and oceanic flows: Model formulation, recent developments, and future perspectives, *Geosci. Model Dev.*, *8*(8), 2515–2551, doi:10.5194/gmd-8-2515-2015.

Merckelbach, L., D. Smeed, and G. Griffiths (2010), Vertical water velocities from underwater gliders, *J. Atmos. Ocean. Technol.*, *27*(3), 547–563, doi:10.1175/2009JTECHO710.1.

Miles, J. W. (1961), On the stability of heterogeneous shear flows, *J. Fluid Mech.*, *10*(4), 496–508.

Miles, J. W., and L. N. Howard (1964), Note on a heterogeneous shear flow, *J. Fluid Mech.*, *20*(2), 331–336, doi:https://doi.org/10.1017/S0022112064001252.

Moeng, C.-H., and J. C. Wyngaard (1988), Spectral Analysis of Large-Eddy Simulations of the Convective Boundary Layer, *J. Atmos. Sci.*, *45*(23), 3573–3587, doi:10.1175/1520-0469(1988)045<3573:SAOLES>2.0.CO;2.

Morison, J., R. Andersen, N. Larson, E. D'Asaro, and T. Boyd (1994), The Correction for Thermal-Lag Effects in Sea-Bird CTD Data, doi:10.1175/1520-0426(1994)011<1151:TCFTLE>2.0.CO;2.

Moum, J. N., M. C. Gregg, R. C. Lien, and M. E. Carr (1995), Comparison of turbulence kinetic energy dissipation rate estimates from two ocean microstructure profilers, *J. Atmos. Ocean. Technol.*, *12*(2), 346–366, doi:10.1175/1520-0426(1995)012<0346:COTKED>2.0.CO;2.

Muller-Karger, F. E., R. Varela, R. Thunell, R. Luerssen, C. Hu, and J. J. Walsh (2005), The importance of continental margins in the global carbon cycle, *Geophys. Res. Lett.*, *32*(1), 1–4, doi:10.1029/2004GL021346.

Nasmyth, P. W. (1970), Ocean Turbulence, Ph.D. thesis, University of British Columbia.

Osborn, T. R. (1980), Estimates of the Local Rate of Vertical Diffusion from Dissipation Measurements, doi:10.1175/1520-0485(1980)010<0083:EOTLRO>2.0.CO;2.

Palmer, M. R., T. P. Rippeth, and J. H. Simpson (2008), An investigation of internal mixing in a seasonally stratified shelf sea, *J. Geophys. Res. Ocean.*, *113*(12), doi:10.1029/2007JC004531.

Palmer, M. R., G. R. Stephenson, M. E. Inall, C. Balfour, a. Düsterhus, and J. a. M. Green (2015), Turbulence and mixing by internal waves in the Celtic Sea determined from ocean glider microstructure measurements, *J. Mar. Syst.*, *144*, 57–69, doi:10.1016/j.jmarsys.2014.11.005.

Paskyabi, M. B., and I. Fer (2012), Upper ocean response to large wind farm effect in the presence of surface gravity waves, *Energy Procedia*, *24*, 245–254, doi:10.1016/j.egypro.2012.06.106.

Petersen, J. K., and T. Malm (2006), Offshore Windmill Farms: Threats to or Possibilities for the Marine Environment, *Ambio*, *35*(2), 75–80, doi:10.1579/0044-7447(2006)35.

Peterson, A. K., and I. Fer (2014), Dissipation measurements using temperature microstructure from an underwater glider, *Methods Oceanogr.*, *10*, 44–69, doi:10.1016/j.mio.2014.05.002.

Piacsek, S. A., and G. P. Williams (1970), Conservation properties of convection difference schemes, *J. Comput. Phys.*, pp. 580–616.

Pingree, R. D., and D. K. Griffiths (1978), Tidal fronts on the shelf seas around the British Isles, *J. Geophys. Res.*, *83*(C9), 4615, doi:10.1029/JC083iC09p04615.

Pope, S. B. (2000), *Turbulent Flows*, 771 pp., Cambridge University Press, doi: 10.1088/0957-0233/12/11/705.

Raasch, S., and D. Etling (1991), Numerical simulation of rotating turbulent thermal convection, *Contrib. to Atmos. Phys.*, *64*(3), 185–199.

Raasch, S., and D. Etling (1998), Modeling Deep Ocean Convection: Large Eddy Simulation in Comparison with Laboratory Experiments, *J. Phys. Oceanogr.*, *28*, 1786–1802, doi:10.1175/1520-0485(1998)028<1786:MDOCLE>2.0.CO;2.

Raasch, S., and M. Schröter (2001), PALM - A large-eddy simulation model performing on massively parallel computers, *Meteorol. Zeitschrift*, *10*(5), 363–372, doi:10.1127/0941-2948/2001/0010-0363.

Rennau, H., S. Schimmels, and H. Burchard (2012), On the effect of structure-induced resistance and mixing on inflows into the Baltic Sea: A numerical model study, *Coast. Eng.*, *60*(1), 53–68, doi:10.1016/j.coastaleng.2011.08.002.

Reynolds, O. (1895), On the dynamical theory of incompressible viscous fluids and the determination of the criterion, *Philos. Trans. R. Soc. London. A*, *186*, 123–164.

Richardson, K., and F. B. Pedersen (1998), Estimation of new production in the North Sea: consequences for temporal and spatial variability of phytoplankton, *ICES J. Mar. Sci.*, *55*(4), 574–580.

Richardson, K., T. Nielsen, F. Pedersen, J. Heilman, B. Løkkegaard, and K. H (1998), Spatial heterogeneity in the structure of the planktonic food web in the North Sea, *Mar. Ecol. Prog. Ser.*, *168*, 197–211, doi:10.3354/meps168197.

Richardson, L. F. (1920), The Supply of Energy from and to Atmospheric Eddies, *Proc. R. Soc. A Math. Phys. Eng. Sci.*, *97*(686), 354–373, doi:10.1098/rspa.1920.0039.

Rippeth, T. P. (2005), Mixing in seasonally stratified shelf seas: a shifting paradigm., *Philos. Trans. A. Math. Phys. Eng. Sci.*, *363*(1837), 2837–2854, doi: 10.1098/rsta.2005.1662.

Rippeth, T. P., M. R. Palmer, J. H. Simpson, N. R. Fisher, and J. Sharples (2005), Thermocline mixing in summer stratified continental shelf seas, *Geophys. Res. Lett.*, *32*(5), 1–4, doi:10.1029/2004GL022104.

Rosetti, G. F., G. Vaz, and A. L. C. Fujarra (2012), Urans calculations for smooth circular cylinder flow in a wide range of reynolds numbers: solution verification and validation, in *ASME 2012 31st Int. Conf. Ocean. Offshore Arct. Eng.*, pp. 1–23, Rio de Janeiro, doi:doi:10.1115/OMAE2012-83155.

Ross, O. N., and J. Sharples (2007), Phytoplankton motility and the competition for nutrients in the thermocline, *Mar. Ecol. Prog. Ser.*, *347*, 21–38, doi:10.3354/meps06999.

Roulund, A., B. Sumer, J. Fredsøe, and J. Michelsen (2005), Numerical and experimental investigation of flow and scour around a circular pile, *J. Fluid Mech.*, *534*, 351–401.

Rovelli, L., M. Dengler, M. Schmidt, S. Sommer, P. Linke, and D. F. McGinnis (2016), Thermocline mixing and vertical oxygen fluxes in the stratified central North Sea, *Biogeosciences*, *13*(5), 1609–1620, doi:10.5194/bg-13-1609-2016.

Rudnick, D. L. (2016), Ocean research enabled by underwater gliders, *Ann. Rev. Mar. Sci.*, *8*(1), 519–541, doi:10.1146/annurev-marine-122414-033913.

Rumyantseva, A., N. Lucas, T. Rippeth, A. Martin, S. C. Painter, T. J. Boyd, and S. Henson (2015), Ocean nutrient pathways associated with the passage of a storm, *Global Biogeochem. Cycles*, *29*, 1179–1189, doi:10.1002/2015GB005097.Received.

Saiki, E. M., C.-h. Moeng, and P. P. Sullivan (2000), Large-eddy simulation of the stably stratified planetary boundary layer, *Boundary-Layer Meteorol.*, *95*, 1–30.

Schlichting, H., and K. Gersten (2000), *Boundary Layer Theory*, 8th editio ed., Springer Verlag, Berlin.

Schultze, L. K. P., L. M. Merckelbach, and J. R. Carpenter (2017), Turbulence and mixing in a shallow shelf sea from underwater gliders, *J. Geophys. Res. Ocean.*, *122*, doi:10.1002/2017JC012872.

Schumann, U. (1973), Ein Verfahren zur direkten numerischen Simulation turbulenter Strömungen in Platten- und Ringspaltkanälen und über seine Anwendung zur Untersuchung von Turbulenz-modellen, Phd thesis, Universität Karlsruhe.

Sharples, J., C. M. Moore, T. P. Rippeth, P. M. Holligan, D. J. Hydes, N. R. Fisher, and J. H. Simpson (2001), Phytoplankton distribution and survival in the thermocline, *Limnol. Ocean.*, *46*(3), 486–496, doi:10.4319/lo.2001.46.3.0486.

Shih, L. H., J. R. Koseff, G. N. Ivey, and J. H. Ferziger (2005), Parameterization of turbulent fluxes and scales using homogeneous sheared stably stratified turbulence simulations, *J. Fluid Mech.*, *525*(August 2004), 193–214, doi:10.1017/S0022112004002587.

Simpson, J. H., and J. Sharples (2012), *Introduction to the physical and biological oceanography of shelf seas*, 424 pp., Cambridge University Press.

Simpson, J. H., J. Brown, J. Matthews, and G. Allen (1990), Tidal Straining, Density Currents, and Stirring in the Control of Estuarine Stratification, *Estuaries*, *13*(2), 125–132, doi:10.2307/1351581.

Simpson, J. H., W. R. Crawford, T. P. Rippeth, A. R. Campbell, and J. V. S. Cheok (1996), The Vertical Structure of Turbulent Dissipation in Shelf Seas, *J. Phys. Oceanogr.*, *26*(8), 1579–1590, doi:10.1175/1520-0485(1996)026<1579:TVSOTD>2.0.CO;2.

Smagorinsky, J. (1963), General Circulation Experiments With the Primitive Equations, *Mon. Weather Rev.*, *91*(3), 99–164, doi:10.1175/1520-0493(1963)091<0099:GCEWTP>2.3.CO;2.

Smyth, W. D., and J. N. Moum (2000), Anisotropy of turbulence in stably stratified mixing layers, *Phys. Fluids*, *12*(6), 1327, doi:10.1063/1.870385.

Smyth, W. D., and J. N. Moum (2013), Marginal instability and deep cycle turbulence in the eastern equatorial Pacific Ocean, *Geophys. Res. Lett.*, *40*(23), 6181–6185, doi: 10.1002/2013GL058403.

Smyth, W. D., J. N. Moum, and D. R. Caldwell (2001), The Efficiency of Mixing in Turbulent Patches: Inferences from Direct Simulations and Microstructure Observations, *J. Phys. Oceanogr.*, *31*(8), 1969–1992, doi:10.1175/1520-0485(2001)031<1969:TEOMIT>2.0.CO;2.

Smyth, W. D., J. R. Carpenter, and G. A. Lawrence (2007), Mixing in symmetric holmboe waves, *J. Phys. Oceanogr.*, *37*(6), 1566, doi:10.1175/JPO3037.1.

Spera, D. A., and T. R. Richards (1979), Modified power law equations for vertical wind profiles, in *Wind Energy Charact. Wind Energy Siting*, Portland.

Stillinger, D. C., K. N. Helland, and C. W. Van Atta (1983), Experiments on the transition of homogeneous turbulence to internal waves in a stratified fluid, *J. Fluid Mech.*, *131*, 91–122, doi:10.1017/S0022112083001251.

Tennekes, H., and J. L. Lumley (1973), *A first course in turbulence*, The MIT Press, Cambridge.

Thomas, H., Y. Bozec, K. Elkalay, and H. J. W. de Baar (2004), Enhanced open ocean storage of CO2 from shelf sea pumping, *Science (80-.).*, *304*(5673), 1005–1008, doi: 10.1126/science.1095491.

Thorpe, S. (2007), *An Introduction to Ocean Turbulence*, 264 pp., doi: 10.1029/2008EO520011.

Thorpe, S. A. (1971), Experiments on the instability of stratified shear flows: miscible fluids, *J. Fluid Mech.*, *46*(2), 299–319, doi:https://doi.org/10.1017/S0022112071000557.

Thorpe, S. A., and Z. Liu (2009), Marginal Instability?, *J. Phys. Oceanogr.*, *39*(9), 2373–2381, doi:10.1175/2009JPO4153.1.

Umlauf, L., and H. Burchard (2005), Second-order turbulence closure models for geophysical boundary layers. A review of recent work., *Cont. Shelf Res.*, *25*(7-8), 795–827.

van Beusekom, J. E., and S. Diel-Christiansen (2009), Global change and the biogeochemistry of the North Sea: the possible role of phytoplankton and phytoplankton grazing, *Int. J. Earth Sci.*, *98*(2), 269–280, doi:10.1007/s00531-007-0233-8.

van der Lee, E. M., and L. Umlauf (2011), Internal wave mixing in the Baltic Sea: Near-inertial waves in the absence of tides, *J. Geophys. Res. Ocean.*, *116*(10), 1–16, doi:10.1029/2011JC007072.

van Haren, H., L. R. M. Maas, J. T. F. Zimmerman, H. Ridderinkhof, and H. Malschaert (1999), Strong inertial currents and marginal internal wave stability in the central North Sea, *Geophys. Res. Lett.*, *26*(19), 2993–2996.

van Leeuwen, S., P. Tett, D. Mills, and J. van Der Molen (2015), Stratified and nonstratified areas in the North Sea: Long-term variability and biological and policy implications, *J. Geophys. Res. Ocean.*, *120*, 4670–4686, doi:doi:10.1002/2014JC010485.

Voynova, Y. G., H. Brix, W. Petersen, S. Weigelt-Krenz, and M. Scharfe (2017), Extreme flood impact on estuarine and coastal biogeochemistry: The 2013 Elbe flood, *Biogeosciences*, *14*(3), 541–557, doi:10.5194/bg-14-541-2017.

Walker, N. D., R. R. Leben, and S. Balasubramanian (2005), Hurricane-forced upwelling and chlorophyll a enhancement within cold-core cyclones in the Gulf of Mexico, *Geophys. Res. Lett.*, *32*(18), doi:10.1029/2005GL023716.

Walter, R. K., M. E. Squibb, C. B. Woodson, J. R. Koseff, and S. G. Monismith (2014), Stratified turbulence in the nearshore coastal ocean: Dynamics and evolution in the presence of internal bores, *J. Geophys. Res. Ocean.*, *119*, 8709–8730, doi:10.1002/2014JC010396.Received.

Wicker, L. J., and W. C. Skamarock (2002), Time-Splitting Methods for Elastic Models Using Forward Time Schemes, *Mon. Weather Rev.*, *130*(8), 2088–2097, doi:10.1175/1520-0493(2002)130<2088:TSMFEM>2.0.CO;2.

Wilkes, J., J. Moccia, A. Arapogianni, M. Dragan, N. Plytas, and A.-B. Genachte (2012), The European offshore wind industry key 2011 - trends and statistics, *Tech. Rep. January*, doi:10.1109/CCA.1997.627749.

Wind Europe, B. I., T. Remy, and A. Mbistrova (2018), The European offshore wind industry - key trends and statistics 2017, *Tech. rep.*, Wind Europe, Brussels, Belgium.

Winters, K. B., P. N. Lombard, J. J. Riley, and E. A. D'Asaro (1995), Available potential energy and mixing in density stratified fluids, *J. Fluid Mech.*, *289*, 115–128, doi:10.1146/annurev-fluid-011212-140620.

Wolk, F., and R. G. Lueck (2009), Turbulence Measurements from a Glider, in *13th Work. Phys. Process. Nat. Waters*, pp. 1–11.

Wolk, F., H. Yamazaki, L. Seuront, and R. G. Lueck (2002), A new free-fall profiler for measuring biophysical microstructure, *J. Atmos. Ocean. Technol.*, *19*(5), 780–793, doi:10.1175/1520-0426(2002)019<0780:ANFFPF>2.0.CO;2.